Fractal Grid-Turbulence and its Effects on a Performance of a Model of a Hydrokinetic Turbine

by

Altayeb Mahfouth

B.Sc., University of Zawia, Libya, 2008

A Thesis Submitted in Partial Fulfillment of the Requirements for the Degree of

Master of Applied Science

in the Department of Mechanical Engineering

University of Victoria

Supervisory Committee

Fractal grid turbulence and its effects on a performance of a model of a hydrokinetic turbine

by

Altayeb Juma Mahfouth

B.Sc., University of Zawia, Libya, 2008

Supervisory Committee

Dr. Curran Crawford, (Department of Mechanical Engineering)

Supervisor

Dr. Brad Buckham, (Department of Mechanical Engineering)

Departmental Member

Abstract

Supervisory Committee

Dr. Curran Crawford, (Department of Mechanical Engineering)

Supervisor

Dr. Brad Buckham, (Department of Mechanical Engineering)

Departmental Member

This thesis focuses on generating real world turbulence levels in a water tunnel rotor test using fractal grids and characterizing the effect of the fractal grid generated-turbulence on the performance of hydrokinetic turbines. The research of this thesis is divided into three studies: one field study and two laboratory studies. The field study was conducted at the Canadian Hydro Kinetic Turbine Test Centre (CHTTC) on the Winnipeg River. An Acoustic Doppler Velocimeter (ADV) was used in the field study to collect flow measurements in the river. The laboratory studies were conducted at the University of Victoria (UVic) fluids research lab and the Sustainable Systems Design Lab (SSDL). In addition, the Particle Image Velocimetry (PIV) technique was used in the experiential studies to obtain quantitative information about the vector flow field along the test section, both upstream and downstream of the rotor's plane.

The first study is a field study aiming to provide real flow characteristics and turbulence properties at different depths from the free-surface to boundary layer region of a fast river current by conducting a field study in the Winnipeg River using ADV. A novel technique to deploy and control an ADV from free-surface to boundary layer in a fast-current channel is introduced in this work. Flow characteristics in the river, including mean flow velocities and turbulence intensity profiles are analyzed. The obtained results indicate that the maximum mean velocity occurs below the free-surface, suggesting that the mean velocity is independent of the channel depth. From the free-surface to half depth, it was found that changes in both the mean velocity and turbulence intensity are gradual. From mid-depth to the river bed, the mean velocity drops rapidly while the

turbulence intensity increases at a fast rate. The turbulent intensity varied from 9% at the free-surface to around 17.5% near the river bed. The results of this study were used in the second lab study to help designing a fractal grid for a recirculating water flume tank. The goal was to modify the turbulence intensity in the water tunnel such that the generated turbulence was similar to that in the river at a location typical of a hydrokinetic device. The properties of fractal-generated turbulence were experimentally investigated by means of 2D Particle Image Velocimetry (PIV). The streamwise turbulent intensity profiles for different grids along the channel are presented. Additionally, visualization of the average and fluctuating flow fields are also presented. The results are in good agreement with results in literature. The third and final study investigated the power coefficient of a scale hydrokinetic turbine rotor in controlled turbulent flow (7.4 % TI), as well as in the low-turbulence smooth flow (0.5% TI) typical of lab scale testing. PIV was employed for capturing the velocity field. The results show that using realistic TI levels in the water tunnel significantly decrease the turbine's power coefficient compared to smooth flow, highlighting the importance of considering this effect in future experimental campaigns.

Contents

List of Tables

List of Figures

Nomenclature

Acronyms

ADCP	Acoustic Doppler Current Profiler
ADV	Acoustic Doppler Velocimeter
CHTTC	Canadian Hydro Kinetic Turbine Test Centre
CFD	Computational Fluid Dynamics
FDM	Fused Deposition Modeling
HAHT	Horizontal axis hydrokinetic turbine
HTs	Hydrokinetic turbines
IMU	Inertial Measurement Unit
PIV	Particle Image Velocimetry
SSDL	Sustainable Systems Design Lab
SYS_x	Systematic uncertainty
TI	Turbulence intensity
TSR	Tip Speed Ratio
RAN_x	Random uncertainty
UNC_x	Total uncertainty
UVic	University of Victoria
VAHT	Vertical axis hydrokinetic turbine

Symbols

A_{cc}	Vertical component of the acceleration
B^j	Number of patterns at each scale-iteration
B	Blade pitch angle
C_p	Power coefficient
C_T	Thrust coefficient
D_f	Fractal dimension
δV	A lump of fluid of volume
F	Flatness

g	Gravity
γ	Rotor yaw angle
λ	Taylor microscale
L_0, L_{max}	Length largest bar in the grid
M	Number of samples
μ	Dynamic viscosity
M_{eff}	Effective mesh size
N	Fractal iteration
v	Kinematic viscosity
υ	Confidence level
p	Pressure
P_{out}	Power output
$\emptyset$	pitch angle
ρ	Flow density
σ	Blockage ration
R	Blade tip radius
R_{ij}	Reynolds stresses
R_e	Reynolds number
R_L	Ratio of the bars' length between each iteration in the grid
R_t	Ratios of the bars' thickness between each iteration in the grid
ρ_{uu}	Autocorrelation coefficient
S	Number of rectangular bars
S_T	Standard deviation
θ	Yaw angle
T	Water tunnel
T_{rotor}	Torque
TI	Turbulence intensity
TKE	Turbulent kinetic energy
t_r	Thickness ratio
t_{min}	Thickness of smallest element in the grid

t_0, t_{max}	Thickness of largest element in the grid
$\vec{u}$	Flow speed
ū	Averaged speed
u'	Fluctuation velocity
U∞	Inlet speed
ω	rotational speed
x_{peak}	TI peak location
x_*	Wake-interaction length scale
σ_u	Standard deviation

Acknowledgements

I would like to express my sincere gratitude to my supervisor *Dr. Curran Crawford*, for his encouragement, support and guidance during my study and research from the initial to the final step.

I would like to extend my thanks to *Amir Birjandi*, *Mostafa Rahimpou*r, and *Italo Franchini* who were directly involved in the completion of this research.

Finally, I owe my deepest gratitude and loving thanks to *my parents* and *my wife*, and *my brothers and sisters*, and *friends*, for their encouragement, and moral support over all these years.

Chapter 1

1 Introduction

1.1 World energy consumption

There is a relationship between energy demand and population, where, increasing population means more industrial activity and technological change, in turn leading more energy demand and increasing energy costs. According to the United Nations Secretariat, the world population in mid-2015 reached 7.35 billion and is expected to be around 8.5 billion in 2030[1]. This increasing population will lead to increases in the world's energy demand. Based on the International Energy Agency (IEA) report, increases in the world population will contribute to world energy consumption growth of 48% between 2012 and 2040[2]. Energy consumption is the largest source of the environmental pollution emissions, coming primarily from the combustion of fossil fuels and bioenergy[2]. Rising energy demand (or population) results in impacts on human health and the worsening environment as economies develop[3] [Kaya Yoichi & Yokobori Keiichi (1997)]. These factors are the prime motivation for development of renewable energy technologies and thereby drive toward sourcing a higher percentage of our primary energy from renewables. The current concern of the world is to manage and reduce pollution by depending more on renewable energy. The IEA reported that renewables are the world's fastest-growing energy source over the projection period, increasing about 2.6 %/year between 2012 and 2040[2].

One of the renewable energy sources is hydrokinetic energy (encompassing both river, tidal and ocean current devices), which has a relatively high energy density, is a predictable resource (depending the specific hydrokinetic type), and can serve variously as baseload or dispatchable generation. Most experimental studies of hydrokinetic turbines have been conducted in low turbulence intensity water channels [Bahaj et, al., (2007), Harrison et, al., (2009), Whelan et, al.,

---

[1] "The United Nations Secretariat" [Online]. Available: https://esa.un.org/unpd/wpp/publications/files/key_findings_wpp_2015.pdf [Accessed: 1-Nov-2016].
[2] "International Energy Agency" [Online]. Available: http://www.worldenergyoutlook.org/weo2015/ [Accessed: 10-Nov-2016].
[3] "The Kaya Identity" [Online]. Available: https://www.e-education.psu.edu/meteo469/node/213 [Accessed: 11-Nov-2016].

(2009), Myers and Bahaj, (2010), McTavish et, Al., (2013), Franchini, et al, (2016)]. Because of this, these studies have missed an important part of the characteristics of the real-world flows, since river, tidal and ocean current flows typically experience high turbulence intensities. Thus, it is beneficial to use a turbulent inflow that is close to the real-world flow characteristics in laboratory water channels in order to study the influence of this turbulence on hydrokinetic turbines. This will show the importance of testing these rotors in turbulent conditions compared testing in very low turbulence inflow conditions that are experience in typical lab scale testing campaigns.

This thesis therefor investigates hydrokinetic energy systems, including investigation of the properties of real turbulent flow in a real river, and the possibility of generating self-similar turbulence in a water tunnel rotor test using fractal grids. This will allow the study of hydrokinetic turbines performance in conditions much more representative of real-world operating conditions.

1.2 Hydrokinetic energy

According to Marine Renewables Canada group, in the next few decades, hydrokinetic energy could be commercialized because of its a relatively high energy density relative to other options[4]. Canada has significant hydrokinetic energy potential in the tides and river currents. It is estimated theoretically that Canada has tidal potential of about 370 TWh/year, and although river currents although not fully assessed yet, are assumed to range from 350 – 1500 TWh/year[4]. This compares to theoretical near shore and off shore wave combined potentials of 1863 TWh/year. However, the total actual extractable amount of energy from marine renewable energy resources is estimated at 35,700 MW when considering deployment limitations and losses.

Approximately 18.9 per cent of Canada's total primary energy supply is currently provided from renewable energy sources. Canada is the second largest producer of hydroelectricity in the world, contributing 59.3 % of Canada's electricity generation and hydrokinetic energy is considered as

[4] "Marine Renewables Canada" [Online]. Available: http://www.marinerenewables.ca/ [Accessed: 11-Nov-2016].

very important renewable energy source in Canada[5]. Water currents (river/tidal) is driven by gravity rather than by weather, this might allow of extracting predictable hydrokinetic energy and deliver continues power. Hydrokinetic turbines are suitable for remote power applications [Batten, et al., (2006), Birjandi, (2012)]. The Annapolis tidal station in Nova Scotia harness tide energy, that the Bay of Fundy has, to produce 80-100 megawatt hours of electrical energy daily[6]. The Robert H. Saunders St. Lawrence Generating Station is a great example of stations that harness river energy. The station is located on the Saint Lawrence River. It produces 3% of Ontario's power[7].

Like wind turbines, hydrokinetic turbines work on similar operating principles to extract kinetic energy from free-flowing water currents. Old operating concepts rely on drag forces to turn the device's shaft. These results in low efficiency and a low percentage of extracted kinetic energy. This low efficiency can be increased to exceed 50% when using lift to generate torque with respect to the axis of rotation. These lift driven turbines were introduced in the early decades of the twenty century. More serious work and development of wind turbines started later in the 1970's. Hydrokinetic turbines did not receive serious interest until the early 2000's. Generally, horizontal axis hydrokinetic turbine (HAHT) and vertical axis hydrokinetic turbine (VAHT) are the two types of lift-driven hydrokinetic turbines used to harness the power of the water's kinetic energy [Batten, et al., (2006), Birjandi, (2012)], Figure 1.1. They are classified based on the orientation of the rotor axis relative to the mean water flow direction. The vertical or cross-flow turbine is a type of hydrokinetic turbine in which the rotational axis is orthogonal to the flow direction. In contrast to the vertical axis turbine, where the rotor axis is orthogonal to the water surface, the cross-flow turbines have rotor axis parallel to the water surface [Khan, et al., (2009)]. On the other hand, the HAHT axis is parallel to incoming water stream [Batten, et al., (2008), Mukherji, (2010)]. Over part of the rotor's azimuthal sweep, VAHT blades are not working at an optimal angle to generate lift; they therefor are less efficiency than HAHTs. This has been borne out by experience, in that

[5] "Marine Energy Technology Team" [Online]. Available: http://publications.gc.ca/site/eng/384654/publication.html [Accessed: 20-Nov-2016].
[6] "Nova Scotia Power" [Online]. Available: http://www.nspower.ca/ [Accessed: 20-Nov-2016].
[7] "Canadian Electricity Association" [Online]. Available: http://powerforthefuture.ca/future-project/robert-h-saunders-generating-station/ [Accessed: 20-Nov-2016].

HAHTs have less vibration and more uniform lift forces than VAHTs [Khan, et al., (2009)]. In the VAHTs, the placement of the generator, gearbox, and bearings can potentially be above water level, which simplifies installation and avoids the requirement for a waterproof sealed bearing. Beside this, there is no yawing mechanism needed for keeping the axis aligned with the flow. However, the dynamic complexity of the turbines' operation has contributed relatively less commercial development.

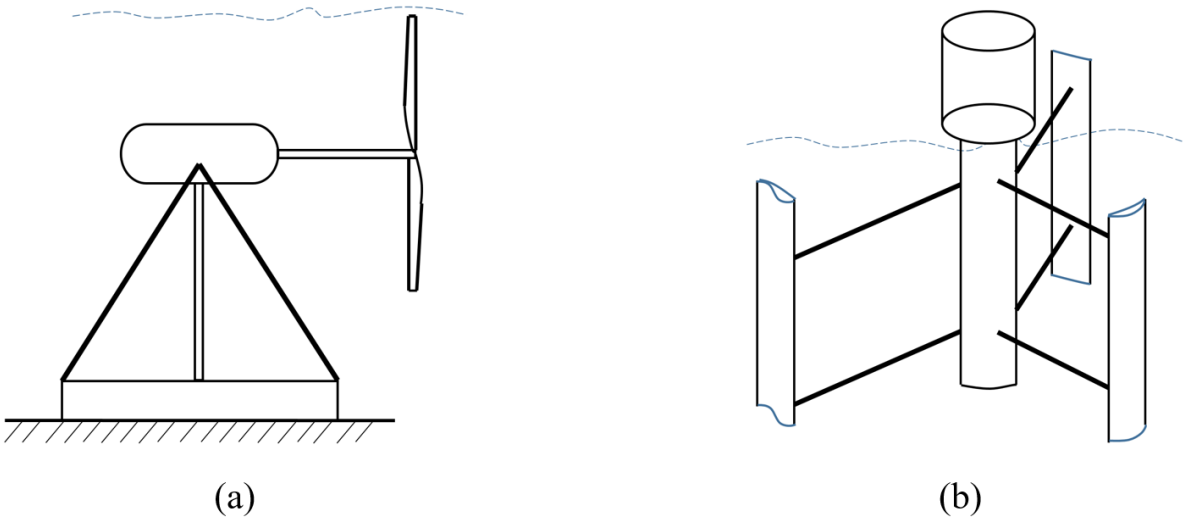

Figure 1-1: (a) A horizontal axis turbine. (b) A vertical axis turbine

1.3 Basics of turbulence

The randomly disordered motion of fluid vortices and their interaction are referred to as turbulence. Turbulent motion is the natural state of most fluids at device scales of interest for hydrokinetic energy [David, (2016)]. Although turbulence is still one of the most complex problems in physics, in recent years, turbulence research has increased and our understanding of the topic continues to improve. Richardson (1922) said that turbulence flow consists of a wide variation of length scales, scales of eddy motions, and time scales. Length scales cover a very wide range, and define the characteristic length scales for the eddies. These scales range from the macroscale at which the fluid kinetic energy is supplied, to a microscale at which energy is dissipated by viscosity. Energy is transferred from mean steady flow on large scales through the creation of large eddies. The large-scale motions are strongly influenced by the geometry of the flow and boundary conditions, which controls the transport and mixing within the flow. The large eddies break up in increasingly

smaller eddies, so that the kinetic energy of the initial large eddy is divided into the smaller eddies that stemmed from it. The energy is transferred from a large scale gradually to the smaller ones in a process known as the turbulent energy cascade. This process continues until reaching a sufficiently small length scale (known as the Kolmogorov length scale) such that the viscosity of the fluid can effectively dissipate the kinetic energy into internal energy [Marcuso, (2012)]. The behavior of the small-scale motions may be determined by the rate at which they receive energy from the large scales, although they are also influenced by the viscosity of the fluid. Therefore, these small-scale motions have a universal character, independent of the large-scale flow geometry. The amount of energy that is passed down from the large to smaller scales during this cascade process is randomly distributed [Kolmogorov, (1941)]. However, if the state of turbulence is statistically steady (statistically unchanging turbulence intensity), then the rate of energy transfer from one scale to the next must be the same for all scales, so that no group of eddies sharing the same scale sees its total energy level increase or decrease over time. It follows that the rate at which energy is supplied at the largest possible scale is equal to that dissipated at the shortest scale.

The governing equation for incompressible fluid motion, without external forces, is a form of the Navier-Stokes equations, which fundamentally include turbulence at sufficiently large scales, expressed as:

$$\frac{\partial \vec{u}}{\partial t} + (\vec{u} \cdot \nabla)\vec{u} = -\frac{1}{\rho}\nabla p + v\nabla^2\vec{u} \qquad \textbf{(1-1)}$$

where $\vec{u}$ is the flow speed, ρ the flow density, p the pressure and v the kinematic viscosity. $(\vec{u} \cdot \nabla)\vec{u}$ is called the inertia term and describes the convective acceleration of the fluid particles as they move with the flow [David, (2016)]. The dissipative or viscous term $v\nabla^2\vec{u}$ describes the internal friction of the flow due to its viscosity. The general expression for mass conservation is:

$$\frac{\partial \rho}{\partial t} + \nabla \cdot (\rho\vec{u}) = 0 \qquad \textbf{(1-2)}$$

For incompressible flow the above continuity equation is reduced to:

$$\nabla \cdot \boldsymbol{u} = 0 \qquad \textbf{(1-3)}$$

This equation means that the total convection of mass into the control volume minus that convected out of the control volume is zero for a constant density flow. For turbulent flow, the instantaneous velocity can be expressed as a fluctuation component and a mean component:

$$u_j = \bar{u}_j + u_j' \tag{1-4}$$

Also,

$$\rho = \bar{\rho} + \rho' \tag{1-5}$$

By substituting this into Eq. 1.2:

$$\frac{\partial \bar{\rho}}{\partial t} + \frac{\partial (\bar{\rho}\bar{u}_j)}{\partial x_j} + \frac{\partial (\overline{\rho' u_j})}{\partial x_j} = 0 \tag{1-6}$$

The momentum equation is defined as:

$$(\rho \delta V)\frac{D\vec{u}}{Dt} = -(\nabla p)\delta V + viscous\ forces \tag{1-7}$$

where, δV is a lump of fluid of volume. This equation states that the mass of the fluid element $\rho\delta V$ times the acceleration $\frac{D\vec{u}}{Dt}$ is equal to the net pressure force acting on the fluid element, plus any viscous forces arising from viscous stresses [Marcuso, (2012)]. The ratio of inertial force to viscous force is defined by a dimensionless Reynolds number. Considering a flow with velocity U and a characteristic length scale L, the flow fluid has dynamic viscosity μ and density ρ. The large Reynolds number is defined as:

$$R_e = ratio = \frac{Inertia\ Force}{Viscous\ Force} = \frac{\rho\ U\ dU/dx}{\mu\ d^2U/dx^2} = \frac{\rho\ U\ U\ /L}{\mu\ U/L^2} = \frac{\rho\ U\ L}{\mu} \tag{1-8}$$

The detailed motion of every eddy in turbulent flow is very hard to predict. It is common that a statistical approach is used to describe the stationary turbulent flow because of the fact that some of its statistical properties are repeated through the turbulence cascade. The statistical measures used in this work are defined as follows:

- The time averaging flow speed:

$$\bar{u}(t) = \frac{1}{\Delta t}\int_t^{t+\nabla t} u(t)dt \tag{1-9}$$

- The fluctuation velocity:

$$u'(t) = u(t) - \bar{u} \tag{1-10}$$

- The standard deviation of the fluctuation:

$$\sigma_u = \sqrt{\overline{u'(t)^2}} \tag{1-11}$$

- 3D turbulent intensity:

$$TI = \frac{\sqrt{\frac{1}{3}(\overline{u'^2} + \overline{v'^2} + \overline{w'^2})}}{\sqrt{(\bar{u}^2 + \bar{v}^2 + \bar{w}^2)}} \tag{1-12}$$

- Streamwise turbulent intensity:

$$TI = \frac{\sigma_u}{\bar{u}} \tag{1-13}$$

- Turbulent kinetic energy:

$$TKE = \frac{1}{2}(\bar{u}^2 + \bar{v}^2 + \bar{w}^2) \tag{1-14}$$

- The skewness:

$$S = \frac{\overline{u'^3}}{{\sigma_u}^3} \tag{1-15}$$

- The flatness:

$$F = \frac{\overline{u'^4}}{{\sigma_u}^4} \tag{1-16}$$

- Reynolds stresses:

$$R = \begin{bmatrix} \overline{u'u'} & \overline{u'v'} & \overline{u'w'} \\ \overline{v'u'} & \overline{v'v'} & \overline{v'w'} \\ \overline{w'u'} & \overline{w'v'} & \overline{w'w'} \end{bmatrix} \tag{1-17}$$

where,

$$\overline{u'u'} = \overline{(u - \bar{u})(u - \bar{u})}$$

$$\overline{v'v} = \overline{(v - \bar{v})(v - \bar{v})}$$

$$\overline{w'w'} = \overline{(w - \bar{w})(w - \bar{w})}$$

$$\overline{u'v'} = \overline{(u - \bar{u})(v - \bar{v})}$$

$$\overline{u'w'} = \overline{(u-\bar{u})(w-\bar{w})}$$

$$\overline{v'w'} = \overline{(v-\bar{v})(w-\bar{w})}$$

1.4 River turbulence

In general, riverine flows are typically in a state of turbulence. River turbulence is still a challenge for researchers and engineers working in hydraulics and fluid mechanics [Franca and Brocchini, (2015)]. Some of the river turbulence energy is derived from the meandering of flow, wakes of piers, sand waves on the bottom, and so on. The main force that drives open channel flows is gravity [Kaji, (2013); Franca and Brocchini, (2015)]. The size of the eddies produced by the above causes are on the order of magnitude as the size of the causes. If there are no sand waves, no obstacles and no meandering in a river channel, in each region, there exists the so-called inertial subrange, in which no production and no dissipation of energy take place and only energy transfer to smaller and smaller eddies occurs because of the sufficiently large Reynolds number of the river flow. Rivers can be regarded as open-channel flows with highly heterogeneous beds and irregular boundaries [Franca and Brocchini, (2015)]. River flow is restricted by the free surface and the bottom vertically, and by the width of channel horizontally.

In open channel flows, the turbulence in the flow in the region away from the bed is highly effected by the depth (D) and the maximum streamwise velocity near the free surface [Nezu and Nakagawa, (1993a), Kaji, (2013)]. At the river, each bed slope can cause the depth and velocity to vary from upstream to downstream that the water surface will not be parallel to the bed. River flow is usually characterized by a large ratio of width to water depth. In rivers, parameters such as the width (W) of channel, water depth (D) and furthermore the smallest scale (Kolmogorov microscale) (λ) can be used to characterize the river turbulent structure [Yokosi, (1967), Sukhodolov, et al., (1998)]. Yokosi reported that turbulence properties near the river bed are similar to that of well-known wall turbulence. The largest scales in the flow in the horizontal plane have a size of the order of the dimension of the region in which the flow takes place. On the other hand, the smallest eddies in the flow have a size of about 1mm. Moreover, most of the river turbulent energy dissipates in eddies smaller than 1 cm, whose turbulence Reynolds number (R_λ) is comparable with unity.

The energy is transferred from the largest eddies scales which break-up to form smaller eddies and these further break-up and so on till small eddies scales such that the flow returns to laminar inside the very small eddies and the kinetic energy is small enough to be dissipated by viscosity. This dissipation happened because of the friction force that opposes the flow and dissipate the energy and turns it into heat as the organized motion of the 'molecules' turns from a straight path into a chaotic one. Also, the circular motion inside the eddy has its maximum flow velocity in the outside edges from which it derives its energy to exist, and a zero velocity at its center. The resulting gradient in velocity between the outer and inner regions of an eddy results in friction due to viscosity and further loss of energy.

Yokosi (1967) confirmed that the energy spectral density is described by the well-known Kolmogorov -5/3 power law in both horizontal and vertical turbulence. Nikora (2007) in his study presented interpretation of how the flow energy is distributed through temporal and spatial scales present in fluvial systems. Nikora reported that the shapes of the rivers can be completely changed by floods with return periods of years, or even centuries. River boundaries such as the grain roughness, river bed form and channel protrusions have strong influences on the generation of the river turbulence. At the same time, these river boundaries are continuously shaped by the turbulent structures. Rivers have highly heterogeneous beds and irregular boundaries [Yokosi, (1967)]. This can impact the riverine flow structure and, therefore, generate different scales of turbulence [Nezu and Nakagawa, (1993a), Kaji, (2013)]. The morphology of the river can be shaped continuously throughout a long period of time by energetic currents that are generated locally.

Nikora stated that the distribution of the flow energy through the spatial scales on the order of greater than kilometer adjusts the amount of water, sediments and organic matter arriving at a given river section. Moreover, other scales can be locally introduced to the flow, these scale are caused by natural obstacles (e.g., riffles, pools, tree trunks, and root wads) and man-made structures (e.g., bridge foundations, groynes, and stream restoration structures). The smallest scales can be related to micro-organisms and to viscous processes such as diffusion and energy dissipation. The smallest time scales are orders of magnitude smaller than seconds. These times scales are related to the energy dissipation process. An adequate momentum might be transmitted to promote sediment entrainment and suspension by turbulent structures that have time scales on the order of seconds [Nikora, (2007)].

Measurement and analysis of the three-dimensional turbulence structure in a straight lowland river was conducted by [Sukhodolov, et al., (1998)]. They observed that the flow can be considered weakly three-dimensional in the central part of the river and the river turbulence is isotropic for spatial scales smaller than the river depth. Yokosi stated that in the region between Kolmogorov microscale (λ) and the river depth (D) in the spectrum of the river turbulence the turbulence is 3D. the vertical turbulent component is characterized by the vertical scale D and the horizontal turbulence by width scale W. Consequently, the energy dissipation different between the vertical and horizontal turbulence. The statistical properties of turbulence are assumed to be independent in the vertical and horizontal turbulence [Yokosi, (1967), Sukhodolov, et al., (1998)]. The scale of turbulence is very much larger horizontally than that of vertical turbulence given typical flow channel dimensions. The dynamic behavior of river flow on the scale of the water depth seems to be contributed by the turbulent motion on the scale of the largest eddies of vertical turbulence. This turbulent motion seems to correspond to a dominant circulation with a diameter on the order of depth around a longitudinal axis and to the streets of spots observed on the surface of a river. The Kolmogorov energy cascade is obeyed for horizontal turbulence and energy may be transferred to smaller and smaller eddies by a cascade process to vertical turbulence through the transitional region by the action of turbulent viscosity [Yokosi, (1967)].

1.5 Ocean turbulence

The general characteristics of turbulence in the ocean are similar to those in rivers described in section 1.4. As mentioned in the previous section, the large scales of turbulence in a river are related to the geometry of the river, depth and width. Ocean turbulence exists over a wide range of scales, from a few centimeter to large scales which can be thousand of kilometers. The ocean motions are forced by the large-scale atmospheric winds and tides. These different scales continuously interact again with the energy ultimately dissipated as heat at the smallest scales. Mackenzie and Leggett (1993) collected oceanic data for different stations and found that the turbulence in oceanic environments is driven by the shear stress induced by wind at the ocean surface. Gargett (1989) reported on measurements of turbulence in the stress-driven bottom boundary layer. Stress is particularly important as a measure of the effect of turbulent water motion on a sedimentary ocean bed, and its magnitude determines whether and how sediment is moved

by the flow of water. Frictional forces can be exerted on ocean bottom by transport of momentum from ocean currents and waves through a boundary layer [Williams, et al., (1987)]. The turbulent kinetic energy in the surface layer of the ocean should be mainly produced from breaking waves [Ardhuin and Jenkins, (2006)]. This occurs mostly through the large shear at the forward face of these breaking waves. Ocean surface waves, tidal current, and ocean current have turbulent motions and they are resources of ocean energy which are collectively referred to as marine renewable energy. Understanding turbulence in the ocean should lead to improvement the ocean energy technologies that are used to convert these resources to a useful form.

1.6 Fractal grid turbulence

Fractal grids have been used to generate turbulence in water tunnels and wind tunnels [Queiros & Vassilicos, (2001); Staicu, et al., (2003); Hurst and Vassilicos, (2007); Seoud and Vassilicos, (2007); Mazellier and Vassilicos, (2010); Stresing, et al., (2010); Discetti, et al., (2011); Laizet and Vassilicos, (2011); Valente and Vassilicos, (2011a, b); Cardesa and Nickels, (2012); Gomes, et al., (2012); Stefan, et al., (2013); and Hearst, (2015)]. Fractal grids are rigid structures with constant solidity that result in turbulent flows with specific patterns and statistics. Various patterns for fractal grids can be characterized as I pattern, cross pattern and square pattern (see Figure 1.2). Each pattern generate turbulence with different properties; more details on this can be found in section 3.2.

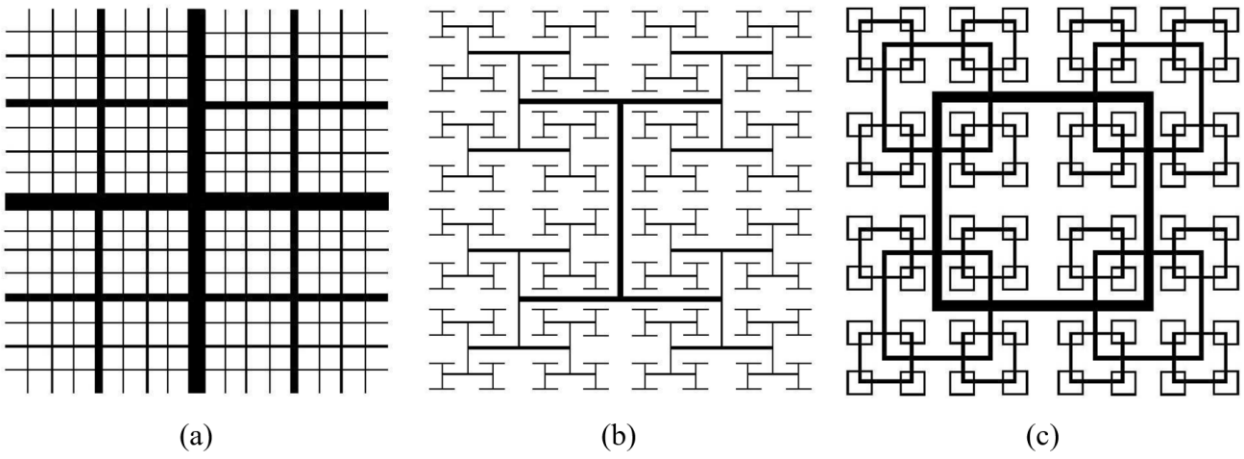

Figure 1.2: Fractal grids patterns: (a) Cross pattern (b) I pattern (c) Square pattern. Adapted from [Hurst & Vassilicos, (2007)]

The space filling square pattern is the one has been selected in this work. The fractal square grid has the ability to generate controllable turbulence build-up and decay rates. It generates turbulence by creating different sizes of many vortices with corresponding levels of interaction as illustrated in Figure 1.3 [Mazellier and Vassilicos, (2010); Hurst & Vassilicos, (2007)]. The main interaction events occur when similar sized wakes meet; the bars have different sizes and are placed at different distances from each other, so the turbulence is generated from a range of wakes interacting which are created by these different bars at different locations downstream [Mazellier and Vassilicos, (2010); Laizet and Vassilicos, (2011)]. The smallest wakes meet and mix together at locations closer to the grid compared to the larger wakes. In general, fractal grids can generate turbulence with high Reynolds numbers compared with turbulence generated by regular grids at the same flow speed [Seoud and Vassilicos, (2007)]. Fractal grids generate turbulence which has two regions, one close to the fractal grid and the other further downstream as seen in Figure 1.3, [Mazellier & Vassilicos, (2010); Laizet & Vassilicos, (2011)]. The turbulence build-up in the production region reaches a peak (intensity peak) at x_{peak}downstream of the grid, as shown in Figure 1.3, decaying exponentially downstream [Hurst &Vassilicos, (2007)]. The turbulence in the near production region is anisotropic and non-Gaussian, becoming isotropic and Gaussian further downstream in the decay region. The properties of the fractal generated turbulence are strongly influenced by the smallest and largest scales in the grid, as well as some other grid parameters [Hurst and Vassilicos, (2007); Seoud and Vassilicos, (2007); Mazellier and Vassilicos, (2010); Stefan, (2011)].

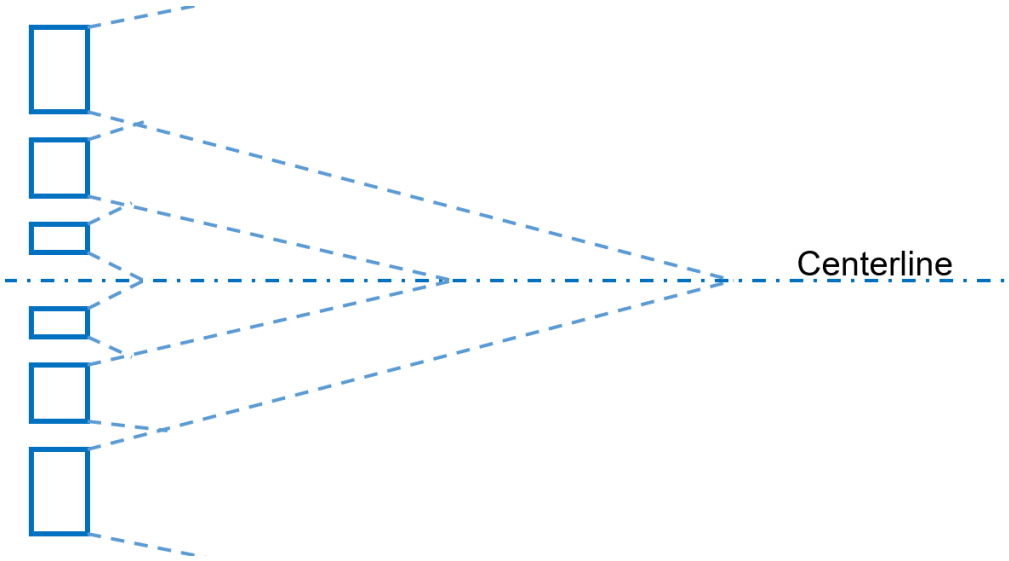

Figure 1-2: Sketch of wake interactions resulting from the fractal grid's bars

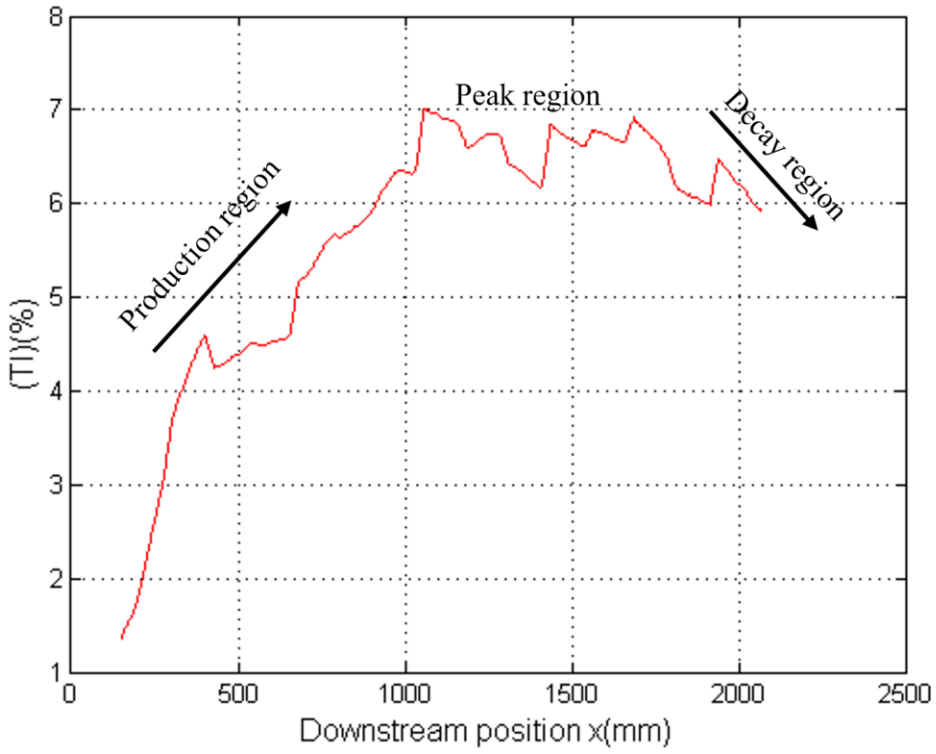

Figure 1-3:Turbulence regions downstream fractal grid

1.7 Objectives

As the population is increasing, energy demand and energy consumption are also increasing. This leads to more environmental pollution emissions, which is coming primarily from the combustion of fossil fuels and bioenergy. So, the current concern of the world is to manage and reduce pollution by depending more on renewable energy. This means that the globe is in dire need of more developments of renewable energy technologies and thereby drive toward sourcing a higher percentage of our primary energy from renewables. Therefore, the main goal of this thesis is to help in develop one of renewable energy technologies (hydrokinetic energy systems) by conducting field and experimental studies. These studies have objectives (which leads to the main goal of the thesis) such as characterizing the effect of fractal grid turbulence on the performance of hydrokinetic turbines. Other objectives were undertaken, such as the design of a fractal space filling square grid specifically for the UVic water tunnel to generate turbulence with the required turbulent properties. This grid was intentionally designed so it can be used in the future for other experiments. Moreover, another important aspect in this thesis is to provide real turbulence properties such as river turbulence by doing a field study in the Winnipeg River. This field study helped to inform the generating turbulent flow in the water tunnel in a way that the generated turbulence was similar to real turbulence. The present work started with field measurements to characterize the properties of the river turbulence. Fractal square grids were then designed and manufactured to generate turbulence in the water tunnel. A design study was done for some of the grids to select the proper grid to generate turbulence with specific characteristics. The selected grids were then placed upstream of the turbine. Detailed performance behavior of a small-scaled tidal turbine (horizontal axis tidal turbine) in the generated turbulent flow condition was investigated in the water tunnel to quantify the effect of turbulence on the performance of the turbine by comparing the results with other results that have been collected in smooth flow in the same water tunnel with the same rotor.

Particle Image Velocimetry (PIV) techniques were used in the experimental study to record and obtain quantitative information about the vector flow field along the channel downstream the grid, and also upstream of the rotor plane. Flow measurements were obtained started immediately downstream of the grid to all the way till the end of the channel. The intension was to decide on

the correct place for the rotor to be installed at. Other flow measurements were obtained, after the rotor had been installed, upstream the rotor.

1.8 Contributions & Thesis Outline

This thesis consists of five chapters. Chapter 1 has provided an introduction and motivation for the work. Chapter 2 presents field measurements of river turbulence, covering in-situ measurement results of velocity measurements of a river at different depths from free surface to the river bed. This chapter also includes laboratory study to investigate the effect of the ADV orientation on the data collection and also the effect of transferring the data to a local frame. Chapter 3 presents laboratory measurements of fractal generated turbulence and results and the effect of the fractal parameters on the turbulence properties. Chapter 4 details an experimental study of fractal generated-turbulence influence on horizontal axis hydrokinetic turbine performance and chapter 5 provides conclusions and recommendations.

Chapters 2-4 of the thesis have been assembled as a collection of papers to be submitted for publication:

[1] Mahfouth A., Birjandi A. H., Crawford C., and Bibeau E. L., “Turbulence Characteristics Through the Water Column in an Open Channel for Hydrokinetic Turbine Deployment” Marin Energy, (2016).

[2] Mahfouth A., and Crawford C., “An experimental study of fractal grid generated-turbulence using PIV,” (2016)

[3] Mahfouth A., and Crawford C., “An experimental study of fractal generated-turbulence influence on horizontal axis hydrokinetic turbine performance,” (2016)

Chapter 2

2 Turbulence Characteristics Through the Water Column in an Open Channel for Hydrokinetic Turbine Deployment

Authors: Altayeb Mahfouth[1], Amir Hossein Birjandi[2], Curran Crawford[1], Eric L. Bibeau[2]

[1] Dept. of Mechanical Engineering, University of Victoria, BC

[2] Dept. of Mechanical Engineering, University of Manitoba, MB

To be submitted

2.1 Abstract

For the first time an accurate velocity measurement is conducted from the free-surface to boundary layer region of a fast current channel using an acoustic Doppler velocimeter (ADV). Flow characteristics in a river or open channel, including mean flow velocities and turbulence intensity profiles, are essential information for marine and hydrokinetic energy industry in site selection, engineering design, commissioning and operation phases. In this contribution, we introduce a novel technique to deploy and control an ADV from free-surface to boundary layer of a fast-current channel to improve the accuracy of the flow data obtained from traditional techniques such as acoustic Doppler current profiler (ADCP) or single point ADV (e.g. near surface or near channel bed). The knowledge of true flow characteristics and turbulence properties at different depths in a fast-current river or channel can lead to a better performance evaluation, lifetime estimation and power output prediction. This investigation is conducted at the Canadian Hydro Kinetic Turbine Test Centre (CHTTC) on Winnipeg River. Results indicate that the maximum mean velocity

occurs at about 3 m below the free-surface, independent of channel depth and mean velocity, and drops by 34% at 0.8 m above the channel bed, in the boundary layer region. Therefore, flow in this region carries only 29% of the energy that the flow has in the maximum velocity point. Turbulence intensity has a reversed pattern and increases near the channel bed. The free-surface to half depth changes are gradual, both in mean velocity and turbulence intensity. After mid-depth, mean velocity drops rapidly while the turbulence intensity increases in a fast rate.

Key Words: River Boundary Layer; Turbulence Measurement; Acoustic Doppler Velocimeter (ADV); Hydrokinetic Turbine, Marine Energy

2.2 Introduction

An essential requirement for optimizing the design of wind or water turbines and designing codes is obtaining turbulence data from field observations of the flow. Information about three-dimensional structure of turbulence has contributed to the current accuracy and reliability of designing marine turbines industry [Thomson, et al., (2012)]. Development of marine turbine requires detailed knowledge of the inflow conditions and the nature of its turbulence; indeed this knowledge is a key goal in the successful installation and operation of marine energy devices. IT Power Group (itp) has installed the world's first commercial scale marine current turbine[8]. IT Power Group reported that turbulence has effects on the engineering design, analysis or operation of marine power installations. Field observations of river flows and characterization of the turbulent properties, such as those presented in this paper, provide characteristic design conditions for hydrokinetic turbines. Significant fluctuations in loading may be applied to marine current turbine by fast velocity changes resulting from large scale turbulence [Osalusi, et al., (2009)]. Turbine performance, structural fatigue and the wakes of individual turbines have been shown to be correlated with turbulent properties of the flow, such as the turbulence intensity and the turbulent spectra [Kelley, et al., (2005); Frandsen, (2007); Thomson, et al., (2012)]. Osalusi (2009) stated that turbulence in the inflow causes cyclic loads (that are imposed upon the turbine) that continually pose a threat of fatigue damage to the turbine, and these loads drive the design of

[8] "IT Power Group" [Online]. Available: http://www.itpowergroup.com/ [Accessed: 20-Oct-2016].

modern marine current turbines. Changing of the speed and direction of the flow with the depth and the influence of the free surface have significant effects on the hydrodynamic design of marine current turbines [Batten, et al., (2006)].

The use of computational tools is rapidly developing for investigating flow structures in river environments. Flow structure in rivers are considered one of the main factors affecting the character and the intensity of several river processes, such as flow resistance and sediment transport etc. [Gimbert, et al., (2014)]. The need to improve understanding of flow structures in rivers is important for developing numerical models [Ge, et al., (2005); Thomson, et al., (2012); Sulaiman, et al., (2013)]. The development of computational models face some difficulties; one of these difficulties is that there are not enough detailed reliable measurements to validate models. At the same time, it might not be possible for these models to simulate the turbulence at all relevant scales [Sanjiv and Odgaarrd, (1998); Thomson, et al., (2012)]. Experimental measurements of turbulence and acquiring turbulence data in natural rivers are pressing needs [VanZwieten et al., (2015)]. To validate a numerical model of a river, field and laboratory investigations have to be conducted in order to collect reliable data for verification purposes. Validation with laboratory data at fixed flow conditions is easier than with natural confluence data [Kalyani, (2009)]. However, even though laboratory experiments allow researchers to check the effects of the main determinants of flow structure, there are still boundary condition values that need to be considered. Thomson 2012 argues that the turbulent flow must be estimated from field measurements. Boundary condition values in a numerical model of a river channel can be controlled much more easily than if an experimental design for the channel had been conducted in a laboratory [Lane, (1998)]. Velocity patterns of a river channels may be possible to be replicated by numerical models that have been tested using field data [Olsen, (1995); Nicholas and Smith (1999); Booker, (2001)].

During the past three decades, research studies have been undertaken to measure the flow and turbulence characteristics in open channels starting in the 1970s [Nakagawa, et al, (1975)]. In these investigations different devices and configurations have been used for flow measurements such as Laser Doppler Velocimeters (LDV), micropropellers, time-of-flight acoustic type current meters, electromagnetic current meters and Pitot tubes [Kraus, et al., (1994)]. A primary necessity for analyzing a turbulent flow is to collect high frequency velocity signals in at least two planes. Optical tools are impractical for field measurements due to their limited penetration in murky

waters. Electromagnetic current meters (ECMs) have been commonly used to measure turbulence quantities in field studies [McLelland and Nicholas, (2000)]. However, Voulgaris and Trowbridge (1997) reported that electromagnetic current meters are able to measure only two components of the flow and they are inappropriate for resolving fine scales of turbulence. Studying the turbulence characteristics in an open channel requires the use of rapidly responding flow-measuring devices that can read fluctuating flow in three-dimensional directions (streamwise, transverse & vertical) [Voulgaris and Trowbridge, (1997); Sulaiman, et al., (2013)]. Garde, (2000) stated that the turbulence quantities of a flowing fluid can be measured by identifying the changes in mechanical, physical and chemical nature in a detection element that is immersed into the flowing fluid.

Around two decades ago, researchers started to replace 2D- measurement devices such as electromagnetic current meters, propeller meters, hot-film anemometers, etc. with the Acoustic Doppler Velocimeter (ADV). ADV was designed initially by the U.S. Army Engineer Waterways Experimental Station and SonTek in 1992 to measure 3D velocity in lab and field environments [Lohrmann, et al., (1994); Kraus, et al., (1994); Nikora and Goring, (1998)]. Voulgaris and Trowbridge (1997) have examined the accuracy of ADV sensors in the laboratory to measure turbulence and they found that the ADV mean flow velocities are accurate to within 1%. However, Chanson, et al., (2008) highlight the need for further field data and research on the use of ADVs for determining turbulent flow properties. Acoustic Doppler velocimetry has been recognized to be sufficiently robust to provide instantaneous three-dimensional velocity information for natural rivers.

Usually, rivers have vigorous environment conditions; therefore, field measurements in a river require a device that is able to collect high quality data under robust changeable environmental conditions. Despite the fact that ADV has been commonly used as the in-situ measurement device at field scale [e.g. Lane, et al., (1998); Sukhodolov and Roads, (2001); Fugate and Friedrichs, (2002); Kim, et al., (2003); Carollo, et al., (2005); Tritico and Hotchkiss, (2005); Andersen, et al., (2007); Stone and Hotchkiss, (2007); Strom and Papanicolaou, (2007); Lacey and Roy, (2008); Chanson, et al., (2008); Sulaiman, et al., (2013); VanZwieten, et al., (2015)], setting up the measurement device in a river environment to conduct measurements at different depths is quite challenging due to the change river flow conditions. Thus, in this study, an innovative technique for deploying and orienting the ADV is introduced to obtain high frequency velocity data at

different depths, from free surface to the river bed. It has been highlighted that ADV is a well suited measurement device for natural flows (at one stationary point) [Brunk, et al., (1996); Nikora, et al., (1998); Goring, (2000); Fugate and Friedrichs, (2002); Chanson, et al., (2008)]. Compared to optical and laser techniques, ADV is simple and compact, as the acoustic emitter and receivers are installed within a common device. Additionally, acoustic waves penetrate deeper in water when compared to light or laser beams [Duraiswami et al., 1998]. Because of these advantages, ADV is widely used by researchers for flow velocity measurements in laboratory and field applications [Chansona et al., 2008, Sarker, 1998, Trevethan et al., 2007, Trowbridge and Elgar, 2001 and Wilcox and Wohl, 2006].

This paper is concerned with field investigation of flow structures in a river. In this work, ADV was used to record instantaneous velocity components at a single-point in the x, y, and z directions with a frequency of 64Hz. Measurements were conducted at the Canadian Hydrokinetic Turbine Test Centre (CHTTC) site located on the Winnipeg River in the tailrace of the Seven Sisters generating station, Manitoba, Canada. The CHTTC is a test facility for river hydrokinetic turbines which provides a standard condition to test these technologies. These measurements were conducted at different locations along the river at various depths in the water column, from the surface to the bottom of the river. To our knowledge, this is the first time that ADV has been employed to measure turbulence characteristics in the water column of a fast current stretch of a river at various depths. It is anticipated that the results of this study will help lead to performance improvements for hydrokinetic turbines, as well as fundamental understanding of turbulence in rivers.

2.3 Test site

In this study, the velocity measurements were conducted at three locations along the CHTTC site, Figure 2.1. The CHTTC is a national test center for river hydrokinetic technologies that allows manufacturing companies to test their products in a real condition environment. The test center is located at the tailrace of the Seven Sisters power generating station on the Winnipeg River. High turbulent flow and variable flow rate are main characteristics of this site which attracts marine turbine manufacturers and developers for life-cycle project solutions and fully grid integrated systems. The CHTTC site is a manmade channel 1 km long curved in granite bed with average

width of 60 m and the depth between 9 and 12 m. On average the, CHTTC site maintains a current speed in the range of 1.7 m/s to 3.2 m/s. Due to the high flow velocity, channel remains unfrozen at the site even during cold days of the winter. Harsh winter temperature at the site, -30°C and bellow for couple of weeks, provides the opportunity for companies to test their technology for cold climate environment. Since the test center is a manmade channel carved in granite bed rock, the cross-section shape of the channel is close to a perfect rectangular, with right angle edges and reasonably smooth bed contour with no considerable roughness, large boulders or hydraulic jumps.

Figure 2-1: Satellite image of the CHTTC site and measurement locations

2.4 Experimental apparatus

To deploy the ADV at different depths through the water column, a customized rig was built to lower the ADV all the way to the bottom of the channel. The higher accuracy and resolution of the ADV compared to ADCP offers better understanding of turbulence characteristics and velocity profile along the channel depth. The ADCP beams diverge as they travel in the water column; therefore, at deeper levels of the water the measured velocity by ADCP represents the average velocity of a large volume of water which reduces the resolution and accuracy specifically in high

velocity gradient areas such as wake zones or boundary layer. ADCP measurements also suffer from two blank distances, one near the device head and the second one in proximity of the river bed. On the other hand, ADVs allow instantaneous velocity measurement at a single point at much higher frequency and accuracy [Nortek, A. (2005)].

The setup of the experiment is shown in Figure 2.2. The ADV is equipped with a stabilizing fin attached to the ADV that keeps the ADV axis stationary with respect to the inflow, the x, y and z frame of the ADV oriented such that x was aligned into the flow, y was aligned across the flow, and z direction was aligned upward. Swivels on the deployment line separate the ADV and the support structure from any torsion in the rest of the deployment line and let the ADV rotate freely along the deployment line. A support structure is designed to connect the ADV to the deployment line and it lets the ADV slide along the deployment line. The support structure is a C-channel that the deployment line passes through the c-opening and a control line attached to the top of the support structure enables the operator to adjust the depth of the ADV. A 30 m data cable connects the ADV to a computer in the pontoon boat; therefore the operator is able to monitor the depth and the signal quality simultaneously on the screen. For the measurements, first the pontoon is anchored stationary in the channel using two shore anchors, one attached to the left shore and one attached to the right shore. After the pontoon is secured in the channel, a heavy weight attached to the deployment line is winched down to the channel bed through the opening in the middle of the pontoon boat. The purpose of the weight is to keep the deployment line straight; therefore, when the weight reaches the bottom the extra slack on the deployment line is removed by the winch. Once the weight and the deployment line are secured the ADV is attached to the deployment line using the support structure and the control line is attached to the top of the support structure, as shown Figure 2.2. The ADV is sent down using gravity and the control line holds the ADV at specific depths. The operator reads the depth from the pressure sensor on the ADV. When the ADV reaches the desired depth it is secured by the control line and velocity data is recorded for approximately 7 minutes.

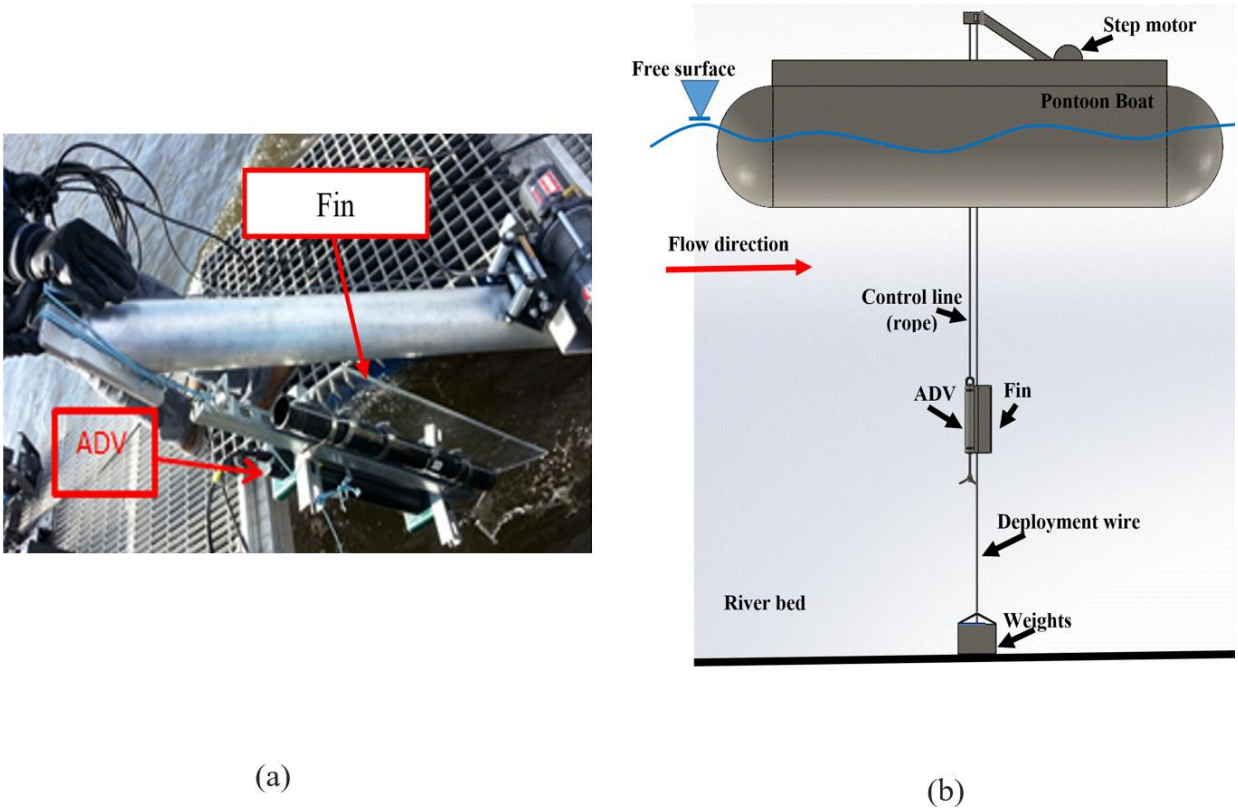

Figure 2-2: Setup the ADV in the river (a) mounting the ADV on the guiding wire at the opening in the middle of the pontoon boat (b) a sketch of the whole setup

2.5 Data filtering

It has been noticed that ADV raw field data demonstrates large populations of spikes in the data records [Nikora and Goring, (1998); Chanson, et al., (2008); Birjandi and Bibeau, (2009); Birjandi and Bibeau, (2011)]. These spikes are due to the combined effects of operating conditions, air bubbles, Doppler noise, signal aliasing, large particles and other disturbances. For instance, when floating sediments with a volume greater then sampling volume or acoustic wavelength of the ADV pass through the sampling volume, they cause aliasing of the Doppler signal. Nikora and Goring 1998, Goring and Nikora 2002 reported that Doppler noise has a significant effect on the measured turbulence properties; they introduced simple techniques to reduce the effect of these spikes on the turbulent characteristics. Birjandi and Bibeau 2011, developed a new method to eliminate spikes that are caused by signal aliasing and air bubbles. This method performs better compared to the Nikora and Goring method when the number of spikes is large and the standard deviation of the dataset is affected. Spikes may not affect the averaged velocity, but correlations

and statistical moments are significantly influenced by spikes. Thus, in order to quantify turbulence characteristics of the flow in the channel, the spikes have to be removed from the data.

Before any further data post-processing, the quality of the data is improved by removing sharp spikes from the dataset. Spikes are detected using a technique referred to as the hybrid despiking method proposed by [Birjandi and Bibeau, (2011)] where the spikes are replaced with linearly interpolated data using data on both sides of the spike; further information regarding the method see [Birjandi, (2011); Birjandi and Bibeau, (2011)]. Figure 2.3 demonstrates the effective performance of this method to remove spikes from a 60 s sample of ADV velocity data.

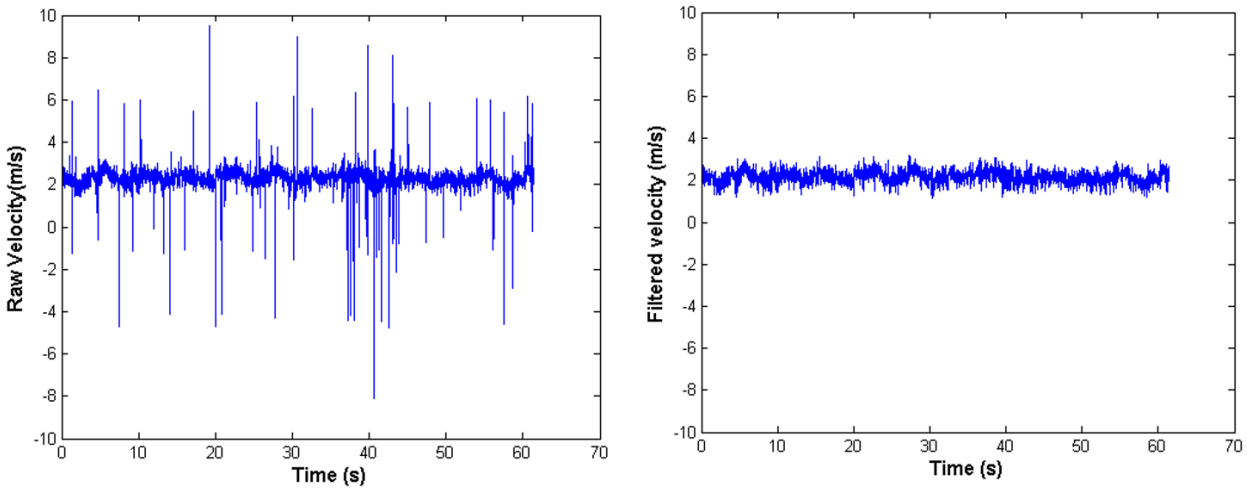

Figure 2-3: A segment of the streamwise ADV data collected at CHTTC site (a) Raw velocity data and (b) despiked velocity data

Figure 2.4 shows the number of spikes removed from the streamwise velocity dataset using the hybrid despiking method through the water column (the channel has a depth of 8.5 m). It has been noticed that the number of spikes decreases as the ADV moves deeper. A higher number of spikes near the free-surface can be blamed on the higher number of entrained air bubbles in this region according to the study conducted by Birjandi and Bibeau in the river [Birjandi and Bibeau, (2011)]. More studies on the general effect of air bubbles on ADV data can be found in [Mori, et al., (2007); Birjandi and Bibeau, (2011)].

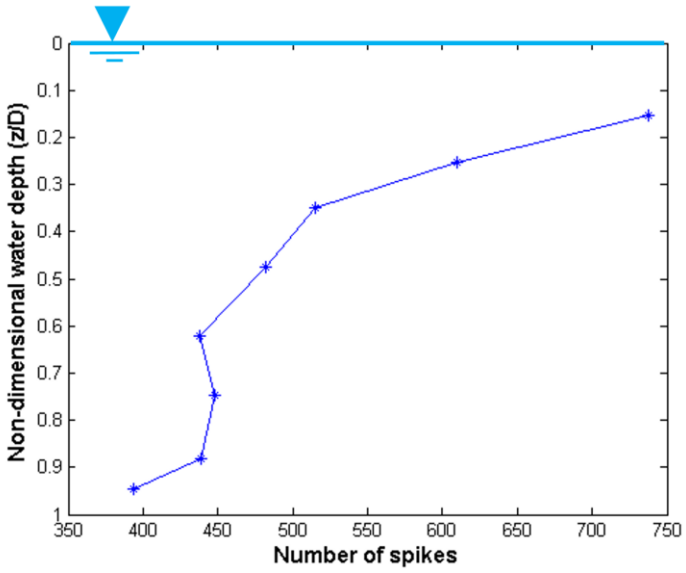

Figure 2-4: Number of spikes removed from the streamwise velocity data variation with depth

2.6 Angle correction

During the test in the channel, it was noticed that the ADV's body axis was not exactly aligned with the flow coordinate system. This disagreement was the result of many factors. The main contributors was the drag forces on the deployment line, control line and the ADV which caused a net pitch angle. Slight asymmetry in the support structure contributed to an effective yaw angle of the ADV, shown Figure 2.5.

The raw ADV data presents the velocity components in body reference system, the flow coordinate system is the relevant frame for data analysis, which breaks down the velocity into streamwise, transvers and vertical components. The velocity components in the flow coordinate system are obtained by transforming the velocity components from the body coordinate system. The first step in the transformation between the two coordinate systems is to determine the angles between the two coordinate systems. An analytical solution is developed to convert velocity components to the flow coordinate system. The data is adjusted in two steps. Step one rotates the data by the pitch angle $\emptyset$ and step two applies yaw angle θ transformation.

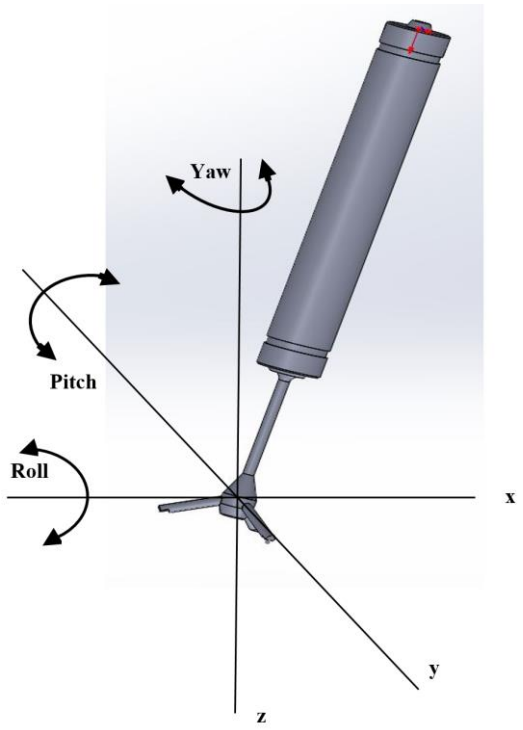

Figure 2-5: ADV rotation

The ADV carries an Inertial Measurement Unit (IMU) that enables the ADV to measure acceleration in three directions. The stationary ADV only measures gravitational acceleration; therefore, the pitch angle of the ADV during measurements in the channel can be obtained from:

$$\emptyset = acos\left(\frac{A_{cc}}{g}\right) \quad \textbf{(2-1)}$$

were A_{cc} is the vertical component of the acceleration measured by IMU and g is the gravity. The corrected vertical velocity for the flow coordinate system, $W_{corrected}$, is obtained from:

$$W_{corrected} = U_{raw} * sin(\emptyset) - W_{raw} * \cos(\emptyset) \quad \textbf{(2-2)}$$

were U_{raw} and W_{raw} are velocities measured by ADV in X and Z directions of the body coordinate system respectively. The first transformation of the streamwise velocity, U_{T1}, from raw X-direction velocity of the ADV, U_{raw}, is obtained from:

$$U_{T1} = U_{raw} * cos(\emptyset) + W_{raw} * \sin(\emptyset). \quad \textbf{(2-3)}$$

The yaw angle of the ADV is obtained from the first transformation of the streamwise velocity and the raw Y-direction velocity of the ADV, V_{raw}, from:

$$\theta = \text{atan}\left(\frac{V_{raw}}{U_{T1}}\right) \quad \textbf{(2-4)}$$

The corrected streamwise velocity, $U_{corrected}$, and transvers velocity, $V_{corrected}$, are obtained from:

$$U_{corrected} = U_{T1} * \cos(\theta) + V_{raw} * \sin(\theta) \quad \textbf{(2-5)}$$

$$V_{corrected} = V_{raw} * \cos(\theta) - U_{T1} * \sin(\theta) \quad \textbf{(2-6)}$$

A set of experiments were conducted in a water tunnel to validate the analytical formulas developed in the previous section for pitch and yaw angle corrections. Tests were conducted in the University of Manitoba's water tunnel with the test section width of 61 cm, length of 183 cm and depth of 60 cm. A costo-made mount holds the ADV in the water tunnel such that ADV sampling volume is positioned at the center of the test section away from water tunnel walls and boundary layers. The mount provides four degrees of freedom: vertical and lateral motions, in addition to pitch and yaw angles.

Figure 2.6 shows the time averaged streamwise, transverse and vertical velocities before and after the correction. The base lines to validate the results are values for three velocity components at zero yaw and pitch angles. Results indicate accurate performance of the analytical method for all three velocity components in general and for the streamwise velocity in particular. The deviation in the vertical and transverse velocity corrections is the result of the near zero velocity components in these two directions; therefore, any small error has a magnified effect in the final result.

Figure 2.7 shows comparison between the geometric and calculated angles in the pitch and yaw directions. The geometric angles are set on the mount holding the ADV in the water tunnel and are known for each test and are used as benchmarks to evaluate the accuracy of the analytical model. It can be seen that the maximum difference between geometric and calculated yaw ∅ is less than 4%, since this difference is between 1.8 and 14 % for the pitch angle θ. One of the reasons that the error in the pitch angle calculation is higher than the error in the yaw angle is that the yaw angle is calculated directly from IMU acceleration, while the pitch angle is obtained from the transverse velocity which is a small number.

(a)

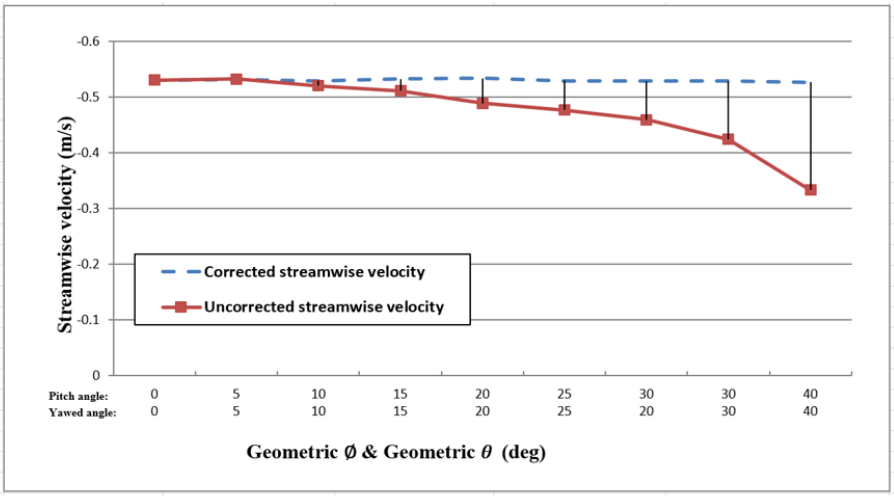

(b)

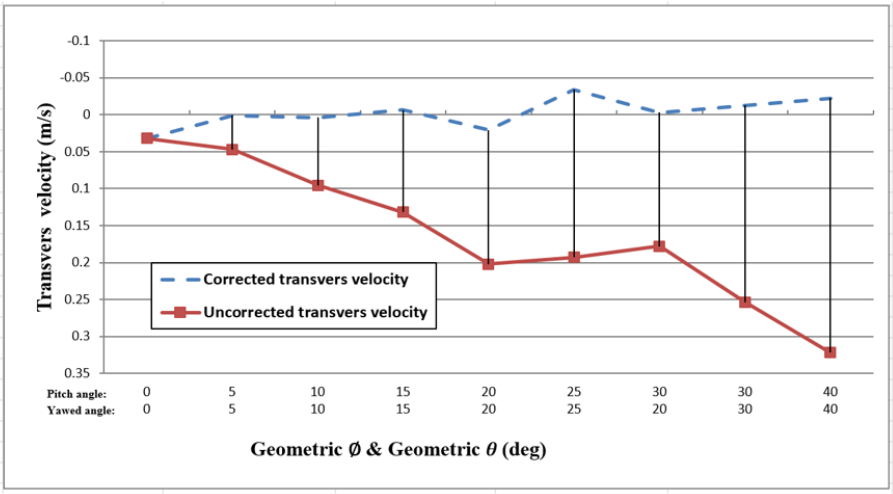

(c)

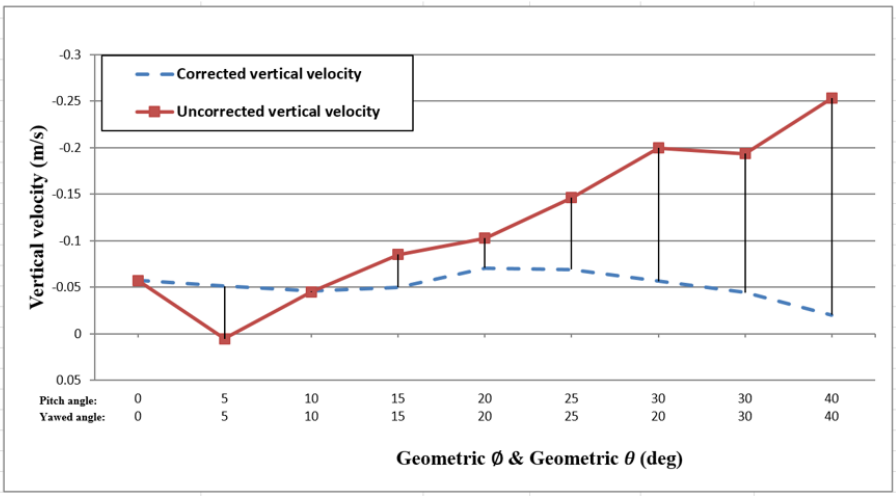

Figure 2-6: Time averaging of the velocity components before and after transformation (a) streamwise velocity, (b) transvers velocity, (c) vertical velocity

(a)

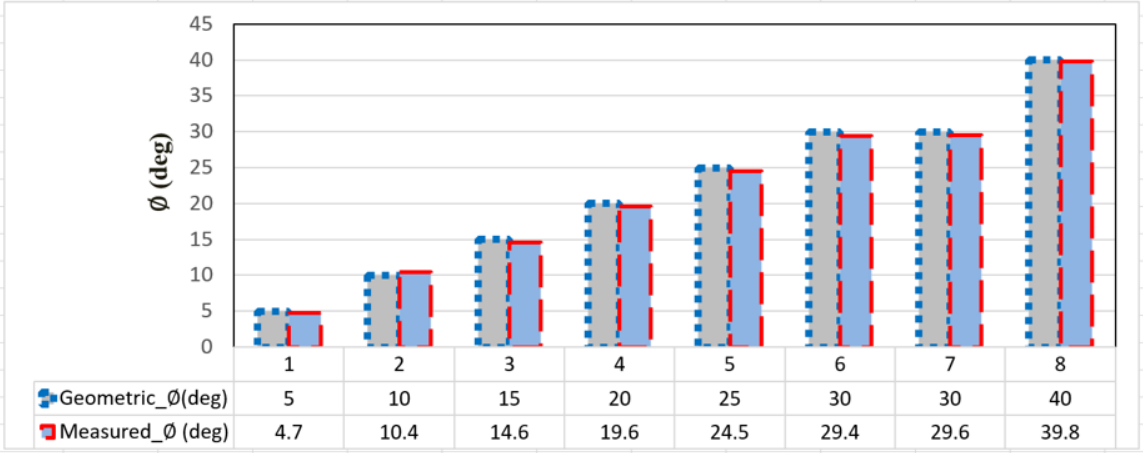

(b)

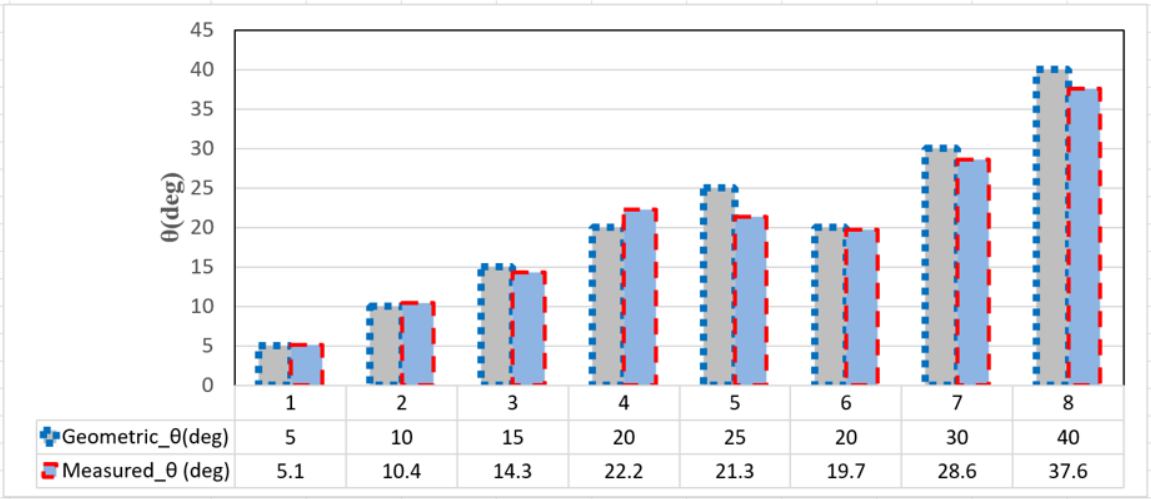

Figure 2-7: Comparison between geometric angles and calculated angles using IMU and Velocity data (ADV), (a) (Ø), (b) (θ)

2.7 Data analysis

The data was collected at three locations, location 1, location 2, and location 3, as shown in Figure 2.1. The flow velocity was recorded at these three locations at 1 m depth increments from the free-surface using 7 minute ADV recording periods. The collected data is despiked before further analysis as outlined earlier.

2.7.1 Velocity component characterization

In order to visualize how the velocity is distributed around the mean velocity, the probability distribution of the streamwise velocity at a depth of 1.3 m below the surface is plotted in Figure 2.8. The distribution is evidently normally distributed, typical of turbulent flows.

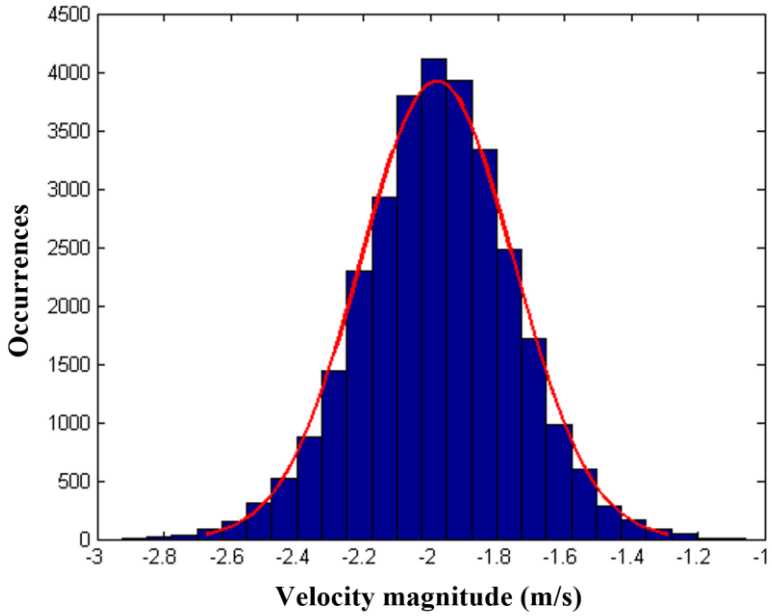

Figure 2-8: Streamwise velocity histogram

The profiles of the instantaneous velocity components at a depth of around 1.3 m are shown in Figure 2.9. Evidently the streamwise velocity is bounded between 1.15 and 3.5 m/s. The upward and transverse velocities in the river are the results of the large eddies and boils in the turbulent flow. The variation of the upward velocity is noticed to be somewhat similar to the variation of the streamwise velocity. This may be because the orientation of the sampling volume with respect to the flow direction, leading to components of the true streamwise velocity being resolved in the upward direction. The time-averaged streamwise velocity is 2.39 m/s, while the transverse and upward velocities are almost 0 and 0.001 m/s respectively. These values give a basic understanding of the nature of the flow.

(a)

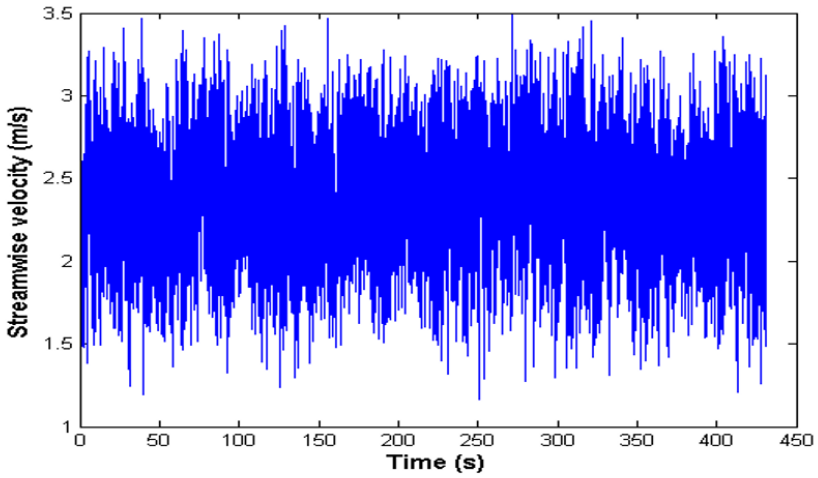

(b)

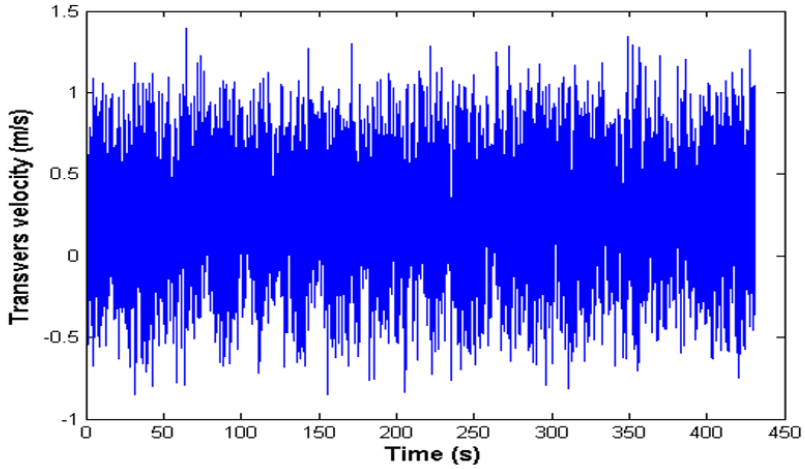

(c)

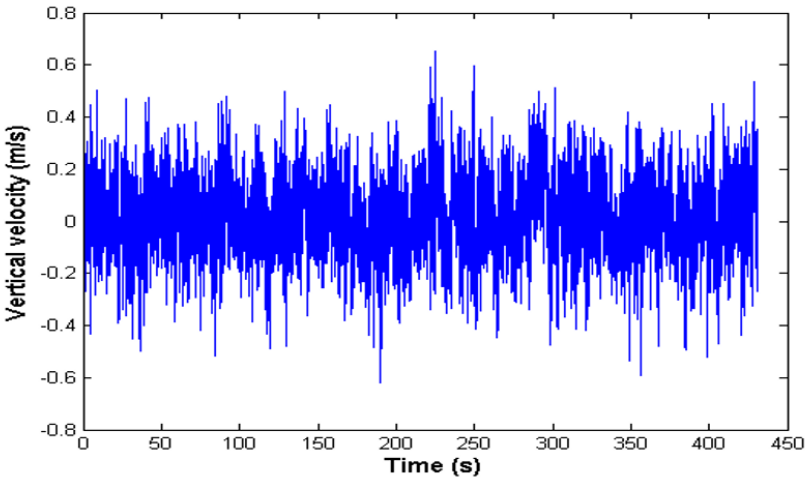

Figure 2-9: Orthogonal velocity components at 1.3m depth (a) streamwise velocity, (b) transvers velocity, and (c) vertical velocity

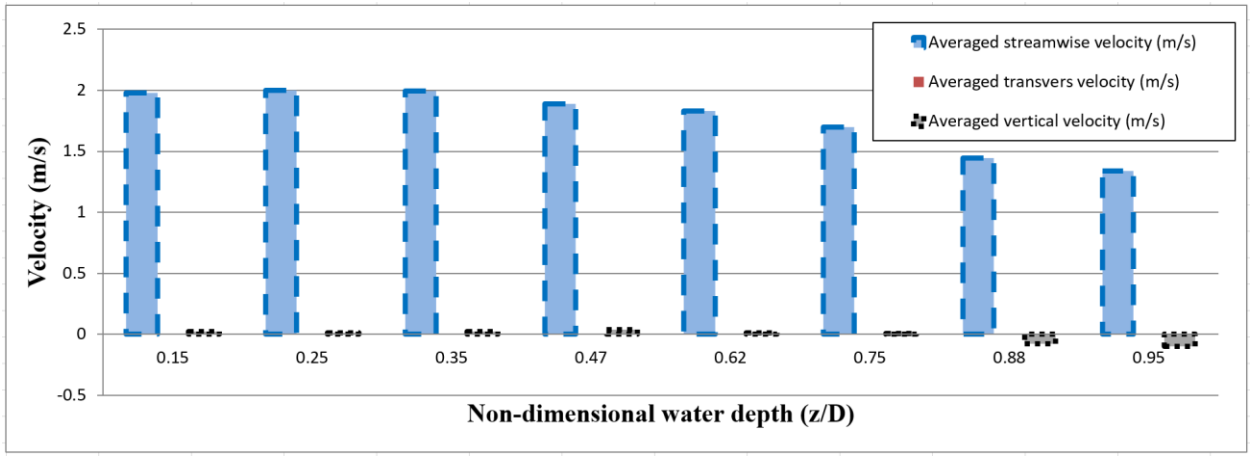

Figure 2-10: Comparison between velocity components

Comparing between the time averaged velocity components, the transverse and vertical velocities are much smaller magnitude than the streamwise velocity, and are less than 1% of the streamwise velocity as can be seen in Figure 2.10. According to the analytical conversion method developed and verified through water tunnel tests, the pitch and yaw angles of the ADV during field measurements are obtained using $\emptyset = acos\left(\frac{A_{cc}}{g}\right)$ and $\theta = \text{atan}(\frac{V_{raw}}{U_1})$. The adjusted streamwise and spanwise components of velocity are used to determine the dominant flow direction/angle, shown in Figure 2.11. It should be noted that the flow direction is based on the local frame coordinate system. The variation of pitch angle with respect to depth was also calculated and is shown in Figure 2.11.

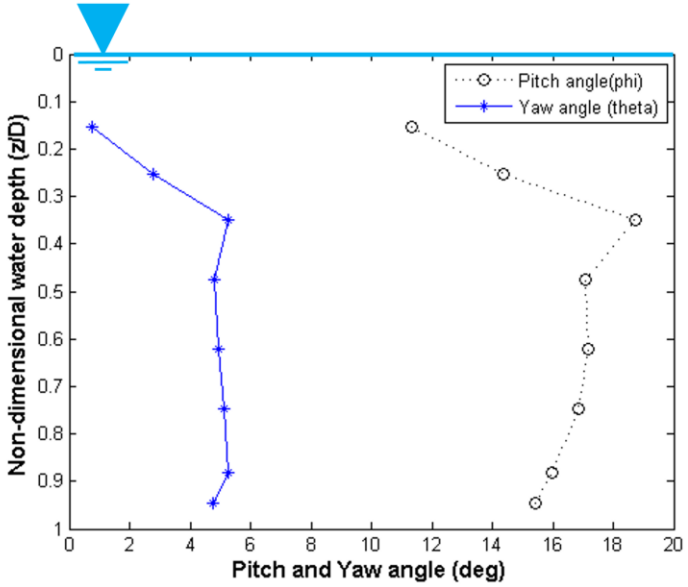

Figure 2-11: The dominant flow direction and the pitch angle of the ADV varying with the depth

2.7.2 Velocity variation with depth

The river has a depth of 8.5 m. As can be seen from Figure 2.12, streamwise velocity has a maximum value at point z/D= 0.3 and then it decreases with depth. It reduced by 31.6 % near the river bed at z/D = 0.94. It can be seen that the velocity components decrease gradually in a layer close the river bed. The thickness of this layer is about z/D = 0.3, where we can see a large velocity deficit; this region will be referred to as the boundary layer region. This layer seems to be just above the boundary layer. In the boundary layer the turbulence is governed by the roughness of the river bed. Quantifying the boundary layer in the marine environment is a critical necessity, where it dominates the performance of marine engineering systems [Clark et., al. (2015)].

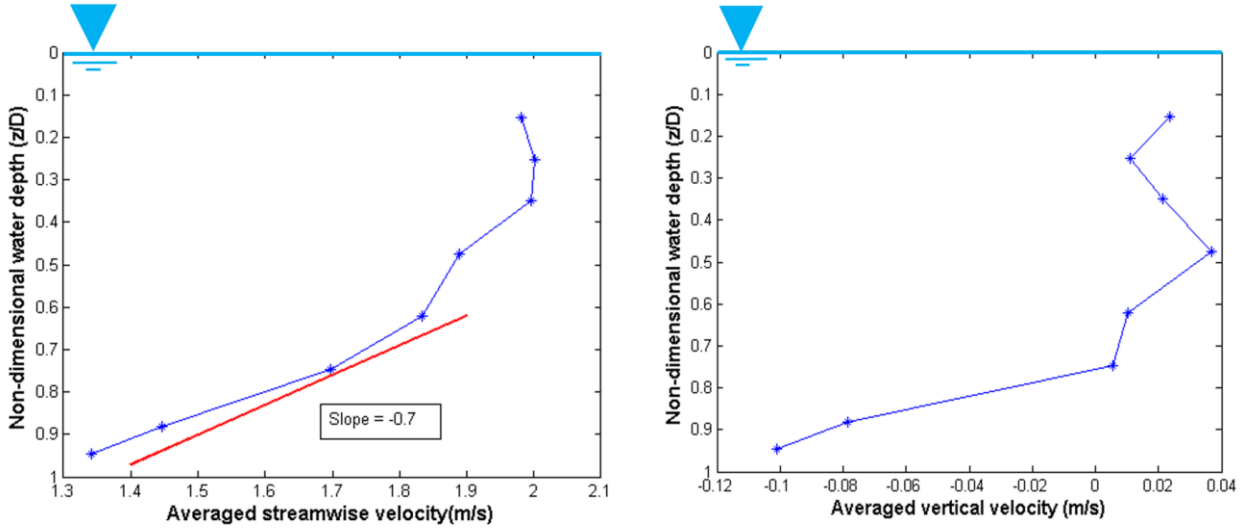

(a) (b)

Figure 2-12: (a) Streamwise mean profile with respect to river depth, (b) Upward mean profile with respect to depth

Thus, marine turbines are invariably placed away from the bed to avoid the boundary layer. Usually, the river has a variation in bed friction and channel geometry along the streamwise direction, resulted in a nonequilibrium boundary layer. Vertical velocity has its higher values at the boundary layer region as can be seen in the Figure. Its maximum magnitude is shown to be increased gradually in the boundary layer region by approximately 0.09 ms^{-1}, but there appears to be little variability between the boundary layer region and the free surface. The negative velocity might be due to vertical eddies in the flow.

2.7.3 Reynolds stresses

The total stress tensor in a turbulent flow is obtained from the averaging operation over the Navier-Stokes equations. The stress tensor comprises Reynolds stress terms but, since it is symmetric ($\overline{uv} = \overline{vu}$), only six components are independent. Three are tangential stress terms $\overline{uv}$, $\overline{uw}$, and $\overline{vw}$ and three normal stress terms $\overline{uu}$, $\overline{vv}$, and $\overline{ww}$. Generally, the tangential stress terms are known as momentum flux terms. Physically, they represent momentum flux due to turbulent fluctuations. When the normal stress terms are not equal, the turbulence is non-isotropic and there is a shear stress. Non-isotropic turbulence leads to the transport of momentum usually orders of magnitude greater than that of molecular action. For instance, uw is defined as the turbulent vertical advection of streamwise turbulent momentum, or more simply the vertical flux of streamwise momentum.

The Reynolds stress terms might be greater or smaller than zero. The sign (positive and negative) tells whether the flux is inducing a net increase or decrease in momentum, respectively. The instantaneous velocity can be decomposed into mean values and fluctuations U=$\overline{U}$+u. The time averaging velocities have been calculated. The fluctuations were also determined in order to find the Reynolds Stresses by using the following formulas:

$$\overline{uu} = \overline{(U-\bar{U})(U-\bar{U})}$$

$$\overline{vv} = \overline{(V-\bar{V})(V-\bar{V})}$$

$$\overline{ww} = \overline{(W-W)(W-\bar{W})}$$

$$\overline{uv} = \overline{(U-\bar{U})(V-\bar{V})}$$

$$\overline{uw} = \overline{(U-\bar{U})(W-\bar{W})}$$

$$\overline{vw} = \overline{(V-\bar{V})(W-W)}$$

$$R=\begin{bmatrix} 0.0863 & 0.0011 & 0.0132 \\ 0.0011 & 0.0757 & 0.0006 \\ 0.0132 & 0.0006 & 0.0173 \end{bmatrix}$$

2.7.4 Turbulence intensity

The 3D turbulence intensity is defined to relate $u' = \sqrt{\frac{1}{3}(\bar{u}^2 + \bar{v}^2 + \bar{w}^2)}$, the streamwise, transverse and upward velocity fluctuation components (u, v, w) to the magnitude of the flow velocity U = $\sqrt{(\bar{U}^2 + \bar{V}^2 + \bar{W}^2)}$; $TI = {}^{\sigma}/_{U}$. Generally, the ambient turbulence intensity critically affects the performance of hydrokinetic turbines. The wake shape behind turbines is also deeply influenced by the turbulent intensity, decaying much faster with a higher upstream turbulence intensity [MacLeod, et al., (2002); Mycek, et al., (2014)] with commensurate implications for turbine arrays. In several sites where marine current turbines are installed, several studies have been conducted to characterize the turbulence intensity [Osalusi, et al., (2009); Colby, et al.,

(2010); Thomson, et al., (2012); Milne, et al., (2013); Mycek, et al., (2014)]. Osalusi, et al., (2009) conducted a study at the tidal test site of the European Marine Energy Centre (EMEC) (Scotland, UK); they found that the turbulent intensity at 5 m above the seabed ranging between around 8% to 8.7% for a mean velocity of 1.5 m/s. Colby, et al., 2010 carried out a study in the East River (New York, NY) and found that the 3D turbulent intensity is approximately 16−24%. Thomson, et al., 2012 measured the streamwise turbulence intensity at 8.4% using an ADV at 4.7 m from the seabed in the Puget Sound, US. At nearly the same height from the seabed in the Sound of Islay, UK, for a mean velocity of 2 m/s, Milne et al., reported that the turbulent intensity is roughly 9.5% to 10.5%. Mycek, et al., (2014) reported that the ambient turbulence intensity influences the machine behavior in terms of force and torque fluctuations, however it dose not have strong influence on the power and thrust coefficients of hydrokinetic turbines.

In the present study, the 3D turbulence intensity was found to vary between a minimum of 9.1% at the free surface to a maximum of 17.6 % in the boundary layer, as can be seen in Figure 2.13. By looking at the Figure, one can notice that the intensity is increased with depth untill it reaches its maximum value, which is increased by 83.5 percent, at the boundary layer region. This is because the mean flow velocity magnitude is decreased in this layer as shown in the Figure, while the streamwise, transverse and upward velocity fluctuation components are increased. In this layer, the change in TI and flow velocity have a slope of 0.05 and -0.7 respectively.

(a)

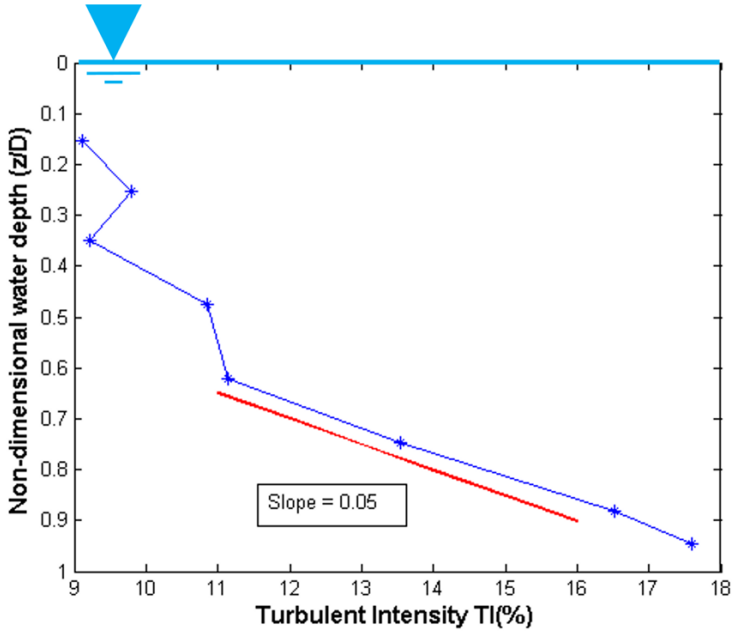

(b)

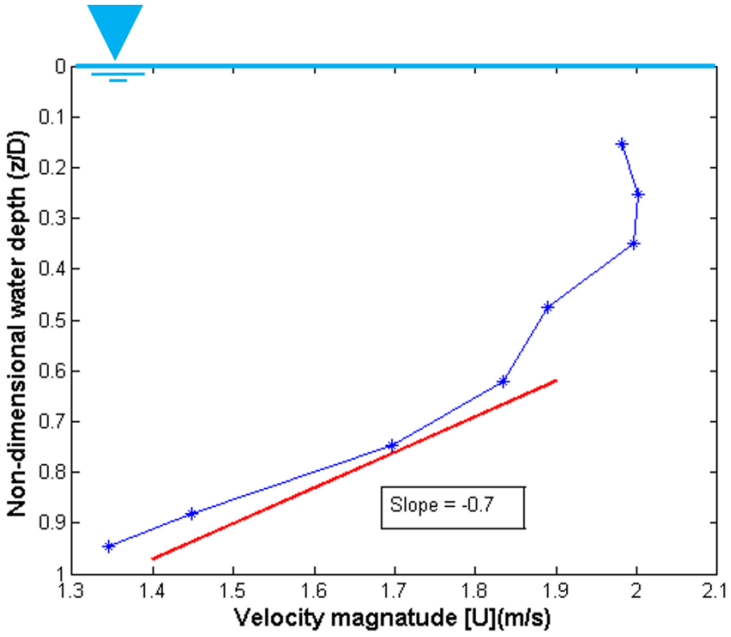

Figure 2-13: (a) 3D turbulence intensity and (b) velocity magnitude profile with respect to depth

The evaluation of the turbulence intensity of the three components of velocity with depth is shown in Figure 2.14. From the Figure, the turbulent intensities of the components of velocity have similar behavior to turbulence intensity of the flow velocity. The spanwise intensity increases with depth reaching values up to 59% at the boundary layer region. The spanwise and vertical velocities have smaller turbulent intensity. By examining the figure, the spanwise turbulence intensity has close

behavior to the streamwise velocity, and is about twice as great than the vertical intensity. The vertical component's turbulence intensity increases slightly with respect to position; it varies between 0.34% and 1.97%.

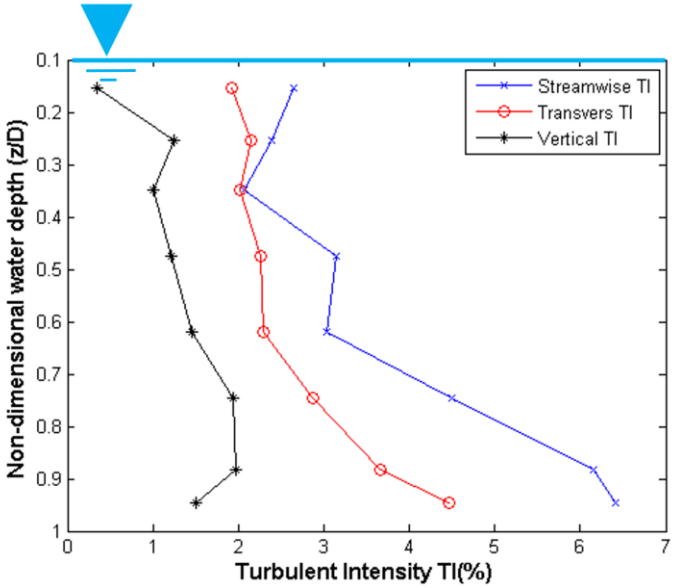

Figure 2-14: The turbulent intensity components

2.7.5 Turbulent kinetic energy

The turbulent kinetic energy per unit mass k is characterized by measured Root-Mean-Square (RMS) velocity fluctuations to be as K= $\frac{1}{2}(\bar{u}^2 + \bar{v}^2 + \bar{w}^2)$. The TKE production represents the energy being transferred from the mean flow to the turbulent kinetic energy. This production is estimated from the product of the Reynolds Stress and the velocity shear. The TKE is dissipated into heat via the effect of fluid viscosity, with a rate referred to as the dissipation rate.

The variation of TKE with depth is shown in Figure 2.15. As can be seen in the Figure, the turbulent kinetic energy has maximum value of 0.086 J/kg in the boundary layer region, due to increases in the velocity fluctuations in this layer, and the fact that the shear is higher near the boundary layer. On the other hand, the turbulent kinetic energy is decreased by roughly 44 % at 0.15z/D below the free surface to be just 0.048 J/kg.

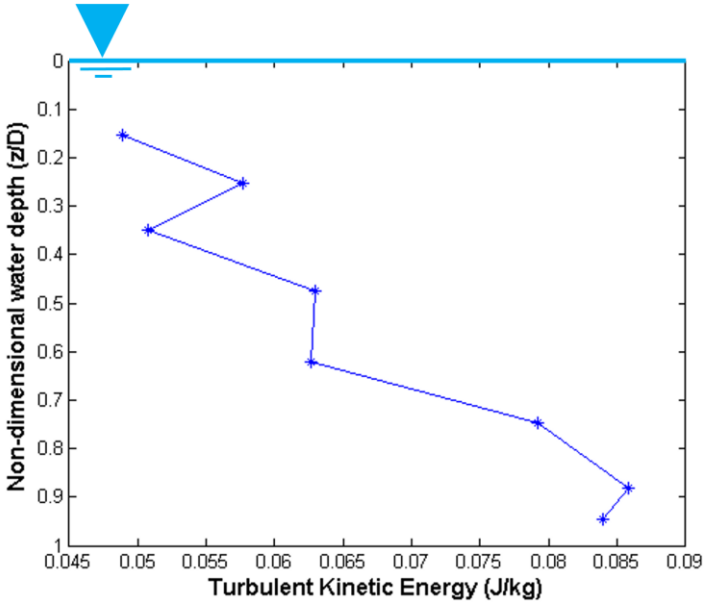

Figure 2-15: Variation of TKE with the depth

2.7.6 Flow length scales and power spectrum

To calculate the integral length scale, one needs to compute the autocorrelation coefficient. The autocorrelation between the values of a fluctuation of the streamwise velocity at a fixed point in the flow at two different instants t and t+τ can be written as $R_{uu} = \overline{u_1(t)u_1(\mathrm{t}+\tau)}$. The autocorrelation coefficient is defined as $\rho_{uu} = \frac{\overline{u_1(t)u_1(\mathrm{t}+\tau)}}{\langle u_1^2 \rangle}$, where u is the fluctuating streamwise velocity component. The autocorrelation function for the three components of velocity at two points, (a) near the free surface and (b) in the boundary layer, can be seen in Figure 2.16.

The integral time scale is a measure of how long turbulent fluctuations remain correlated. The integral time scales are computed by integrating the autocorrelation function from t=0 to the first instance of ρ_{ii}=0 (zero crossing) as $T_i = \int_{t=0}^{t(\rho_{ii}(t)=0)} \rho_{ii}(t)dt$. At depth of around 0.15z/D from the free surface the integral time scales for the three velocity components are measured to be T_u=2.9 s, T_V= 1.12 s and T_w= 3.1 s. At the boundary layer region, at a depth of 0.97z/D, they are found to be T_u=4.5 s, T_V= 0.42 s and T_w= 1.21 s respectively. The differences are representative of eddy sizes, and the changes in the eddy structures with depth. Near the surface, the eddies are evidently vertically orientated, while in the boundary layer region are more elongated vertical structures

owing to the presence of the bottom. The short horizontal time scales indicated relatively little mixing laterally.

(a)

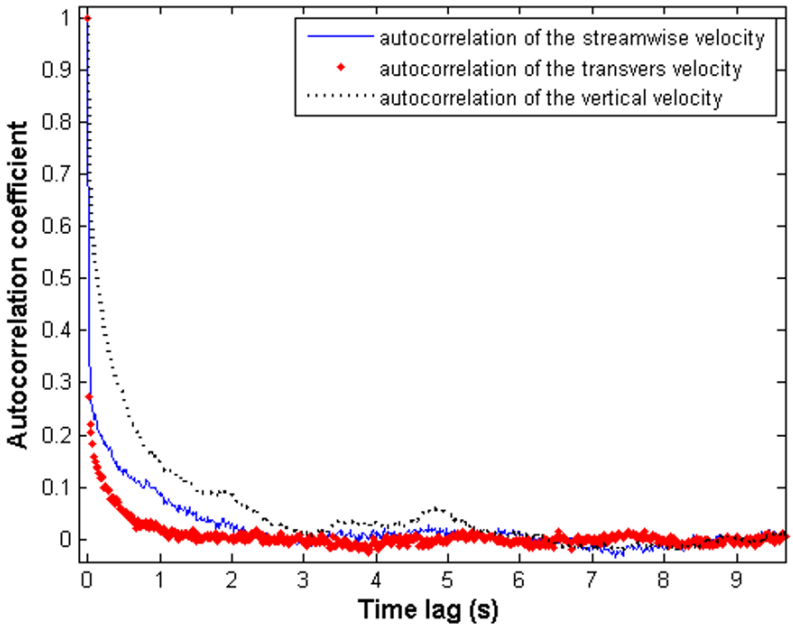

(b)

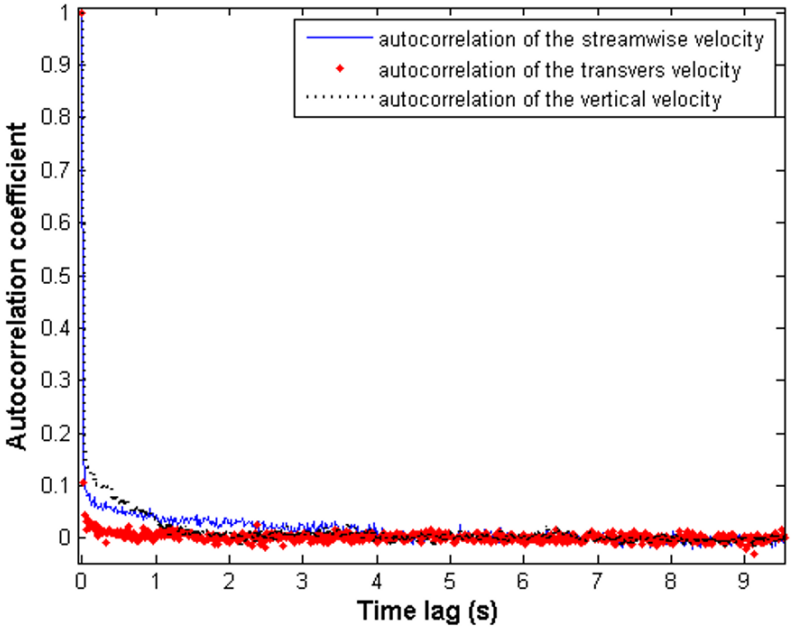

Figure 2-16: The autocorrelation function for the three components of velocity, (a) At 1.3 m below the free surface, (b) at depth of 8.24 m

The integral length scale represents a measure of the longest connection (or correlation distance) between velocities at a single fixed point but at different times. To compute the integral length

scale, assuming Taylor's frozen turbulence hypothesis to be valid, the integral time scale has to be multiplied by the mean velocity. Hence, the integral length scale of the velocity components, streamwise, spanwise and vertical at 1.3m below the free surface are found to be around 6.93m, 0.278m and 0.046m respectively; in the boundary layer region they are 8.97m, 0.184m and 0.114m respectively.

The use of a fin for ADV stabilization resulted in good raw data that were consistent with the expected turbulence spectra. The power spectral density (velocity variance as a function of frequency) of the streamwise velocity at a depth of 0.15z/D and 0.97z/D were calculated from the ADV data in FFTs and are shown in Figure 2.17. As can be observed from the Figure, the inertial sub-range portion of the spectra has a slope of -5/3 for a depth of 0.15z/D; the Figure shows acceptable a slope (i.e. consistent with Kolmogorov rate in inertial subrange) for a depth of 0.97z/D. It can be also noticed that because of the noise in the ADV measurements, the spectra tend to become horizontal at high frequency beyond 10 Hz. At depth, there is more energy generally in the turbulent flow, owing the presence of the bottom and generated turbulent boundary layer.

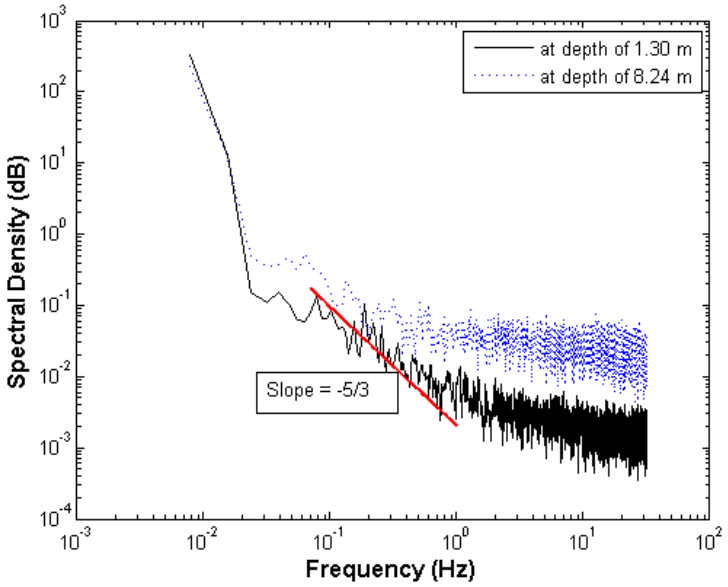

Figure 2-17: Spectrum of the streamwise velocity at 1.3 m below the free surface (black solid line), and at depth of 8.24 (dot blue line)

2.8 Conclusion

The aim of this study was to characterize turbulent flow through the water column in the Winnipeg river, where the flow velocity is roughly 1.9-2.3 ms^{-1}. The ADV was capable of providing data at high temporal resolution and it is a well-suited metrology for measuring field data in rivers. The flow velocity has its maximum magnitude at approximately 3m below the free surface; it reduced by about 32% at 2m above the riverbed. In the bottom boundary layer turbulence intensity of the flow velocity increases gradually while the velocity magnitude decreases gradually. In this layer the TI is nearly twice its value near the free surface. The behavior of the turbulence intensity in the streamwise and transverse directions is similar. The spanwise and upward integral length scales were much smaller magnitude than the streamwise integral length scale, however there is variation in the vertical length scales with depth, indicated reduced eddy size vertical extent with depth as the bottom is approached. The streamwise energy spectrum results showed that flow is a fully developed turbulent flow with a -5/3 slope of the inertial sub-range portion of spectra. The use of a fin for stabilization resulted in raw data that were consistent with expected turbulent decay characteristics. The obtained results will be helpful for the hydrokinetic turbine industry as well as improving laboratory and CFD models.

Chapter 3

3 An experimental study of fractal grid generated-turbulence using PIV

Authors: Altayeb Mahfouth[1], Curran Crawford[1]

[1] Dept. of Mechanical Engineering, University of Victoria, BC

To be submitted

3.1 Abstract

In this work, the turbulence properties of fractal grids were experimentally investigated by means of 2D Particle Image Velocimetry (PIV). This work was motivated by the need to determine power coefficients for wind/tidal turbine rotor in controlled turbulent flow conditions, to compare to results typically obtained in very low turbulent tunnels which are not representative of real-world conditions. Multiscale grids have been designed guided by the results found in the existing literature to achieve a desired turbulent profile. Square pattern fractal grids were used in this study. The fractal grids were installed at the entrance of a water channel, with a test section area of T=0.45m2 cross section and 2.5m length. The experiments were run at different inlet velocities, 0.9 m$s^{-1}$for grid N4 and 1.3 and 1.5 m$s^{-1}$for grid N3 respectively. The background turbulence intensity of the flow in the tunnel in the absence of the fractal grid obstruction is 0.5 % in the streamwise direction. The average and fluctuating flow fields are presented and the streamwise turbulence intensity along the channel is analyzed. The position and magnitude of the peak turbulence intensity is compared with predictions from sizing rules reported in the literature and relative the future positions of test rotors in the water tunnel.

Key Words: Fractal square grid; Turbulence Measurement; Particle Image Velocimetry (PIV); Wind/Hydrokinetic turbine rotor.

3.2 Introduction

It is well-known that wind and tidal turbines always operate in the field in turbulent conditions which influence their performance tremendously, but wind and flume tunnel lab testing is typically done in very low turbulence conditions [Batten, et al., (2007), Burton, et al., (2011)]. Some studies have simply removed flow straighteners in the water tunnel to create turbulence in the water tunnel test section, but introduce more complicated overall flow patterns confounding interpretation of the results [Mycek, et al., (2014)]. Regular, fractal, and active grids have all been used to generate more controlled turbulence in water and wind tunnels [Queiros & Vassilicos, (2001); Hurst and Vassilicos, (2007); Seoud and Vassilicos, (2007); Mazellier and Vassilicos, (2010); Stresing, et al., (2010); Discetti, et al., (2011); Laizet and Vassilicos, (2011); Valente and Vassilicos, (2011a,b); Cardesa and Nickels, (2012); Gomes, et al., (2012); Stefan, et al., (2013); and Hearst, (2015)]. Regular and fractal grids are rigid structures with constant solidity that result in turbulent flows with specific patterns and statistics corresponding to the grid geometry. Fractal grids in particular are able to generate controllable turbulence build-up and decay rates, with high turbulence intensity (TI).

The turbulence intensity is the ratio of the root-mean-square of the turbulent velocity fluctuations to the magnitude of the flow velocity ($TI = \frac{\sigma_u}{\bar{u}}$); is often referred to as turbulence level. It helps to understand the nature of turbulence in the turbulence flow such as rivers for which is considered as a main aspect in terms of designing hydrokinetic turbines. Typically, three cases of turbulence were introduced based on the turbulent intensity level [Soltani, et al., (2011); Ghorbanian, et al., (2011); Strom and Papanicolaou, (2007); Balcer, (2005); George, et al., (1994); Nikora and Smart, (1997)]. A low-turbulence case occurring at controlled lab facilities and has turbulence intensity lower than 1% [Soltani, et al., (2011), Ghorbanian, et al., (2011)]. Turbulence intensity with range between 1%-5% is considered a medium-turbulence case; this occur in deep-wide rivers or low velocity shallow rivers and downstream of the turbulence generating regular grids [Strom and Papanicolaou, (2007); Balcer, (2005)]. 5%-20% is a high-turbulence case; like fast current rivers [George, et al., (1994); Nikora and Smart, (1997)].

Downstream of regular grids, the turbulence is created on a relatively uniform scale and breaks down through an energy cascade. In contrast, the fractal grids generate turbulence by creating different sizes of vortices with corresponding levels of interaction. The main interaction events occur when similar sized wakes meet and since the bars in a fractal grid have different sizes and are placed at different distances from each other, the turbulence is generated from a range of wakes interacting at different locations downstream [Mazellier and Vassilicos, (2010); Laizet and Vassilicos, (2011)]. The smallest wakes meet and mix together at locations closer to the grid than the larger wakes. Various patterns for fractal grids can be characterized as: I pattern, cross pattern and square pattern. The last pattern is the one used as a basis for the current.

A schematic of a square type fractal grid is shown in Figure 3.1. Space-filling fractal square grids with relatively low solidity have the ability to generate turbulence with high Reynolds numbers compared with turbulence generated by regular grids at the same flow speed [Seoud and Vassilicos, (2007)]. Note that for this discussion, the appropriate Reynolds number is $Re_\lambda = \frac{u'\lambda}{v}$, where $u'$is the instantaneous fluctuating velocity, λ is the Taylor microscale[9], and v is the kinematic viscosity of the fluid. This is also confirmed by [Mazellier and Vassilicos, (2010)] who found that compared with higher blockage regular grids, much higher turbulence intensities and Reynolds numbers can be produced by fractal grids. Active grids are another alternative that use moving elements to generate specific turbulence characteristics as well, but require much more complex moving mechanisms. Active grids allow more flexible generation of turbulent flow by actively changed the orientation of the grid structure [Stefan, et al., 2013]. Generating turbulent flow with special characteristics require a better understanding of these multi-scale/fractal generation of turbulence. Fractal grids are therefore the focus of the work presented in this paper, due to their simplicity relative to active grids, but controlled turbulence generation relative to regular grids.

[9] Also, called the turbulence length scale and defining the intermediate length scale between large-scale eddy size range where inertia dominates and the small dissipation range where viscosity dominates.

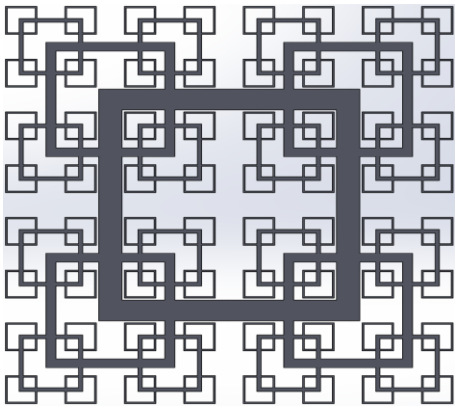

Figure 3-1: A schematic of a square type fractal grid

A number of previous experiments have been done with the goal of creating controllable turbulence using fractal grids. Some of these experiments have been aimed at studying the properties of the turbulent flow behind the grid and how it change by varying the grid's parameters [Queiros & Vassilicos, (2001); Staicu, et al., (2003); Hurst and Vassilicos, (2007); Seoud and Vassilicos, (2007); Mazellier and Vassilicos, (2010); Stresing, et al., (2010); Discetti, et al., (2011); Laizet and Vassilicos, (2011); Valente and Vassilicos, (2011a,b); Cardesa and Nickels, (2012); Gomes, et al., (2012); Stefan, et al., (2013); and Hearst, (2015)]. Fractal square grids have received much more attention than the I and cross grids because of the fact that they give the most interesting turbulent statistics results among other grids, whereas, they give production region between the grid and the x_{peak} with fast build-up turbulence rate, high Reynolds number, high turbulence intensity with the same blockage ration, lower static pressure drop across the grid [Hurst & Vassilicos, (2007); Mazellier & Vassilicos, (2010)]. Turbulence generated by 3D fractal elements was first reported by Queiros-Conde & Vassilicos, (2001) and Staicu, et al., (2003). They studied the turbulence statistics in the wake of 3D fractal grids. They reported that these grids can generate turbulence with very long production region compared with higher blockage regular grids which generate turbulence just within the decay region. This makes it not suitable for the motivation of this work and it is excluded because this production region has inhomogeneous and anisotropic turbulence.

A total of 21 planar fractal grids from 3 different patterns have been tested by Hurst &Vassilicos, (2007): fractal cross grids, fractal I grids and fractal square grids. For the space-filling fractal square grids, they found that the distance downstream where the turbulence peak position occurs

seems to be controlled by the smallest length scales on the fractal square grid $x_{peak} = 75\frac{t_{min}T}{L_{min}}$. The turbulence decays exponentially after the turbulence intensity peak position. Specific parameters of the fractal grid such as the fractal dimension (D_f), the number of fractal iteration (N) and the thickness ratio (t_r) can control this turbulence decay. They also mentioned that increasing the thickness ratio (t_r) by reducing the thickness of the smallest element in the fractal square grids ($t_{\min}$) can lead to increased turbulence intensity and Reynolds numbers. The position of the peak Reynolds number moves closer to the grid when increasing t_r. Mazellier & Vassilicos, (2010) and Laizet & Vassilicos, (2011) defined two regions, one close to the fractal square grid, the other further downstream. The turbulence in the near region is anisotropic and non-Gaussian, while that in the downstream region is isotropic and Gaussian. It is interesting to note that [Seoud & Vassilicos, (2007)] concluded that the ratio between the Taylor microscale and the integral length scale remains constant where the turbulence is approximately isotropic in a large region further downstream of the fractal square grids. However, [Mazellier & Vassilicos, (2010), Valente & Vassilicos, (2011a)] discussed that Taylor microscale is not exactly constant in the wakes of fractal grids and this can reflect the fact that turbulence decay is not really exponential, but a fast power law which can be fitted quite closely by an exponential for some distance downstream. This makes sense, based on Kolmogorov thought which implies that the turbulence energy needs different length scales to cascade down till it dissipates at length scale small enough for the dissipation to occur at higher Reynolds number. Unlike regular generated turbulence, that decays as a power law, fractal square generated turbulence decays exponentially far enough downstream where the flow is homogeneous and isotropic [Strsing, et al., (2010)]. The wake-interaction length scale x_* was first introduced by Mazellier & Vassilicos, (2010). Estimates x_*^{peak} were improved by Gomes, et al., (2012) by taking into account the free-stream turbulence characteristics and the geometry of the grid to enable the comparison of the data from different experiments.

Gomes, et al., (2012) conducted PIV study of fractal-generated turbulence, reporting on an investigation of the flow in the lee of space filling square fractal grids in a water tunnel using planar PIV. They found good agreement between their results and Mazellier & Vassilicos, (2010)' results in terms of turbulence intensities, Taylor microscale, and other quantities, when the improved wake-interaction length scale is used.

Stefan, (2011) investigated the influence of different boundary conditions, bar sizes and solidity of fractal grids on generated flow. He reported that the properties of the fractal generated turbulence depend on the smallest and largest scales in the grid, as well additional grid parameters. A slight change in the position of the peak turbulence intensity (x_{peak}) was noticed when increasing the thickness ratio of the grid's bars. Designing the grid's walls to permit a free flow around the edges of grid area had no effect on the statistical properties (such as mean velocity, turbulence intensity and flatness) of the flow along the centerline. On the other hand, blocking parts of the grid caused a strong influence on the flow. The shape of the spectrum of the flow close to the grid depends mostly on the small scales [Stefen, et al., (2013)]. Mazellier & Vassilicos mentioned that for values of t_r equal to and bigger than 8.5 the wakes from the biggest bars eliminate that from the smallest ones. Furthermore, Hurst & Vassilicos, (2007) concluded that smaller values of t_r the thickness of the smallest squares becomes non-negligible and their wakes influence the location of the turbulence intensity peak, as well as the turbulence intensity at that location. Hearst, (2015) investigated the turbulent motion of the flow behind three passive grids and an active grid in a wind tunnel.

A range of materials and manufacturing methods have been used to construct fractal grids. Hurst & Vassilicos, (2007) have used acrylic and wood (with a constant thickness of 5mm in the direction of the flow). They also used steel (constant thickness of 1.6 mm in the direction of the flow) for some experiments. Cardesa and Nickels, (2012) used stainless steel for their regular grids, covered with a black spray paint to avoid laser light reflections. Gomes, et al., (2012) conducted an experiment in water with three different experimental cases, three different inlet speed U∞ = 0.48, 0.59 and 0.69 m/s; using acrylic grids with 5 mm thickness.

Here we present water tunnel measurements of turbulence generated by fractal square grids placed at the entrance of a water tunnel test section. The aim of this work is to design a square fractal grid that can generate turbulence with specific properties representative of tidal/river flows characteristics in the water tunnel, at specific location downstream in the channel, for testing the performance of various tidal/kinetic turbine devices. The paper is structured as follows. Section 3.2 describes the experimental apparatus including experimental facility and optimized parameters of the fractal grid. In section 3.3, the experimental technique used in this work is introduced. The results from water tunnel testing of the grids are reported in section 3.4. A conclusion summarizing

and comparing the results obtained from different fractal square grids and against prediction rules drawn from literature is given at the end.

3.3 Experimental apparatus

3.3.1 Experimental facility

Experiments were conducted in the water tunnel of University of Victoria. It is a recirculating water tunnel with test section of 0.45 m^2 cross section and 2.5 m long. The water tunnel can operate at any water height up to 0.45m. The channel is provided with two acrylic lids to slightly pressurize the flow, which can prevent any waves formation at the surface. The experiments were conducted in the channel with the lids installed. The walls of the channel are transparent, which allow optical access through the sides and the bottom so that the flow can be observed. In this study, all measurements were taking with optical access through the bottom. A single stage axial flow propeller pump drives the flow in the water tunnel. The pump delivers a maximum flow rate of 405L/s with a maximum test section velocity of 2 m/s. A 25 HP, 1180rpm, 3 ∅ 60 Hz Toshiba induction motor drives the pump by belt. The pump flow rate is regulated by adjusting the motor rpm which is controlled using a Toshiba Inverter Frequency Controller with a 0-60 Hz range. The water tunnel with a generic sketch of a tunnel's square test section is given in Figure (3.2) for the purpose of defining spatial coordinate notation and indicating the direction velocity flow. The inlet flow to the test section is conditioned with a series of honeycombs and high-porosity screens to straight the flow and break up large eddies generated in the pump and reduce the turbulence intensity in the test section to be approximately less than 1 % for the maximum velocity.

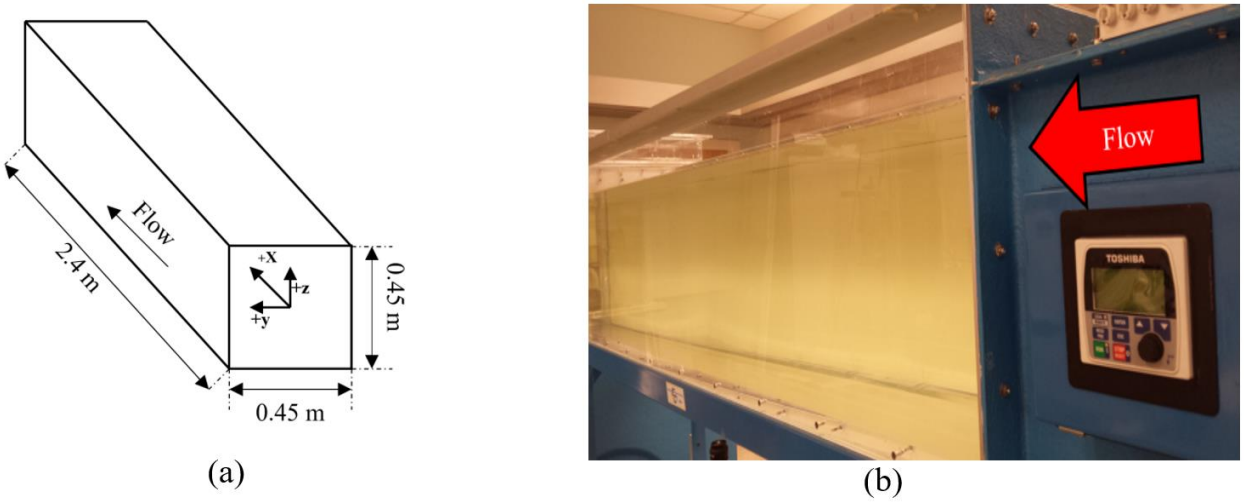

Figure 3-2: Water tunnel setup and the corresponding coordinate system, (a) coordinate system and dimensions, (b) water tunnel controller and test section

PIV measurements were first carried out along the centerline of the channel without any grid installed to measure the free streamwise turbulence intensity, which was found to be around 0.5% at the entrance and reducing downstream. The baseline turbulence intensity was insensitive to the flow speed. The grid is installed downstream of a 6:1 contraction at the entrance to the test section. Measurements were conducted with three nominal inlet speeds (U_∞): 0.9 ms^{-1} for grid N4 and 1.3 and 1.5 m$s^{-1}$for grid N3. The incoming water speed in front of the grid is slightly smaller than the water speed without the grid owing to blockage of the grid. This drop depends on the blockage ratio of the insert grid, and thus the exact incoming water speed might vary slightly between experiments. The flow speed in the water tunnel was set to be nominally 0.9 m/s, 1.3 m/s, and 1.5 m/s using Toshiba inverter frequency controller via adjusting the frequency of the pump (25 Hz ≈ 0.9 m/s, 35 Hz ≈ 1.3 m/s and 40 Hz ≈ 1.5 m/s.

3.4 Quantities and parameters of the fractal grid

Space filling square fractal grids are used in the present work, consisting of the repetition of a square pattern at different scales. Two space-filling fractal square grids have been used in the water tunnel experiments reported here. The grids are referred to as N3 and N4 corresponding to the number of fractal iteration (N) the thickness ratio (t_r). Generally, fractal grids can be characterized by:

- The number (S) of rectangular bars (in the case of fractal square grids S=4).

- The number of fractal iterations (N).
- The length L_0 and thickness t_0 (in the plane of the pattern, normal to the mean flow) of the largest bar in the grid.
- The ratios of the bars' length and thickness between each iteration (R_L, R_t); These scaling factors are independent of j (the scale-iteration) and are smaller than or equal than 1/2 and 1 respectively.
- The number B^j of patterns at each scale-iteration.

A complete design of the grids can be done with these parameters. Other quantities can be derived from these independent geometrical parameters, such as the bars' length and thickness at each scale iteration j:

$$L_j = R_L^j \, L_0 \tag{3-1}$$

$$t_j = R_t^j \, t_0 \tag{3-2}$$

Note that:

$$L_0 \equiv L_{max}, L_{N-1} \equiv L_{min}, t_0 \equiv t_{max} \text{ and } t_{N-1} \equiv t_{min} \tag{3-3}$$

To ensure that the grid will fit into the tunnel, the following constrain equation has to be applied:

$$T = \sum_{j=0}^{N-1} L_j + t_{N-1} = L_{max} \, (1 + R_L + R_L^2 + R_L^3) + t_3 \tag{3-4}$$

Where, T is the water tunnel width. A gap space should be left around the out side of the grid inside the tunnel; this space was left to allow for a frame around the grid to hold it in place. A base made from aluminum is used to secure the grid. The base was connected to the front of the biggest bars in a way that will not effect the flow. The thickness of the base's bars was sufficient to prevent the grid from any vibration. (Stefan, 2011) in his work mentioned that having free flow around the grid does not effect the statistical properties of the flow at the centerline.

Other parameters can be defined from above parameters, such as the thickness ratio defined as:

$$t_r \equiv \frac{t_0}{t_{N-1}} \equiv \frac{t_{max}}{t_{min}} \tag{3-5}$$

$$t_r = R_t^{1-N} \tag{3-6}$$

Also, the blockage ration σ has been defined by Hurst & Vassilicos as the ration between the total area of the grid to the total size of the grid which might be equal to the cross-sectional area of the tunnel as:

$$\sigma = \frac{A}{T^2} = S\left(\frac{L_0 t_0}{T^2}\right)\left[\frac{1-(BR_tR_L)^N}{1-BR_tR_L}\right] \quad \textbf{(3-7)}$$

Bar sizes and local blockage are inhomogeneously distributed across the fractal grids. The scaling exponent (known as a fractal dimension) that characterizes the fractal perimeter defined as:

$$D_f = \frac{\log B}{\log\left(\frac{1}{R_L}\right)} \;\; ; \;\; 1 \le D_f \le 2 \quad \textbf{(3-8)}$$

Also, an effective mesh size was introduced by [Hurst & Vassilicos 2007] as:

$$M_{eff} = \frac{4T^2}{P}\sqrt{1-\sigma} \quad \textbf{(3-9)}$$

where *P* is the fractal perimeter length of the grid. This effective mesh size is an average mesh size introduced by [Hurst and Vassilicos, (2007)] to be fluid mechanically relevant for multiscale grids.

3.5 Estimation of the turbulence intensity value and peak location based on literature review

Clearly, there are multiple independent parameters defining a fractal grid, but no analytic formula prescribing the choice of parameters to achieve certain turbulence properties. The current work therefore drew on previous experiments to guide the design of grids to achieve flow properties required for future turbine rotor testing. Previous experiments were conducted to study the estimation of the turbulence intensity, its peak value and turbulence intensity peak location [Hurst and Vassilicos, (2007), Stefan, (2010), Mazellier and Vassilicos, (2010), Laizet and Vassilicos, (2011), Discetti, et al., (2011), and Gomes, et al., (2012)]. Hurst and Vassilicos reported that the turbulence intensity increases till it reaches its peak value at $x_{peak} = 75\frac{t_{min}T}{L_{min}}$ downstream from the grid. The turbulent is predicted to last for $l_{turb} = 0.1\lambda\frac{U\lambda}{v}$ beyond the turbulence intensity peak location, where λ is Taylor microscale, U is the mean speed of the flow and v is the kinematic viscosity of the fluid. The turbulence decays exponentially ($u'^2 = u'^2_{peak}\exp[-(x - x_{peak})/$

l_{turb}]) for downstream beyond x_{peak}. These sizing rule results were obtained for low blockage ratio (σ =25%) with N = 4 fractal iterations. Hurst and Vassilicos concluded that the size of the smallest bars in the grid have strong influence on the turbulent peak position. However, this was not the case for Mazellier & Vassilicos, (2010). They stated that the turbulent peak value and position are effected mainly by the largest bars in the grid, due to the fact that the turbulence results from the interactions between the wakes of the different bars which have different sizes and the most downstream interactions are caused by the biggest bar sizes. Mazellier & Vassilicos introduced a so called wake-interaction length scale $x_* = L_0^2/t_0$, and predicted a TI peak at $x_{peak} = 0.45x_*$. They confirmed exponential decay, introduced by Hurst and Vassilicos, with a slight adjustment to $\frac{u_c'^2}{U_c^2} = A\ exp[-B\left(\frac{x}{x_*}\right)]$ where A and B are dimensional parameter and dimensionless parameter which shifts the predictions. The TI peak value is $\frac{u_c'}{U_c} = \sqrt{A\ exp[-B\left(\frac{x}{x_{peak}}\right)]}$. Stefan (2010) found for fractal square grids the location of the peak TI lies in this range $x_{peak}^{TI} \approx (0.3 - 0.45)L_{max}^2/t_{max}$. However, Laizet and Vassilicos, (2011) reported that Mazellier & Vassilicos's formulas for the estimation of the TI peak location do not fit their results, because their grids have iteration N=3 and blockage ratio varies from σ =23-32 %, while Mazellier & Vassilicos results were obtained for low blockage ratio (σ =25%) with fractal iteration N=4; evidently these two grid parameters can significantly affect the position x_{peak}. Therefore, they expected the location of TI peak to be $x_{peak} = C(N,\sigma)\frac{L_0^2}{t_0}$, where $C(N,\sigma)$ is dimensionless coefficient proportional to the fractal iteration and the blockage ratio, in their case $C(3,\sigma) \approx \frac{5}{4}\sigma$. Discetti, et al., (2011) presented results for an N=4 grid where the peak location is $x_{peak} = 0.5\frac{L_0^2}{t_0}$. Gomes, et al., (2012) investigated fractal generated turbulence in the water tunnel using PIV. They modified the wake-interaction length scale for fractal-generated turbulence, which was defined by Mazellier & Vassilicos, (2010), taking in their consideration the free stream turbulence intensity yielding $x_*' = \frac{L_{max}^2}{\alpha C_d t_{max}}$, where C_d is the drag coefficient and α is a parameter taking into account the background turbulence intensity of the flow in the absence of the fractal grid obstruction. In their work the location of the peak TI was defined as $x_*^{peak} = 0.21\frac{L_{max}^2}{\alpha C_d t_{max}}$. As shown later in

section 3.7.2 results, the decay found in the current work was $x_{peak} = 0.8\frac{L_{max}^2}{t_{max}}$ for the N3 grid and $x_{peak} = 0.85\frac{L_{max}^2}{t_{max}}$ for the N4 grid. Gomes et al introduced a turbulence intensity scaling relation for the peak turbulence intensity $(\frac{u'}{U_\infty})_{peak} = \frac{1}{\beta}(\frac{C_d t_{max}}{x_*^{peak}})^{\frac{1}{2}}$, where β is a parameter taking into consideration the effects of background TI on the peak value of TI. This relation was used to predict the peak value of the turbulence intensity for fractal square grids taking into account the flow conditions.

Table 3.1 summaries the predicted turbulence locations and intensities from the full range of prediction formulas found literature. A range of parameter values were examined to select grids to build for the current set of experiments. The aim was achieving the largest possible turbulence intensity (real world values for tidal/river flows in the range of 10-20%) at a peak turbulence location within the test section length to enable positioning of the rotor rig apparatus within the turbulent flow region.

Table 3.1: Predictions of TI peak value and location based on literature prediction formulas.

N	D_f	σ (%)	t_r	R_t	R_L	L_0 (mm)	L_1 (mm)	L2 (mm)	L_3 (mm)	t_0 (mm)	t_1 (mm)	t_2 (mm)	t_3 (mm)
4	2	27	13	0.425	0.5	212.09	106	53.03	26.5	20.8	8.86	3.75	1.6
3	2	20.4	13	0.28	0.5	212.09	106	53.03	:	26	7.28	2.03	:
3	2	27	5.55	0.425	0.5	212.09	106	53.03	:	25	10.6	4.5	:
3	2	25.5	13.76	0.27	0.5	235	117.5	58.75	:	28	7.56	2.04	:

N	TI peak position x_{peak}(mm)				TI peak value (%)	
	Hurst & Vassilicos (2007)	Mazellier & Vassilicos (2010)	Discetti et al (2011)	Gomes et al (2012)	Hurst & Vassilicos (2007)	Gomes et al (2012)
4	2032.70	973.17	1081.30	719.27	5.6	5.8
3	1297.49	778.54	865.04	575.42	7.8	11.8
3	2874.29	809.68	899.64	771.56	5.4	9.8
3	1172.60	887.54	986.16	601.32	8.9	12.5

Due to the water tunnel channel's geometry, only 4 different grid options are considered here. The one should be selected is the one needs to meet some conditions; such that the TI peak value and location should appear between the mid-channel and the end of the channel. This leaves an enough distance for the turbulence to build-up and become homogeneous before it reaches the rotor (which installed around the end of the channel). Thus, the highlighted ones are the ones that are selected among the others in this work. The grid N4 is the first one that is being selected. It is selected because of that, from the prediction formula, the TI peak location appears around the mid-channel. So, it has been thought that this works well and meets the required conditions. Unfortunately, the TI peak appears much further downstream than what is being estimated, which makes this grid (N4) not suitable for this work. The second one that is selected is the highlighted green one, grid N3. This grid gives good results regarding the TI profile. The two grids have the same blockage ratio ($\sigma = 0.27$) and the distance between the thickest bars (L_0). They differ by t_r and number of iteration N. Two different thickness ratio are used: 5.5 and 13. Generally, the properties of the turbulence, that created by fractal grids, can be changed by changing the above parameters and quantities. A quantitative description of the selected fractal square grids is highlighted and given in Table 3.1. The grids used for the experiments are designed using Solidworks and manufactured from an acrylic plate with a constant 6mm thickness in the direction of the mean flow irrespective of the iteration using leaser cutting machine as can be seen in Figure 3.3. Figure 3.4 shows the manufactured grids. The grids referred to as grid N3, and grid N4. Figure (3.4c) shows the base that is used to hold the grid into the water tunnel. The grid is assembled on the base, then the base with the grid is installed on the channel's lid through a hatch.

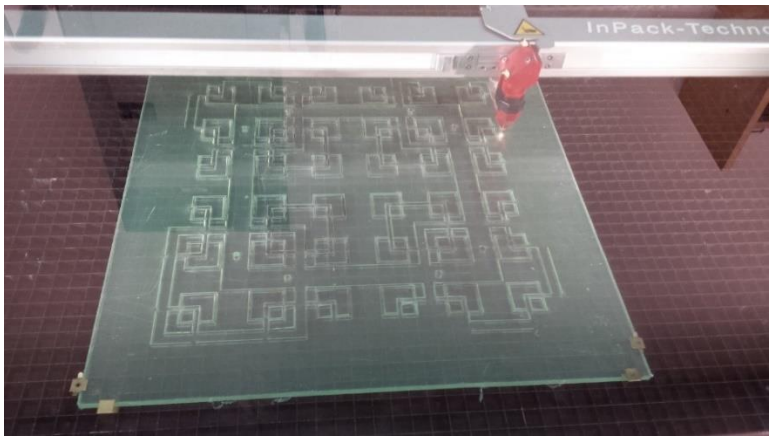

Figure 3-3: Manufacturing the grid using a leaser cutting machine, the accuracy of the manufacturing cutting laser machine is about 0.15(mm)

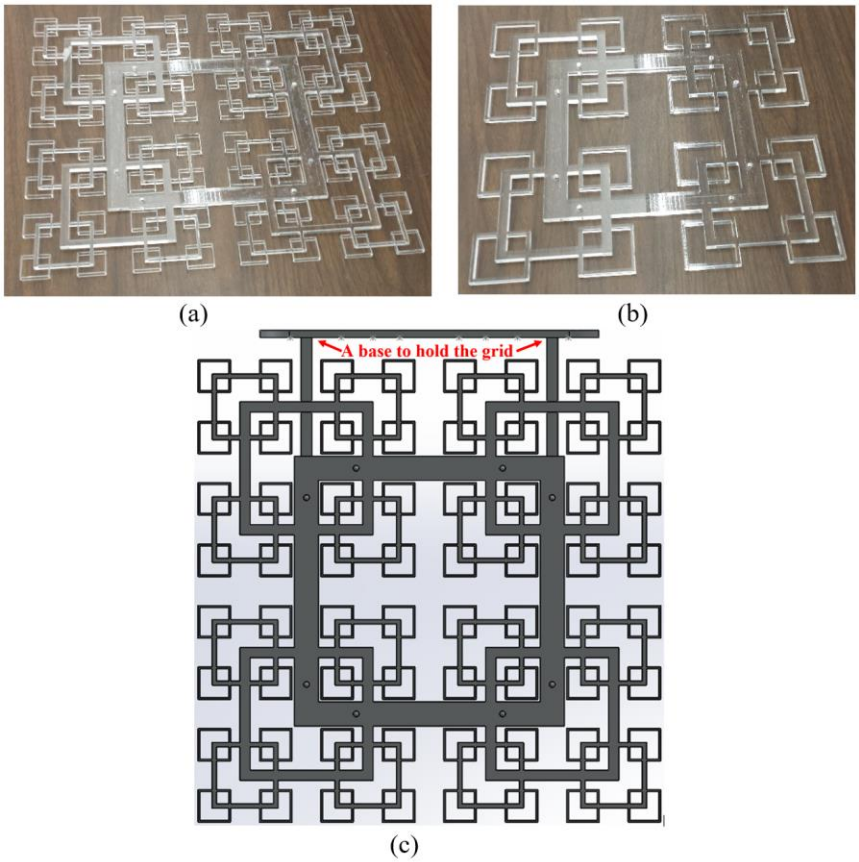

Figure 3-4: The manufactured grids, (a) the N4 grid, (b) the N3 grid, (c) the grid with its base

3.6 Experimental technique

The flow is interrogated with two-dimensional PIV. SH400S20 Silver-Coated hollow glass sphere tracer particles of 13 µm mean diameter and 1.6 specific gravity were added to the flow. The particles are inertial; i.e. because of the fact that the particles have size and density, they have inertia relative to the flow and thus may behave differently. However, with the assumption that the particles follow the flow they are used to help measure fluid flows with PIV by enhancing reflectively. Their motion is influenced by the Stokes number, defined as the ratio of the time (that the particle takes to respond to changes in the flow) to the timescale of the flow [Peter, (2008)]. The Stokes number is one of the most important parameters describing the behavior of inertial particles in a fluid flow and which must be less than 1 for the particles to obey the flow-following assumption.

A Nd:YLF laser (class IV High Power Laser) is used to illuminate the flow. The recording rate is set depending on the flow velocity and size of the interrogation window; it can be fine -tuned to provide an optimal particle displacement from the first image to the second. The recording rate is set to be 950 Hz, 1300 Hz, and 1500 Hz for flow velocities 0.9 m/s,1.3 m/s, and 1.5 m/s respectively. A horizontal laser sheet with minimum thickness of around 2 mm is formed at the horizontal mid-plane of the channel to illuminate the desired field of view. A CCD camera (LA-Vision VC-Imager Intense) is mounted on rails under the water tunnel test section looking perpendicular to the light sheet from the bottom to record the PIV images with 1024X1024 pixel resolution. The Darwin Laser Head is placed on another set of rails mounted on a table besides the tunnel test section, Figure 3.5. This configuration allows optical access along the channel. The camera is synchronized with the laser sheet pulse. A Nikon 50mm f/1.8D AF Nikkor lens is used with the camera to capture wide images in order to reduce the total number of camera locations along the channel. The time interval between images dt depending on the mean flow velocity and can be controlled by changing the recording rate. The time delay between the illumination pulses must be long enough to be able to determine the displacement between the images of the tracer particles and with sufficient resolution and short enough to avoid particles with an out-of-plane velocity component leaving the light sheet between subsequent illuminations [Raffel, et al., (2007)]. Thus, the displacement of the particle images between the light pulses is set to be maximum 8 px. A single frame mode is used to take images (to record the light scattered by the particles).

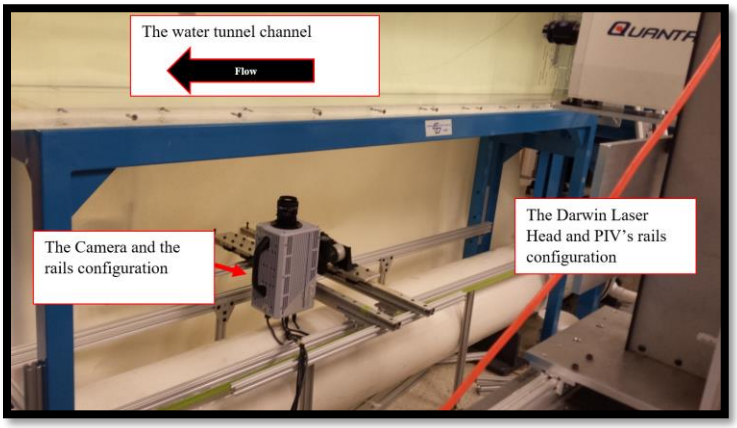

Figure 3-5: The experimental set up

The images were recorded immediately downstream of the grid all the way downstream along the channel along the centerline. There were 14 camera positions, and 3000 images are taken for each camera position to ensure an acceptable level of uncertainty in the calculated fluctuation and mean velocity fields. The PIV data were processed using the commercial software Davis, v7.2. The software splits up each image into a set of interrogation windows. For every window in the first image, there is a corresponding window in the next image. With the assumption that within one interrogation window, all particles moved homogeneously between the two illuminations, the local displacement vector for the images of the tracer particles of the first and second illumination is determined, by means of statistical methods (auto- and cross-correlation), for each interrogation area Raffel, et al., (1998-2007)

Once the time averaged and fluctuation velocity fields are calculated for each camera position, they are stitched together using linear interpolation in overlapping regions to create a single continuous vector field for the entire channel. This continuous vector field is used to calculate other statistical properties of the flow, such as turbulence intensity, using Matlab.

3.7 Results

3.7.1 Fractal grid wakes

Figure 3.6 shows PIV results for two camera position (position one and two) immediately downstream of the grid N 3 at flow velocity 35 Hz ≈ 1.3 m/s. The 0.0 location shown in the Figure donates that the 0 coordinate in the y direction is at the center of the grid, and the 0 coordinate in the x direction is 18.2 cm downstream the grid. One can notice that there is a strong jet-like behavior represented in red at the center of the grid where there are no bars blocking the flow. It is wider close to the grid and becomes narrower farther downstream from the grid. The velocity deficit behind the grid is visible on each side, caused by the presence of grid bars. It seems to be symmetric in the spanwise direction. The maximum value of the speed appears exactly at the center of the grid having value close to 1.7 m/s, 30% higher than freestream. The velocity decreases below the freestream far from the center line in the spanwise direction. The wakes from the smallest bars might be dominated by the wakes of the biggest bars but their contribution can not be neglected for small or big values of t_r.

(a)

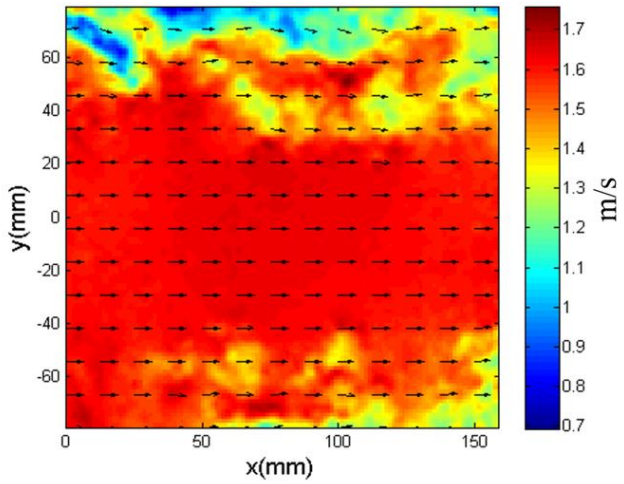

(b)

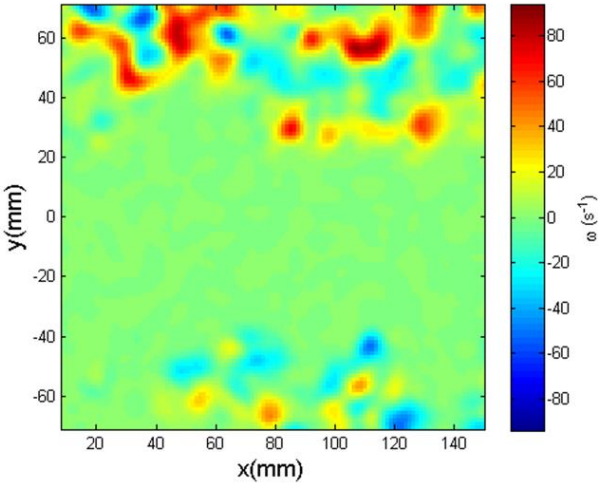

(c)

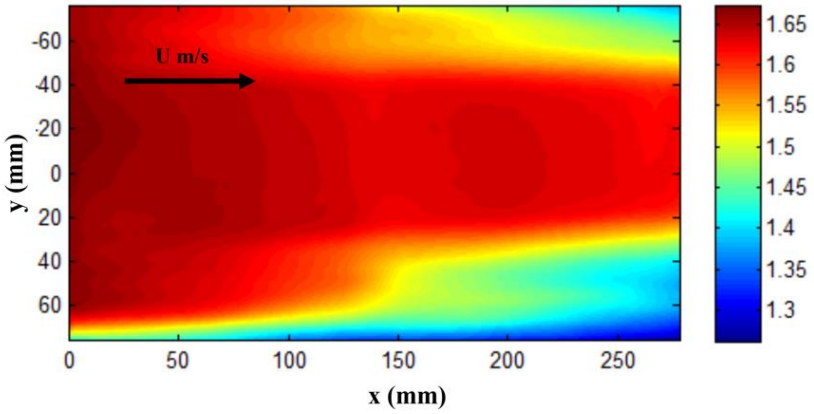

Figure 3-6: Fractal grid wakes (N=3, U= 1.3 m/s). (a) typical instantaneous velocity. (b) vorticities created by fractal elements. (c) contour of averaged flow velocity

3.7.2 Normalized and non-normalized turbulence intensities

Figure 3.7 shows the centerline turbulence intensity behind the fractal grids with streamwise distance for the two grids N3 and N4, and two inlet velocities for grid N3. The lowest peak turbulence intensity value and furthest occurs on the centerline [Laizet and Vassilicos, (2011)]. This means that at any distance downstream of the grid as we go in the spanwise direction we might find the turbulence intensity has higher values, in the direction of the spanwise, than its values on the centerline. However, the centerline TI profile is the only one is being concern about inhere because the model of the rotor will be deployed at the centerline.

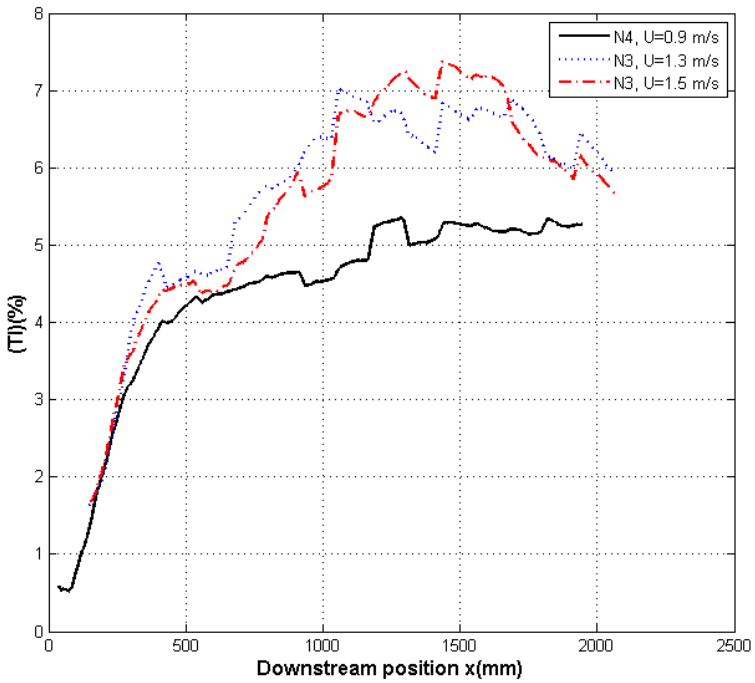

Figure 3-7: Streamwise evolution of the centerline turbulence intensity as a function of downstream position x

Evidently the turbulence intensity peak value is approximately the same for the grid N3 at the two different flow velocities. This agrees with [Mazellier and Vassilicos, 2010] results for wind tunnel experiments, confirming that peak turbulence intensity is independent of the flow velocity for water measurements. Moreover, the data shows that for both velocities for the N3 grid the peak of TI has value of 7.4% and at 1440 mm downstream the grid. From the Figure, it can also be seen

that the peak of turbulence intensity for the N4 grid is further downstream and located at x=1822mm. Interestingly, increasing the number of iterations by one from N=3 to 4 and reducing the thickness ratio from 13 to 5.55 by changing the thickness of the biggest to the smallest bars in the grid (t_0-t_{min}), to have the same blockage ratio, has a significant effect on the TI peak value and position. The TI peak value increased by roughly 30 % to be 7.4 % and the peak position shifted 380 mm up-stream. However, from Figure 3.7 it can be noticed that the development of the flow in the wake of the N4 grid seems to not be fully developed, but is constrained by the limit of the channel length. Also, the TI keeps increase till the end of the channel. The TI for two grids grows sharply in the region of less than 500 mm downstream of the grids, then for the grid N3, increases faster than in the grid N4. There is no decay region in the N4 grid, only the production region because of the limited experimental facilities. In the flow behind the grid N3, there are both production and the decay regions and the decay region in N3 smaller than the production region only because the tunnel's test section is short for a full study of the decay region.

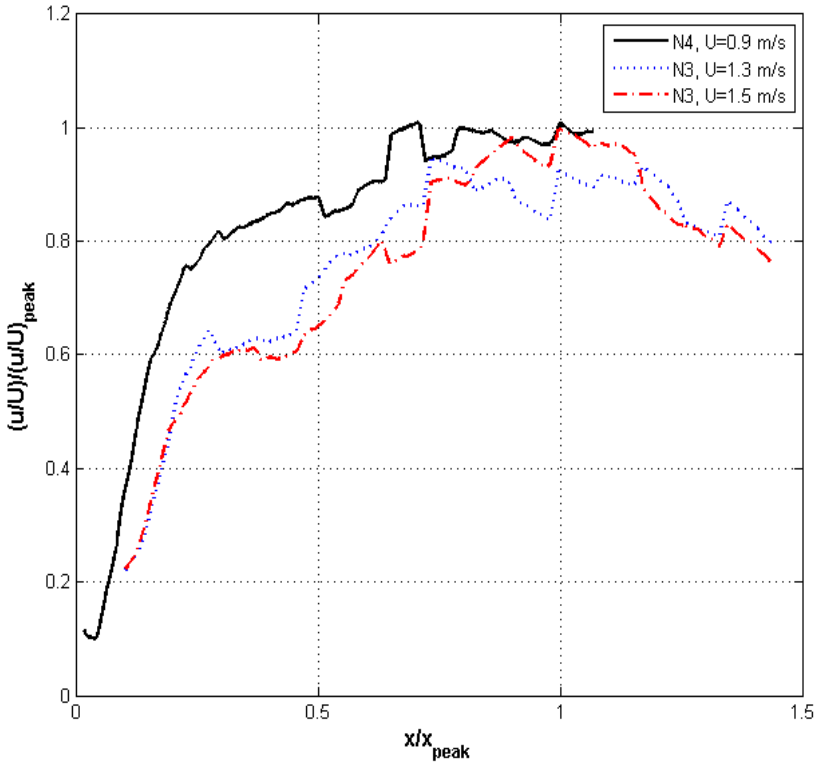

Figure 3-8: Streamwise evolution of the centerline turbulence intensity as a function of x scaled by x_{peak}; turbulence intensity is normalized by its peak value

Figure 3.8 shows the streamwise development of turbulence intensity values for the two grids in relation to x/x_{peak} for the three different velocities in the range studied with the turbulence intensity scaled by its peak value. Mazellier & Vassilicos, (2010) reported that the streamwise evolution of the centerline turbulence intensity can be collapsed by using the peak turbulence intensity. Comparing data for U=1.3m/s and U=1.5m/s for the same N3 grid, it can be said that they are practically the same given the somewhat noisy dataset. Figure 3.8 also shows that both cases U=1.3 m/s and U =1.5m/s have similar overall profile. The N4 grid does not collapse onto the N3 results in the production region, having overall higher normalized values. Again, due to tunnel length limitations, the downstream evolution of the TI could not be fully compared to the N3 grids, but it appears to become more similar in the dissipation region.

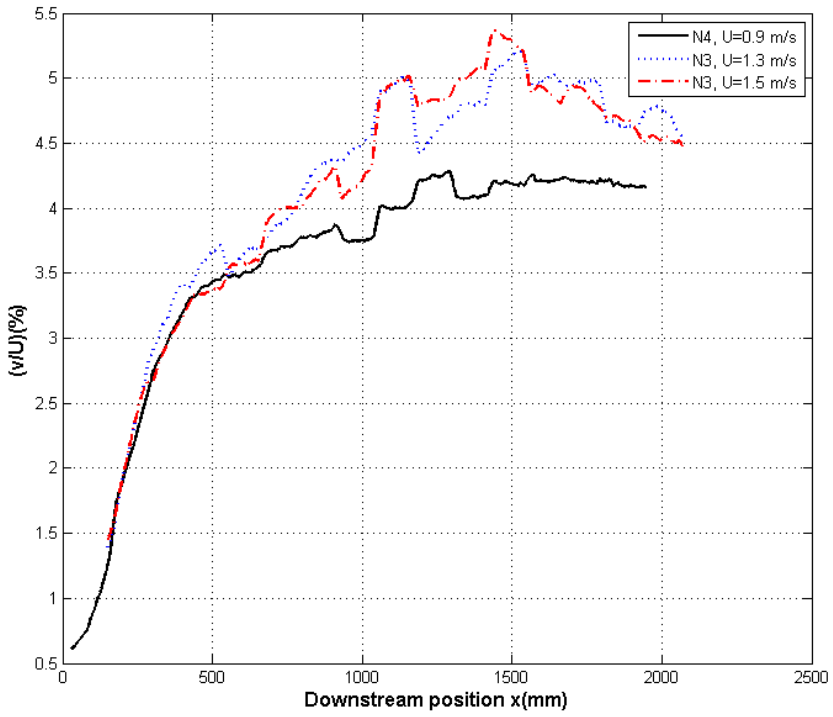

Figure 3-9: Spanwise component of TI evolution along the centerline as a function of x for N3 and N4 grids.

Figure 3.9 shows the spanwise component of turbulent intensity for the two grids. Again, the N3 grid results at both flow speeds are quite similar, both in terms of peak magnitude and position. However, the spanwise turbulent intensity is lower in magnitude compared to the streamwise component, regardless of the type of grid used. It can be concluded that the TI peak position and

magnitude can be strongly effected by smallest bars' size given the differences between the N3 and N4 grids.

Comparison between the obtained results with the predictions is contained in table 3.2. In the case of N4 grid, there is a difference ranging from 10.4 to 46.5 % between the obtained results and the estimated ones for x_{peak}. This differences decreased to be max 8.6 % for predicting the TI peak value for the same grid. On the other hand, the difference in TI peak value for N3 grid is much higher then that one of N4 grid. In overall, these prediction rules seem to not give really accurate estimations for both TI peak value and location. However, it is still good for using to be guides rules for designing fractal grids.

Table 3.2: Comparison between the Predictions of TI peak value and location and our results

Grid	Predictions based on the existing literature						Our results		Differences (%)	
	TI peak position x_{peak} (mm)				TI peak value (%)		TI peak position x_{peak} (mm)	TI peak value (%)	x_{peak}	TI value
	Hurst & Vassilicos (2007)	Mazellier & Vassilicos (2010)	Discetti et al (2011)	Gomes et al (2012)	Hurst & Vassilicos (2007)	Gomes et al (2012)				
N4	**2032.70**	**973.17**	**1081.30**	**719.27**	**5.6**	**5.8**	**1820**	**5.3**	10.4-46.5	5-8.6
N3	**2874.29**	**809.68**	**899.64**	**771.56**	**5.4**	**9.8**	**1440**	**7.4**	37.5-50	24.5-27

3.7.3 Mean velocity profile downstream of the grid

Velocity profiles at a number of spanwise points behind the N3 grid, U=1.5 m/s, can be seen in Figure 3.10. These points are at the centerline, fear off-centerline, and in between. There is a noticeable difference in the magnitude of the velocities at these points. Profiles of points that are extreme off-centerline shows sudden decrease in their magnitude; this drop is because of the obstructions of the small elements of the grid. Meanwhile, centerline points have gradually decreasing along the channel. Off-centerline velocity profiles keep going down till distance of 1.25m then relatively increase because they are effected by the centerline high speed. Overall, the velocity profiles are wide at the middle then it narrows down when it reaches at a point very close

to the location of the TI peak. This (decreasing in the velocity profiles at the centerline) is totally opposite what happen in the case of cross and I fractal grids. The velocity profiles in cross and I grid found to be increase with increasing downstream distance [Hurst & Vassilicos, (2007)]. One can point out that the rate of the change in flow speed behind the fractal grids is faster than those of fractal cross and I grids, which makes fractal square grids have longer production region.

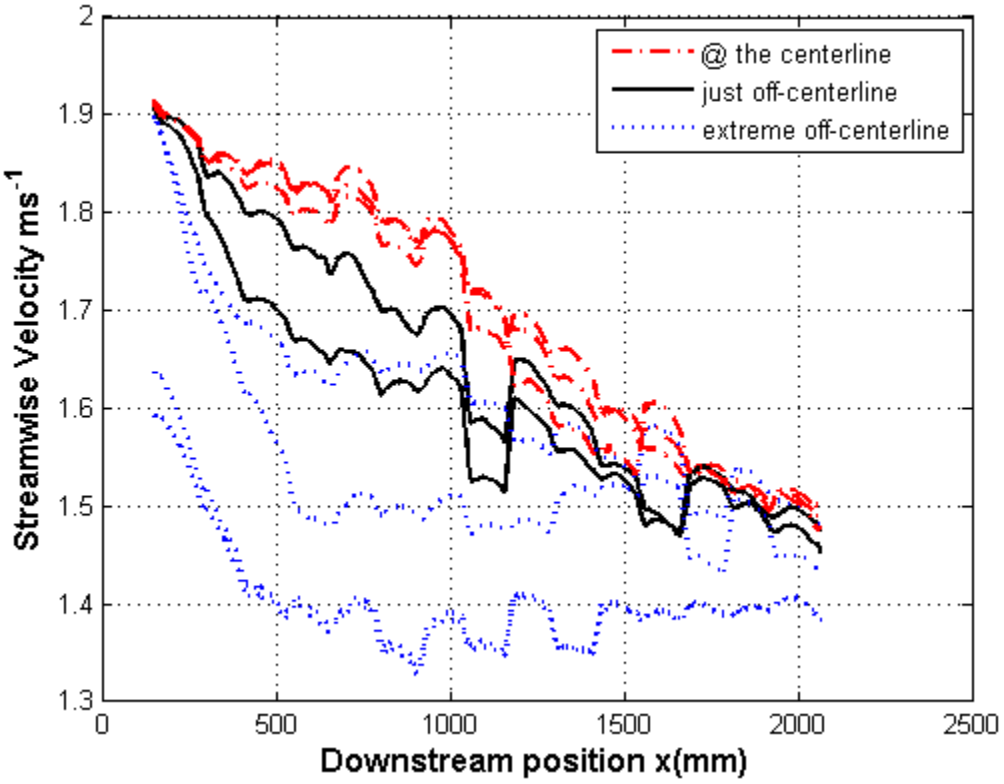

Figure 3-10: Velocity profile behind the grid along the channel (N3, U=1.5 m/s)

Figure 3.11 shows comparison between the spatial average streamwise velocity, along the centerline, in the wakes of each grid. For all grids, the flow velocity started with a high value just downstream of the grid and remains so for a distance, then decreases toward its normal value. Interestingly, it is clear that the data from the N3 grid at the two different velocities exhibits similar behavior; the U = 1.5m/s is just shifted up by 0.25m/s. The flow behind N4 reaches the nominal value at the middle of the channel along the centerline at around x = 1.25 m. On the other hand, the N3 grid flows reach the nominal value close to the TI peak position. From this, one can conclude that the average flow velocity is altered in the production region, then becomes roughly constant in the decay region. It is also confirmed that the TI peak location is independent of the

value of the average velocity. For larger t_r the streamwise velocity decreases faster with increasing x agreeing with the results from Hurst & Vassilicos, (2007).

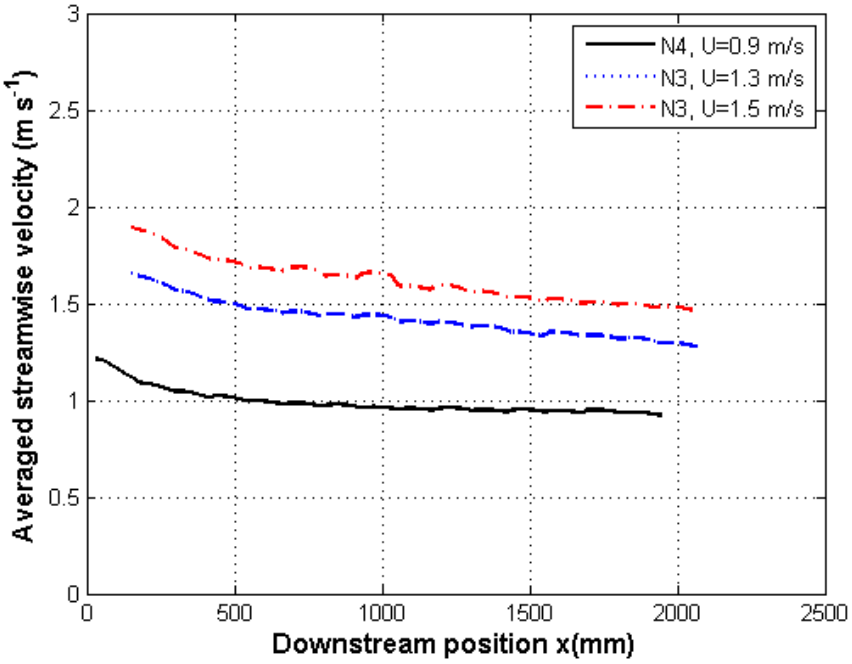

Figure 3-11: Average streamwise velocity along the centerline

Figure 3.12 presents a visualization of the average streamwise velocity component distribution for grids N3 and N4. By looking to the Figure, it is very clear to see that the grid works as a jet behavior, whereas the average streamwise velocity distribution is like a jet flow distribution. This behavior is resulted from the opening at the center of the grid where σ is locally smaller than the rest of the grid. This jet-like is the main reason that makes the flow velocity has maximum value at distance very close to the grid; due to the fact that, there is no elements in the region in the center of the grid, which causes of a relative low blockage ratio in the centerline. It can be observed that for the two grids a very nonhomogeneous velocity field is obtained close to downstream grid side. Fractal square grids generate turbulence with increasing turbulence intensity and the homogeneity simultaneously [Hurst and Vassilicos, (2007); Mazellier and Vassilicos, (2010); Laizet and Vassilicos, (2011)]. In distance $x < x_{peak}$ the flow looks inhomogeneous, this is in agreement with the results of [Discetti, et al., (2011); Gomes, et al., (2012)]. However, the homogeneity of the velocity distribution is improving while we are moving further downstream. Even though both grid have same solidity, in case of N4 the turbulence remains non-homogeneous for a longer

distance downstream of the fractal grid. Therefore, the homogeneity of the flow seems to be independent of the grid's solidity; and it is strongly effected by the opening at the grid' center.

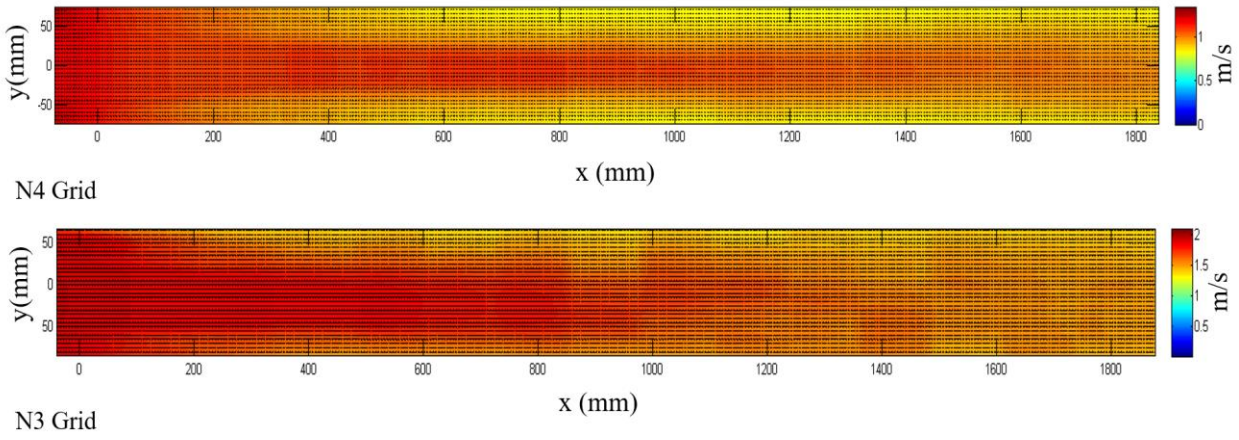

Figure 3-12: Mean velocity field downstream the grid along the channel

In the N3 grid, the flow reaches its homogeneity in distance closer to the grid than in N4. This can also give a reason for why (in case grid N3) the turbulence intensity peaks at location closer than in the case of N4 grid. Furthermore, when t_r is decreased, whilst keeping the same σ, the flow seems to be more homogeneous very far downstream. The opening at the grid's center seems to have effects on the TI peak location, whereas increase this opening by reducing the fractal iteration (N) seems to lead to shift x_{peak} upstream.

3.7.4 Large-scale isotropy

Taylor, G. I., (1935) reported that turbulence is isotropic when the magnitude of the mean of any velocity fluctuation component is constant in relation to rotating the referential axes in any manner. In this work, large-scale isotropy is the variation of the ratio of root-mean-square (r.m.s.) velocities in the streamwise and spanwise directions $\frac{u}{v}$. Figure 3.13 shows the global isotropy of velocity fluctuations with downstream distance along the centerline. From this Figure one can observe that for the N4 grid $\frac{u}{v}$ values at locations $x > 0.2\,x_{peak}$ downstream of the grid roughly equal 1.2 and it remains so till $^{x}/_{x_{peak}} = 1$ then increasing slightly to around 1.25. This result agrees with the results of Gomes, et al., (2012). The N3 grid $\frac{u}{v}$ values vary approximately between 1.2 and 1.5 for $x > 0.2x_{peak}$ comparable to the results obtained by Hurst & Vassilicos, (2007). There is a distance

very close to the grids $x < 0.2x_{peak}$ where $\frac{u}{v}$ has values that are much smaller than 1.2; this region, which is the so-called anomalous region Stefan, (2011), is the same region where the flatness has very unusual values (explained later in detailed in the section 3.7.5). It can be concluded that at a distance far enough from the grid, the turbulence isotropy can be comparable with Hurst & Vassilicos, (2007)' results. It is also clearly evident that the fractal grid generated turbulence is in fact anisotropic, a topic that should be further investigated relative to detailed field measurements in tidal flows as that data becomes available. It is expected that real turbulence is indeed anisotropic owning to bathymetry and water depth constraints, but the exact levels of anisotropy are yet to be quantified in detail.

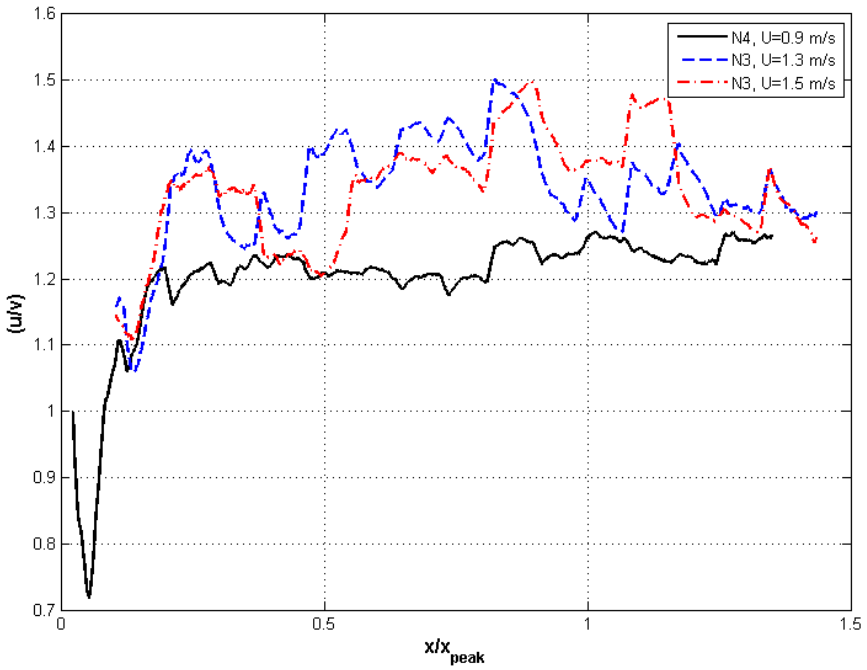

Figure 3-13: Global isotropy parameter u/v as a function of the distance downstream of the fractal grid N4

3.7.5 Flatness of the velocity

Figure 3.14 presents the flatness of the longitudinal fluctuating velocity along the centerline. The values are normalized by factor of 3, so that a value of 1 corresponds to a Gaussian distribution of the velocity fluctuation.

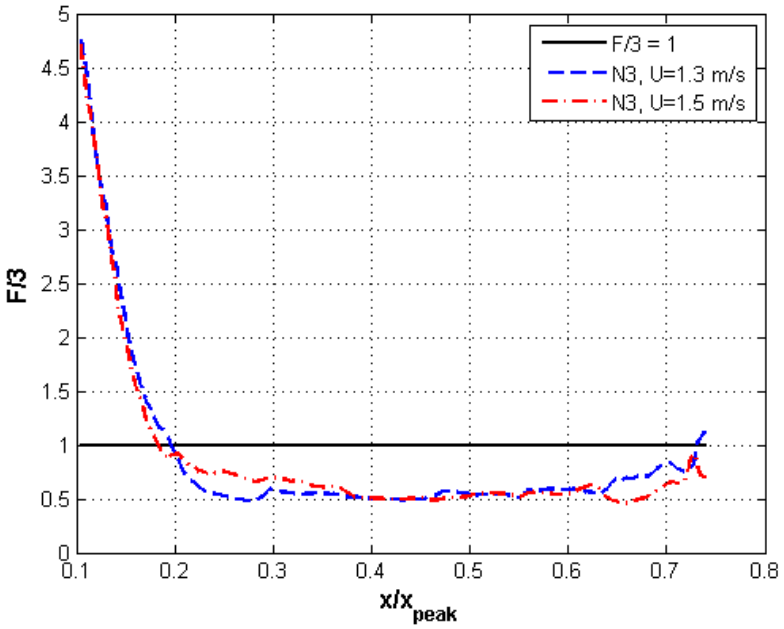

Figure 3-14: Centerline evolution of flatness

From the Figure, it is clear that the flatness of the fluctuation velocity is independent of flow speed. It can also be observed that the flatness is large immediately downstream of the grid. These results agree with other results were reported in literature for wind tunnel experiments [Mazellier & Vassilicos, (2010); Stefan, (2011)]. By looking at the Figure one can also notice that that flatness has values that are much greater than 3. These extreme values downstream of the grid occur at $x < 0.2x_{peak}$, meaning the fluctuations are not normally distributed in this region. Mazellier and Vassilicos, (2010) found that the flatness of the fluctuating velocity behind near the grid is highly non-Gaussian, peaking at around $x = 0.2\ \frac{L_0^2}{t_0}$. Stefan (2011) reported that there is a closed region ranging from about $x = 0.03\frac{l_0^2}{t_0}$ cm to $x = 0.2\ \frac{L_0^2}{t_0}$cm in the downstream direction behind the fractal grid, called anomalous region, characterized by flatness values much higher than 3. It is worth noticing that the flatness has values less than 3 in the production region, increasing to the usual Gaussian value of 3 at locations close to the peak TI and remaining at values fluctuating around 3 for $x > x_{peak}$. The velocity fluctuations in the far region therefore have Gaussian behavior.

3.7.6 Fluctuation and mean flow features

Figure 3.15 shows the velocity fluctuation field downstream the grid along the channel for the both grids. The velocity fluctuating profiles are clearly not uniform across the channel, close to the grids. The inhomogeneity appears longer for N4 than in the case of N3. In the case of N4, the homogeneity starts to show after the mid of the channel then it improves as going further downstream. From the Figure, for the N3 grid, it can be observed that the fluctuation has its high values around $x \approx x_{peak}$, this causes in having peak turbulence intensity at around this location. However, this can not be seen in case of grid N4, this might conform what we have mentioned in section 3.7.2, that the turbulence intensity has not really clear reached its beak and that because of the limit of the channel's length. The fluctuating flow behind N3 stay ununiform for a distance shorter than that in N4. The homogeneity in the horizontal y direction about the centerline seems to be good in the decay region, as can be seen in the Figure.

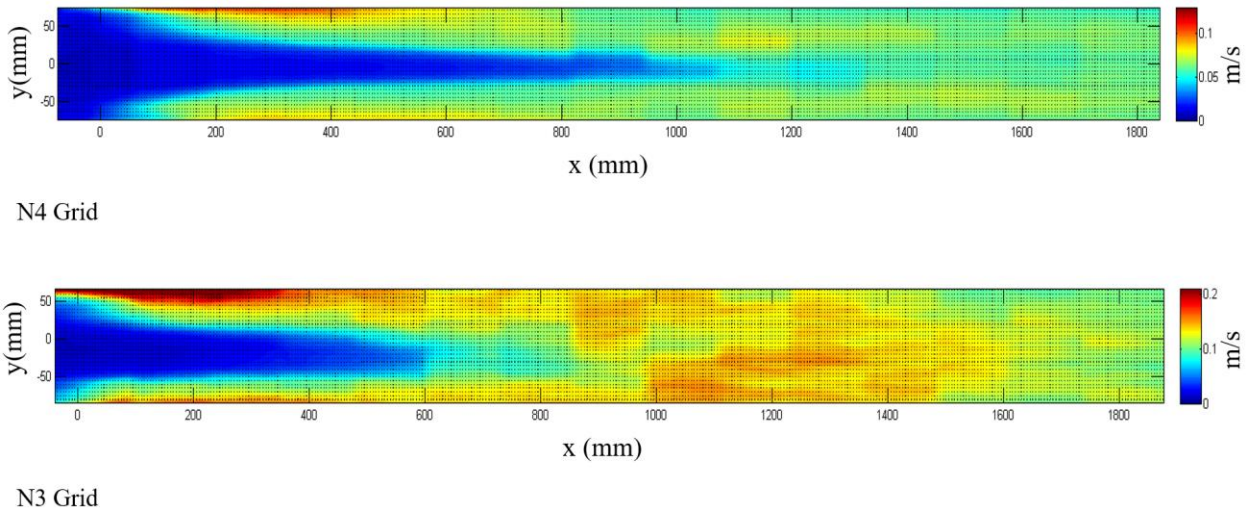

Figure 3-15: Velocity fluctuation field downstream the grid along the channel

3.7.7 Integral length scales and power spectrums

Integral length scale (L_i) can be defined by using the autocorrelation coefficient. The autocorrelation function was computed over a range of delay times τ as $\rho_{uu} = \frac{\overline{u_1(t)u_1(t+\tau)}}{\langle u_1^2 \rangle}$, where u is the fluctuating streamwise velocity component recorded at a point. The integral length scale represents a measure of the longest connection (or correlation distance) between the velocities at a single or fixed point but different times, and thereby a typical size metric of the turbulent eddies

that are created by fractal elements. In the turbulence application, the multiplication of the integral time scale by the mean velocity defines the order of magnitude of macro length scales in the flow. The integral time scale is computed by integrating the autocorrelation function from t=0 to the first instance of ρ_{ii}=0 as $T_i = \int_{t=0}^{t(\rho_{ii}(t)=0)} \rho_{ii}(t)dt$. Figure 3.16 shows the autocorrelation function for both grids N3, and N4 at x_{peak}. The autocorrelation coefficient is unity at a time lag of zero then it decays to zero by increasing time lag. The integral length scales downstream of the grids at the x_{peak} were found to be L_i = 3.7 cm for grid N4 and L_i = 7.7 cm for Grid N3. This means that eddies downstream of the grid N3 are larger than those downstream of the grid N4. This can be expected because the thickness of biggest bar in grid N3 are bigger than the thickness of biggest bare in grid N4. Figure 3.17 represents the power spectral density obtained for grids N3 and N4. Both spectrums show inertial range with slop of -5/3. One can notice that the inertial range starts at lower frequencies for the grid N4, which generates smaller eddies.

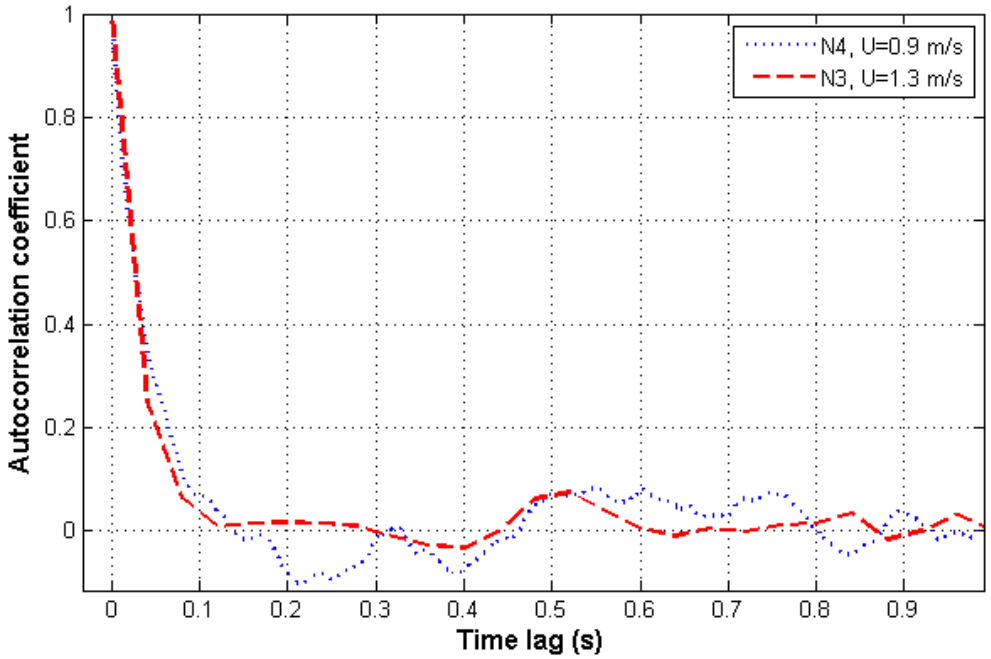

Figure 3-16: Autocorrelation coefficient at x_{peak} at the center line for grid N3 (U=1.3 m/s, @ 35Hz) and N4 (U=0.9 m/s, @25Hz)

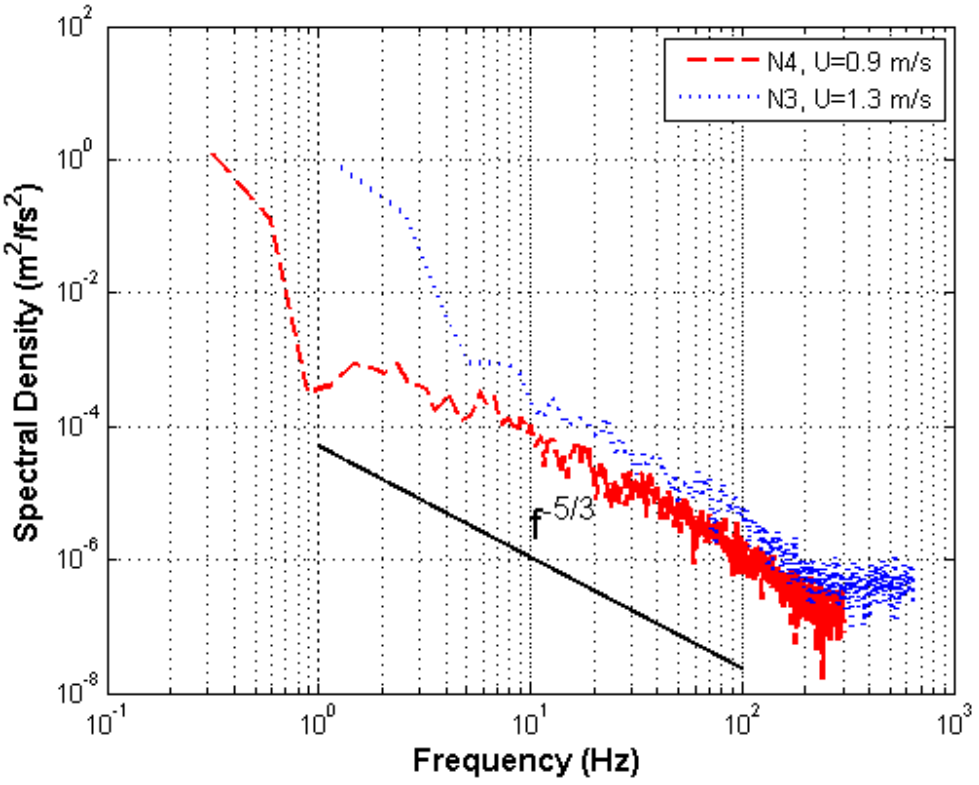

Figure 3-17: Spectra of the stream wise velocity component downstream the grid at x_{peak} for grid N3 and N4

3.8 Conclusion

Realization of multi-scale/fractal generated turbulence by means of using PIV has been presented in this work. The main goal of this work is investigating the effect of changing some grid's parameters on the flow characteristics. And comparing water tunnel experimental results with other wind tunnel results. This study involves calculation of some turbulent statistics such as time averaged velocity, velocity fluctuation, turbulent intensities, development of the flow along the channel in the lee of the grid, global isotropy and flatness. This work also is motivated by other work; whereas we want to study the effect of turbulence on a model of a hydrokinetic turbine and compare the obtained results with other previous results that have been achieved for the same turbine but with smooth flow TI < 0.5%. Moreover, comparison between estimations of the turbulence intensity peak value and location for different papers [Hurst and Vassilicos, (2007); Mazellier and Vassilicos, (2010); Laizet and Vassilicos, (2011); Stefan, (2011); Gomes, et al., (2012)] is presented. Results showed that increasing the size of the smallest element in the grid

has significant effect on the turbulence intensity peak location. The sizes of the biggest bars seem to contribute to a change in the TI peak value. To increase the turbulence intensity peak value, one needs to decrease the number of iteration of the grid with keeping the same solidity of the grid. There is a good agreement regarding to the large-scale Isotropy comparing with other research papers. We found that the ratio of $\frac{u}{v}$ is found to be around 1.2 for N4 and it is ranging between 1.2 and 1.5 for the N3 grid, which is also consistent with other results obtained in fractal square grid experiments. Reducing the opening at the grid's center causes to shift the TI peak location further downstream. Reducing the number of iteration seems to make the turbulence become more homogeneous very far downstream. Results showed that the flow downstream of the grids has different eddies sizes at x_{peak}. This also observed in the autocorrelation function results while the integral length scale downstream of the grid N3 is about 3 times of the thickness of the biggest bars; and downstream of the grid N4, Li is equal to the thickness of the biggest bars in the grid. This means less thickness creates smaller eddies. The power spectrum of the measurement downstream the grid N3 showed more power increase than in the case of grid N4. This might because of the fact that the x_{peak} in the case of grid N4 occurs at the end of the channel; which different than in the case of grid N3 where x_{peak} appears just after the mid-channel. The affects of the grid thickness in the direction of the mean flow needs to be more investigated. Experiments on the effects of the fractal square grids generated-turbulence on the performance of hydrokinetic turbines are going to be conducted.

Chapter 4

4 An experimental study of fractal generated-turbulence influence on horizontal axis hydrokinetic turbine performance

Authors: Altayeb Mahfouth[1], Curran Crawford[1]

[1] Dept. of Mechanical Engineering, University of Victoria, BC

To be submitted

4.1 Abstract

This work presents a study into the performance characteristics of a horizontal axis hydrokinetic turbine using a recirculating water tunnel, using a fractal space-filling square grid to generate upstream turbulence and a small scale axial rotor rig. The rotor rig was developed specifically for small-scale testing Reynolds numbers and these tests was run in speed-control mode. The present work aimed to study the rotor performance in the wake of a fractal grid generated turbulence for different operational conditions, to compare the performance of the model in turbulent (turbulence intensity TI around 7.4%) and smooth flow (TI less than 0.5%) conditions. The fractal square grid was installed in the entrance of the water tunnel. The study was carried out with three different nominal inflow speeds: 0.99, 1.37 and 1.57 m/s. The velocity field upstream of the turbine was documented using Particle Image Velocimetry (PIV); 3000 images were obtained at each tip speed ratio to achieve statistical convergence. It was found that by using fractal grid generated turbulence, the efficiency of the turbine at the three different inflow speeds was decreased quite significantly, with peak C_p values decreased on the order of 30%. This result has important

implications for water tunnel testing of rotors that is typically done in low turbulence tunnels, whereas real-world operating conditions have turbulence intensities on the order of TI=6-20%.

Key Words: Wind/Hydrokinetic turbine rotor; Fractal square grid; Turbulence Intensity, Power coefficient.

4.2 Introduction

River and tidal currents represent a large source of energy which can be extracted with very low lifecycle carbon emissions by deploying hydrokinetic turbines (HTs). One of the first requirements for the development of any reliable hydrokinetic turbine business case is the ability to predict the performance of the rotors of the HTs. Since the early 2000s, noticeable improvements have been achieved in the design of hydrokinetic turbines. Even though these improvements have led to a number of increasingly large deployments of HTs around the globe, there is still much research to be done to provide a deeper understanding of the hydrodynamic behavior of these turbines. In general, hydrokinetic turbines and wind turbines are very similar in terms of understanding their hydrodynamic/aerodynamic characteristics, but the ambiance conditions in deploying both of them (air and water) are different and with vastly different properties (e.g. density, acoustic propagation, cavitation issues) and even site to site variations of environmental conditions. Therefore, HTs require detailed investigations in order to reliably exploit the full potential of marine and river currents. HTs deployed in rivers and the ocean generate energy from a spectrum of unavoidable operating conditions as a result of flow turbulence, the influence of large-scale eddies and changing flow speed with depth. Thus, studying the performance of HTs in prescribed turbulent inflow will help improve device design and prediction of the output energy of HTs.

This study was aimed at providing insight into the effect of turbulence intensity on the performance of a model of hydrokinetic turbine. Commentary on unsteady inflow effects on rotor performance are given in sections 4.2 and 4.3. Description of the experimental apparatus including experimental facility, the model scale hydrokinetic turbine and parameters of the fractal grid is presented in section 4.4. In section 4.5, the experimental procedures and technique used in this work is introduced. As this rig can be used for a range of rotor sizes, experimental results may be obtained in high turbulence flow over a range of designs using the demonstrated experimental procedures presented in section 4.5. Uncertainty analysis of the data is reported in section 4.6. The results

from this study, presented in section 4.7, demonstrate a large influence of turbulence on rotor performance, indicating the important of rotor testing in turbulent conditions, rather than the very low turbulence inflow conditions typically used in lab scale testing campaigns. Finally, section 4.8 has a conclusion summarizing and comparing the results obtained from the two different flow conditions.

4.3 Non-uniform and unsteady inflow effects

Uniform inflow is almost never achieved in the real world, as it implies flow velocity and depth remain constant whereas naturally occurring or man-made channels have changes in cross-section from point to point. Uniform flow can occur only in a channel of constant cross-section, roughness, and slope in the flow direction. Non-uniform inflow is therefore the norm, with velocity varying with depth and in many cases across the flow as well. Non-uniform flow can occur in both man-made and natural channel, rivers, with variable geometrical properties and ocean tidal, ocean current [Kaji, (2013); Ardhuin and Jenkins, (2006); Franca and Brocchini, (2015)]. In the real world, hydrokinetic turbines are installed in non-uniform and also unsteady flow with high turbulence intensities (turbulent flow across a range of eddy length-scales from macro to micro). The turbulence intensity is the ratio of the root-mean-square of the turbulent velocity fluctuations to the magnitude of the flow velocity ($TI = \frac{\sigma_u}{\bar{u}}$); is often referred to as turbulence level. It helps to understand the nature of turbulence in the turbulence flow such as rivers for which is considered as a main aspect in terms of designing hydrokinetic turbines. Typically, three cases of turbulence were introduced based on the turbulence intensity level [Soltani, et al., (2011); Ghorbanian, et al., (2011); Strom and Papanicolaou, (2007); Balcer, (2005); George, et al., (1994); Nikora and Smart, (1997)]. A low-turbulence case occurring at controlled lab facilities and has turbulence intensity lower than 1% [Soltani, et al., (2011); Ghorbanian, et al., (2011)]. Turbulence intensity with range between 1%-5% is considered a medium-turbulence case; this occur in deep-wide rivers or low velocity shallow rivers and downstream of the turbulence generating regular grids [Strom and Papanicolaou, (2007); Balcer, (2005)]. 5%-20% is a high-turbulence case; like fast current rivers [George, et al., (1994); Nikora and Smart, (1997)].

A number of experimental studies have investigated turbulent effects on turbine performance [Batten, et al., (2006); Osalusi, et al., (2009); Colby, et al., (2010); Thomson, et al., (2012); Milne, et al., (2013); Mycek, et al., (2014)], but the majority of rotor performance studies are done in very low turbulence, uniform inflow conditions [Soltani, et al., (2011); Ghorbanian, et al., (2011)]. Mycek, et al., (2014) investigated the turbulence intensity effects on marine current turbines behavior in laboratory for two different turbulence intensities namely 3% and 15%. They reported that the turbulence intensity can strongly effect the wake of turbines. They also concluded that the performance of marine current turbines is slightly influenced by the ambient turbulence conditions. Batten, et al., 2006 stated that changing flow speed and direction of the flow with depth and the influences of the free surface have significant effects on the hydrodynamic design of marine current turbines. Unsteady flow can influence both fatigue loads on the turbine blades and also affect power production.

IT Power Group (ITP) installed the world's first commercial scale marine current turbine[10]. IT Power Group reported that turbulence has effects on the engineering design, analysis or operation of marine power installations[10]. Heavy loads can be imposed on horizontal wind turbine blades by turbulent inflows with large-scale eddies [Sutherland and Kelley, (1995), Osalusi, et al., (2009)]; similar impacts are to be expected for hydrokinetic turbine operation. Yokosi, (1967) investigated the turbulent flow in the Uji river and Sosui canal, stating that varying the width and depth along the river with the smallest eddies can cause the river flow to be unsteady and non-uniform. The river flows are dominated mainly by varying the small and larger length scales as well as turbulent intensities. The hydrodynamic properties of the rotor blade sections, from which the energy of the rotor is determined, can be effected by the smaller scale non-uniform inflow. Moreover, the large-scale turbulence contributes to dynamic loads on the rotor blades and has effects on the fatigue life of the rotor blades.

[10] "IT Power Group" [Online]. Available: http://www.itpowergroup.com/ [Accessed: 20-Oct-2016].

Unsteady inflow is correlated with turbine performance, structural fatigue and the wakes of individual turbines [Kelley, et al., (2005); Frandsen, (2007); Thomson, et al., (2012)]. Unsteady inflow may cause dynamic stall on the turbine's blades. This dynamic stall may occur on the blade as a result of a locally rapid change in the relative velocity over the blade. This rapid change is introduced by eddies that are carried along with the mean flow. Fluctuating aero/hydrodynamic loads can be created by dynamic stall on the blades, which are different than the inherent dynamic behavior of the turbine [Clark, et al., (2015)]. [Talavera and Shu, (2015)] reported that the turbulence intensity of the inflow has high influence on the efficiency of turbines.

Non-uniform and unsteady inflow in rivers and oceans causes cyclic loads (that are imposed upon the turbine) that continually pose a threat of fatigue damage to the marine current turbines [Osalusi, (2009)]. The use of wind/water tunnel tests of hydrokinetic turbines is typically faced with limitations due to a lack of compatibility with respect to real wind/water flows [Iungo, et al., (2012)]. This might cause differences in the boundary layer flows over the suction side of the blades created by the lower Reynolds number at model scale, which leads to laminar separation bubbles on the blades [Selig and McGranahan, (2004)]. These bubbles cause an adverse pressure gradient which results in separation of the laminar flow before it can transition to turbulence and re-attach. This makes the boundary layer rather thick leading to increase in pressure drag and loss in aerodynamic lift, performance [Singh and Ahmed, (2012)].

Previous experiments have been conducted in low turbulent intensity water/wind tunnels to investigate turbines performance [Bahaj, et al., (2007); Whelan, et al., (2009); Harrison, et al., (2010); Myers and Bahaj, (2010); McTavish, et al., (2013); Malki, et al., (2013); MAVI, et al., (2014); Franchini, et al, (2016)]. Conducting experiments in low TI water/wind tunnels does not adequately simulate real-world flow conditions, where turbulent flow has high turbulence intensity reaches to 20% [Osalusi, et al., (2009); Colby, et al., (2010); Thomson, et al., (2012); Milne, et al., (2013)]. There is therefore a pressing need to conduct such experiments in laboratory water/wind tunnels that have high TI. Thus, in this work, a field study has been conducted in the Winnipeg river in order to characterize real-world turbulent intensity in rivers (assumed of similar magnitude to in the ocean at potential hydrokinetic sites) and the variation of TI with respect to depth and its values in the boundary layer. Based on the field data, appropriate and controlled TI was generated in the water tunnel. Finally, a study of the effects of turbulence on the performance characteristics

of a model of a hydrokinetic turbine in three different inflow speeds was conducted. This investigation can increase our fundamental understanding of operating hydrokinetic turbines in real operating conditions. These field and experimental data can be also beneficial for CFD models by providing validation data for flow simulations.

4.4 Experimental apparatus.

4.4.1 Model scale hydrokinetic turbine

A wide range of model rotors can be test using the rig developed in the SSDL. The rig was designed to be suitable for the UVic water tunnel which has a cross section of 0.45 x 0.45 m^2. It can be operated with a closed lid up to maximum flow velocity 2 m/s. This model was designed first by Lartiga & Crawford, (2009), then was further developed by Franchini & Crawford, (2015). The model's components are shown in Figure 4.1. The model consists mainly of two sections. One is immersed in the channel and the second is mounted on the acrylic lid, which is used to eliminate any free surface effect, located on top of the section test. The immersed section is comprised of a three-bladed rotor (1), a main horizontal shaft with its housing tube (2), support tube with fairings that reduce drag and disturbance of the flow (3), a belt (6), and a hub (7) which was designed in the way that can be used for different rotor diameters. The second part has the instrument structure which consist of a AKM23D servomotor with its own horizontal shaft (4), and a torque cell Novatech F 326-Z (5). The second part also has a yaw system which consists of two plates attached to the hatch that can rotate and adjust the position of the submersed structure and yaw the rotor accurately. The minimum expected torque for the experiment is about 0.01 Nm, and the torque cell Novatech F 326-Z has the capability to measure small value such as the minimum expected torque; it has also the ability to read torques ranging -1 Nm to +1 Nm, and the DAQ electronics components can resolve a smallest signal of 60 μV [Lartiga & Crawford, (2009)].

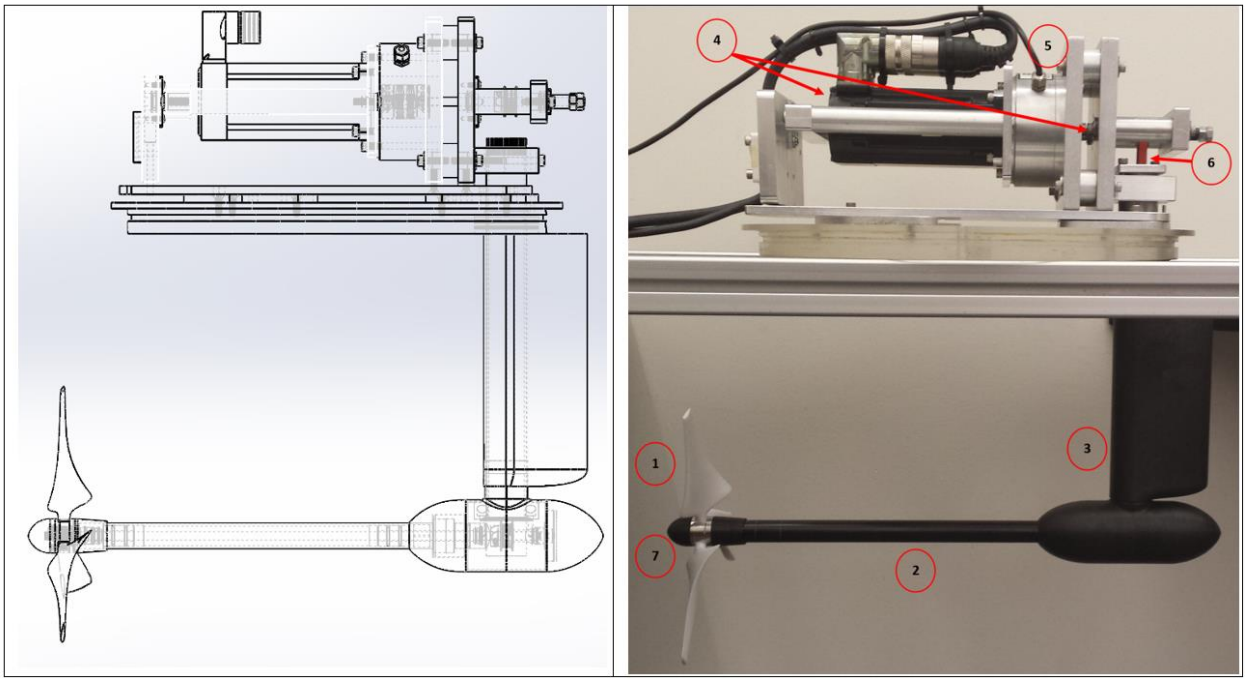

Figure 4-1:The rotor rig components

The two sections are connected together by the support tube. An external fairing is added around the support tube to increase streamlining and reduce drag. The servomotor is connected to the torque cell which is used to measure the reaction torque, then to the belt via the motor horizontal shaft. The belt carries the motion from the servomotor to the rotor via the main horizontal shaft (more detailed information about the model's components can be found in [Lartiga, (2012)].

The DAQ system consists of the load cell to measure the torque and NI CompactRio hardware. Figure 4.2 shows the data acquisition system (NI CompactRio package) used to control the servomotor through a LabView graphical user interface. The NI CompactRio is a real-time acquisition system measures and stores all the acquired information. The LabView graphical user interface enables the user to control the servo motor velocity and direction via the Kollmorgen AKD servo drive. The data acquired also can be displayed by the graphical user interface.

In order to study the performance of the turbine, it was important to control the rotational speed and position of the rotor accurately. Thus, the turbine was connected with a servomotor which allow precise positioning and speed control without the use of external encoder or feedback sensors. The AKM23D servomotor and the Kollmorgen AKD servo drive were chosen as the drive

system. Consequently the rotor azimuth angle can be coordinated with the PIV equipment to synchronize image acquisition.

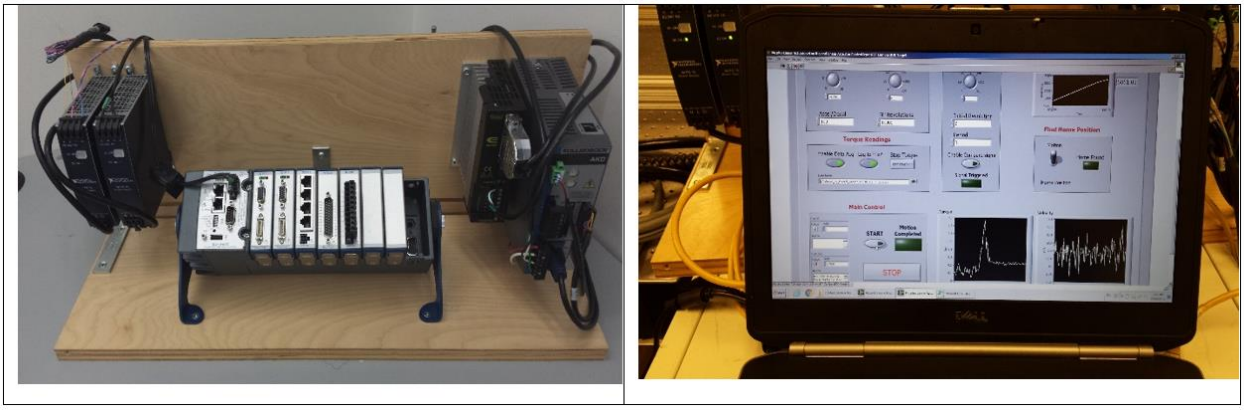

Figure 4-2:The data acquisition system

The same rotor blades which have been tested at the SSDL by Franchini, (2015) in steady conditions were selected for this work: an SD8020 scaled to 15% thickness, Figure 4.3. Franchini, (2015) reported that this hydrofoil showed good low Re performance. The original SD8020 airfoil, with a thickness of 10%, was tested by The University of Illinois at Urbana-Champaign (UIUC) Low-Speed Airfoil Test program and shown to have acceptable low Reynolds performance[11]. Franchini imposed a minimum 15% thickness to this hydrofoil to prevent bending and structural problems. The blade sets tested with this rotor rig by Lartiga (2009) were thinner and there were bending issues with them, which led to unsuccessful results.

A three-dimensional solid model of the hydrofoil was designed using Solidworks software, Figure 4.4. Then it is exported to a Fused Deposition Modeling (FDM) machine software in stereolithography (STL) format. Once the STL file has been exported, the FDM software then horizontally sliced it into many thin sections. Based on these sections the FDM process generates 2D contours paths which will resemble the hydrofoil part. The FDM machine builds the model layer-by-layer from the bottom by heating and extruding polycarbonate filament.

The blades needed to be printed with a rough surface finish to improve low Re performance based on previous testing experience, so a T12 tip combined with the polycarbonate material were used

[11] "U. of Illinois at Urbana-Champaign" [Online]. Available: http://m-selig.ae.illinois.edu/pd.html [Accessed: 25-Oct-2016].

in the FDM machine. The blades were 3D printed with maximum 5.3 cm chord and total length of 10 cm [Franchini, (2015)]. The large tip was intentionally used to provide a naturally rougher surface which has been found in previous experiments to improve low Re performance relative to smooth surfaced foils.

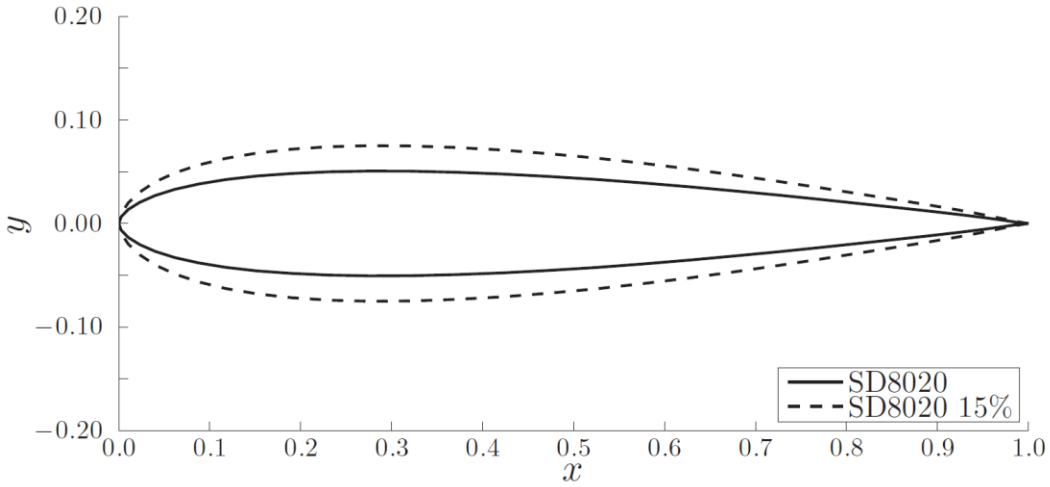

Figure 4-3:SD8020 hydrofoil

4.4.2 A Space-filling fractal square grid

Fractal grids have been used to generate controllable turbulence in water and wind tunnels [Hurst and Vassilicos, (2007); Seoud and Vassilicos, (2007)]. Fractal grids are rigid structures with constant solidity that result in turbulent flows with specific patterns and statistics corresponding to the grid geometry. Various patterns for fractal grids can be characterized as: I pattern, cross pattern and square pattern. The square pattern is the one used to generate turbulence in the current study. Space-filling fractal square grids with relatively low solidity have the ability to generate turbulence with high Reynolds numbers compared with turbulence generated by regular grids at the same flow speed [Seoud and Vassilicos, (2007)]. A schematic of a square type fractal grid is shown in Figure 4.5. Fractal grid's parameters are contained in table 4.1. As can be seen in the Figure, the grid has different bars with different sizes. Since the grid has different bars, it generates turbulence by creating different sizes of vortices with corresponding levels of interaction [Mazellier and Vassilicos (2010); Laizet and Vassilicos, (2011)]. The grid can generate turbulence with a build-up production region and a decay region. The turbulence is built up in the decay region till it reaches a peak turbulence intensity peak at a distance x_{peak} downstream of the grid. Downstream

of the TI peak, the turbulence decays and the TI reduces in the decay region. The turbulence in the near region (production region) is anisotropic and non-homogenous, while that in the downstream region (decay region) is isotropic and homogenous. The rotor is deployed in the decay region.

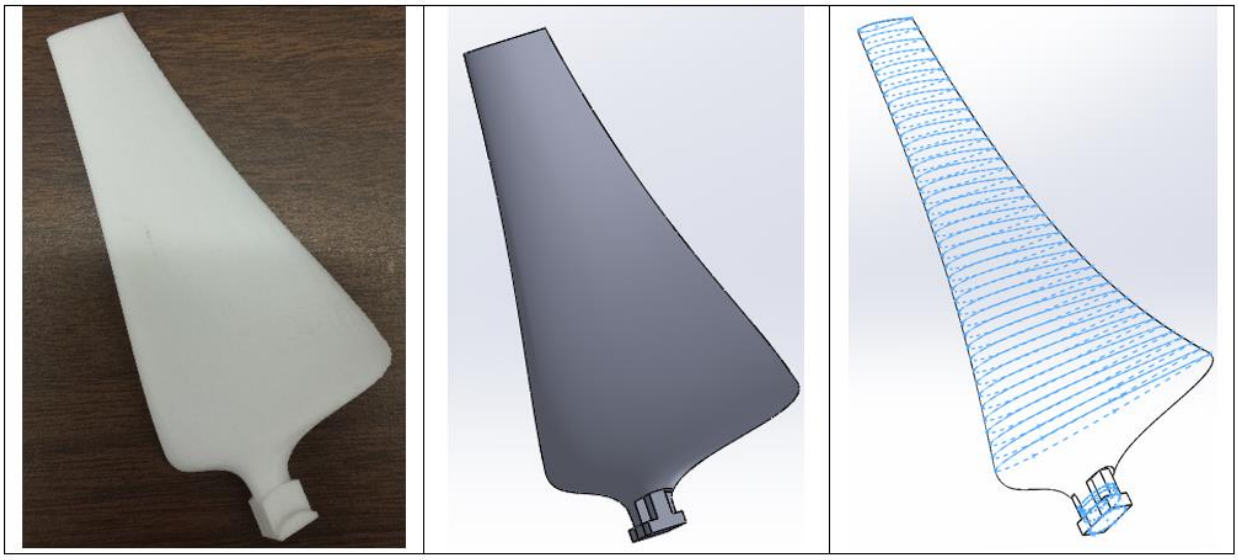

Figure 4-4:The tested blade design

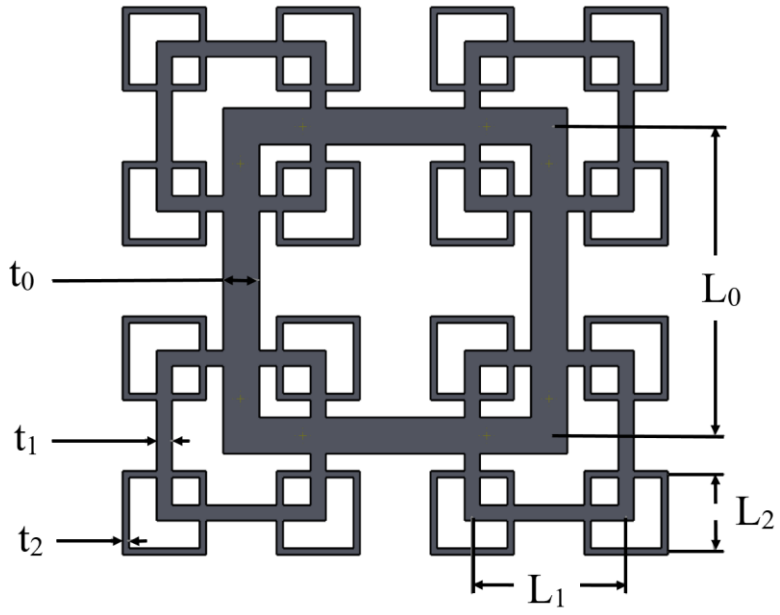

Figure 4-5: A schematic of a square type fractal grid

Table 4.1:Parameters of the space-filling square grid

N	D_f	σ(%)	t_r	R_t	R_L	L_0(mm)	L_1(mm)	L2(mm)	t_0(mm)	t_1(mm)	t_2(mm)
3	2	27	5.5	0.425	0.5	212.09	106	53.03	25	10.6	4.5

where,

- N: is the number of fractal iterations.
- D_f: is the scaling exponent (known as a fractal dimension) that characterizes the fractal perimeter
- σ : is the blockage ration which has been defined by Hurst & Vassilicos as the ration between the total area of the grid to the total size of the grid.
- t_r: is the thickness ratio; it is defined as the ratio between the thickness of the largest bar in the grid to the thickness of the smallest one.
- $L_0 - L_2$: are the lengths of the grid's bars at each scale iteration j (in the plane of the pattern, normal to the mean flow).
- $t_0 - t_2$: are the thickness of the grid's bars at each scale iteration j (in the plane of the pattern, normal to the mean flow).
- R_L, R_t: are the ratios of the bars' length and thickness between each iteration; these scaling factors are independent of j (the scale-iteration) and are smaller than or equal than 1/2 and 1 respectively.

4.5 Experimental method

The experiments were conducted in the University of Victoria water tunnel. In order to investigate the performance of the turbine some parameters need to be introduced such as the Tip Speed Ratio (TSR) which is defined as the ratio between the tangential speed of the tip of the blade and the flow velocity:

$$TSR\ (\lambda) = \frac{\omega R}{U} \qquad \textbf{(4-1)}$$

where ω is the rotational speed of the rotor, R is the blade tip radius measured from the center of the rotor to the tip of the blade (R= 11.27 cm), and U is the nominal average inflow velocity which was measured at 2 rotor radius's distance upstream the turbine (2R). The reaction torque T_{rotor} of the servomotor driving the rotor is measured allowing the mechanical power output estimation P_{out} calculated as:

$$P_{out} = T_{rotor}\omega \quad \textbf{(4-2)}$$

Once the power output is found experimentally for TSRs ranging from 1-6, the performance of the turbine was computed using the power coefficient C_p defined as:

$$C_p = \frac{P_{out}}{\frac{1}{2}\rho U^2 A} \quad \textbf{(4-3)}$$

where ρ is the fluid density, A is the rotor area (the area swept by the blades).

The fractal square grid was installed at distance of 21.18 cm downstream from the entrance of the water tunnel, Figure 4.6. In the low TI case, the model was placed downstream (at 98.5 cm) in order to have a longer tunnel section to fully PIV the wake in that case. However, this was not possible with the fractal grid, whereas, in the production region downstream of the grid, the turbulence is nonhomogeneous and anisotropic; therefore, the turbine should not be installed in this region. On the other hand, in the decay region the turbulence is isotropic and homogeneous, representative of real flows and therefore an ideal installation location for the turbine. Thus, the hydrokinetic model was placed more downstream of the grid at 1.8 m as shown in Figures 4.6; 4.7. The rotor has a radius of 11.27 cm resulting in a blockage ratio (defined as the ratio between the rotor blade' swept area and water tunnel's cross sectional area) of 19.7%. Although the blockage was fairly high, it was consistent for turbulent and non-turbulent conditions and could be corrected to unbounded conditions if required [Bahaj, et al., (2007)].

Once the water tunnel is filled and pressurized (i.e. water level in the tunnel upstream settling chamber higher than the top of the working section of the tunnel), the experiments were run at 3 pump motor frequencies: 25, 35 and 40 Hz, corresponding roughly to inflow speeds of 0.99 m/s, 1.37 m/s and 1.57 m/s. The water tunnel is pressurized using the acrylic lids to prevent any wave formation and also air bubbles are removed. The air-bubbles have to be removed before running the experiments because they are detrimental to the collection of PIV data. For all flow speeds, the rotor yaw angle (γ) and blade pitch angle (β) were set to be $\gamma = 0^o$ and $\beta = 4.1^o$respectively. Note that as the inflow velocity increased as the water level decreased; it was therefore important to pay attention to the water level while increasing the flow velocity to keep the section pressurized and prevent air entering the tunnel. A rig shaft friction test was also run to quantify the torque due to frictional forces (caused by the mechanical components of the rig such as bearing, seals, belt, etc.) with the rig wet. These measurements were obtained over a range of shaft speeds (with rotor

blades removed) and the torque measurements from the frictional forces subtracted from the torques measured during flow testing.

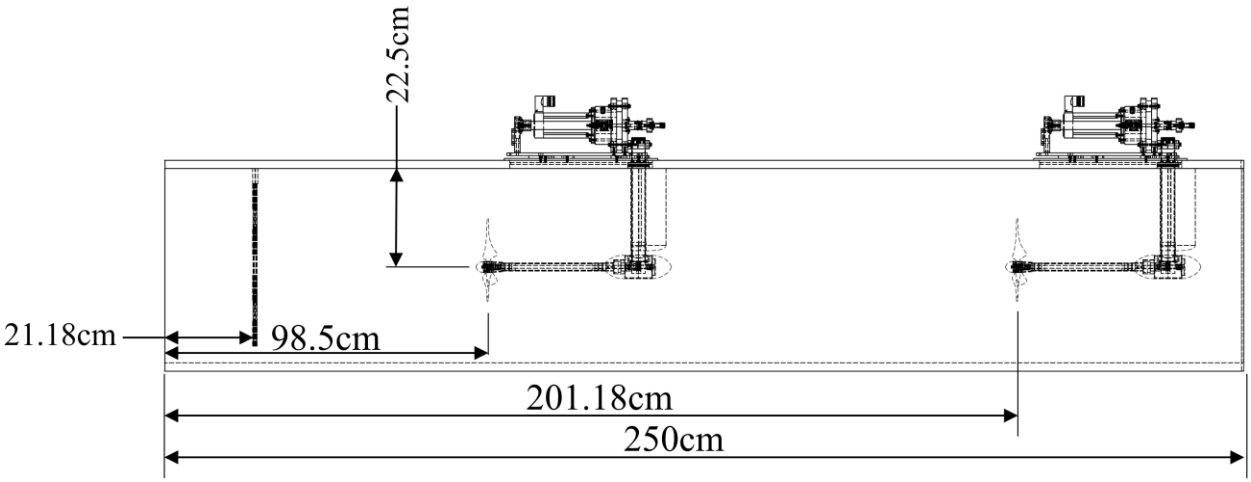

Figure 4-6: A sketch shows where the rotor rig and the grid are placed inside the flume tank

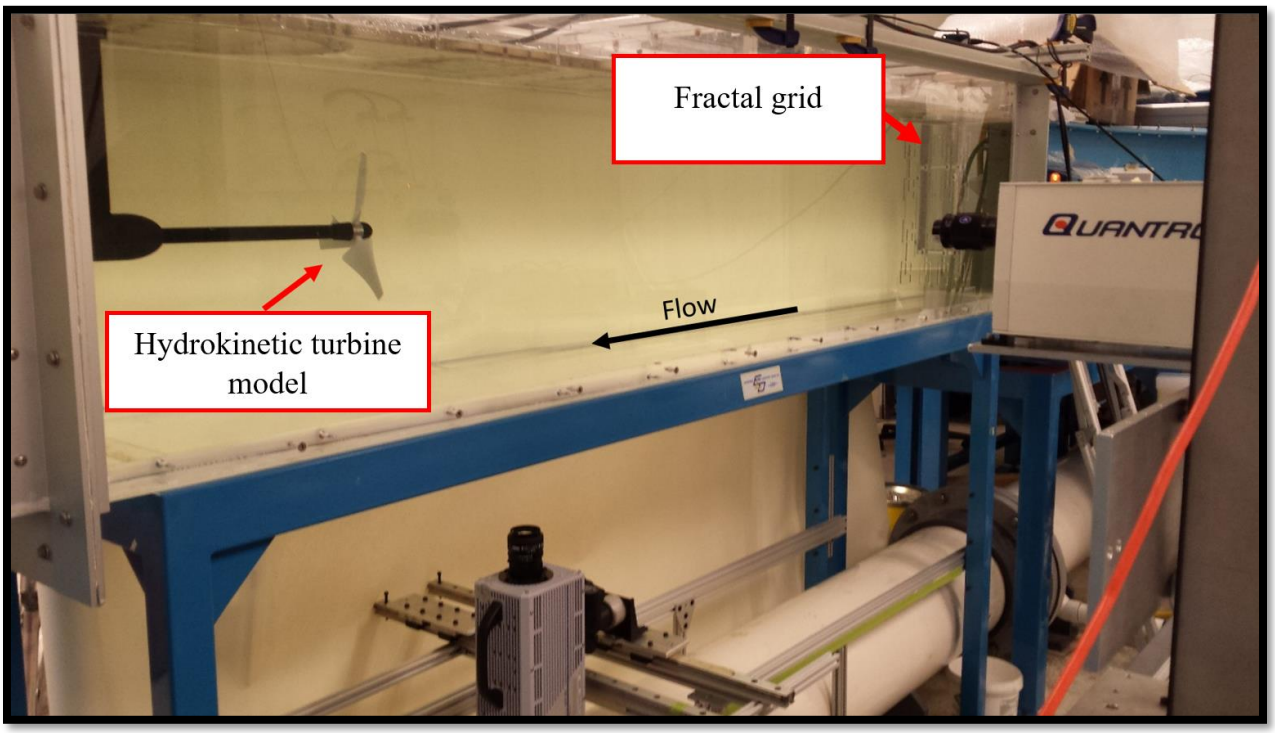

Figure 4-7:Turbine installed downstream of the grid in the water tunnel, with PIV equipment in-place to measure inflow turbulence at the rotor

The flow velocity was measured using PIV at 2R upstream the turbine. The 2D PIV is synchronized with a CCD camera (LA-Vision VC-Imager Intense) to capture the 2D flow field in a horizontal laser sheet. A lens with a 50 mm focal length was used with the camera to record the

images. The images were taken with 1024X1024 pixel resolution. 3000 images were taken using frame rate of 25 Hz to ensure an acceptable level of uncertainty in the calculated the mean velocity fields. In the low turbulence flow experiments (without the grid) the flow velocities corresponding to 25, 35 and 40 Hz are 0.88 m/s, 1.23 m/s, and 1.4 m/s respectively. After installing the grid, the three pump frequencies resulted in 0.99 m/s, 1.37 m/s, and 1.57 m/s at 2R upstream the rotor location. As mentioned before, the flow velocity in the water tunnel can be altered by changing the pump frequency via the Toshiba frequency controller. This frequency controller drives the pump shaft RPM, so that adjusting the pump shaft RPM does not necessary give the same flow velocity every time. The difference caused by the pump shaft RPM on the flow velocity is slight, however the grid is another factor causing the difference in the flow velocity as explained in §3.7.3. However, the flow is measured at $x > x_{peak}$ (x_{peak} is the location of the peak turbulent intensity downstream the grid); based on the fractal grid results the average flow reaches the normal velocity at around $x \approx x_{peak}$.

4.6 Error estimation

Uncertainty is an estimate, with some level of confidence, of error level in the measurements. In experimental work, there are two categories of uncertainties: systematic uncertainty (fixed error) and random uncertainty (precision errors) [Wheeler and Ganji, (2004)]. The systematic uncertainty mainly result from the measurement system which includes, in this work, the F326-Z torque cell and the NI 9237 module for torque measurement. The repeatability, calibration, non-linearity and hysteresis errors of a measuring system lead to systematic uncertainty. These error sources are also known as elemental error sources. The random uncertainty is caused by a lack of repeatability in the output of the measuring system from an experiment with inherent variability [Wheeler and Ganji, (2004)]. Combining the systematic (SYS_x) and random (RAN_x) uncertainties yields the total uncertainty (UNC_x) for the x measurements:

$$UNC_x = \sqrt{SYS_x^2 + RAN_x^2} \qquad \textbf{(4-4)}$$

The random uncertainty (RAN_x) can be determined by calculating the standard deviation of the obtained data. Thus, the random uncertainty of the measurement of the torque can be obtained from:

$$RAN_T = \pm t \frac{S_T}{\sqrt{M}} \quad \textit{(4-5)}$$

where S_T is the standard deviation of the torque samples, M is the number of samples, and t is equal to 3.182 for a confidence level of 95% with υ = 4 degrees of freedom (the number of independent measurements minus the minimum number of measurements that are theoretically necessary to estimate a statistical parameter [Wheeler and Ganji, (2004)]).

The systematic uncertainty of the measurement system with regard to the variable T (Nm) is done by combining elemental uncertainties of the system components. The systematic uncertainty is calculated based on the technical specifications provided by the vendor. Table 4.2 contains the uncertainty for each instrument.

Table 4.2: Systematic uncertainties of the measuring system

Instrument	Sources of Elemental Error	Uncertainty
The F326-Z torque cell	Non-linearity	±0.1%
	Repeatability	±0.05%
	Hysteresis	±0.40%
The NI 9237 module	Calibrated typical (25 ºC, ±5 ºC)	0.05%
	Calibrated maximum (-40 ºC to 70 ºC)	0.20%
Both	Total $SYS_x = \sqrt{0.1^2 + 0.05^2 + 0.40^2 + 0.20^2}$	$SYS_x = 0.46\%$

Then, the total uncertainty is computed (for the two cases) by combining both the systematic and random uncertainties using the square root of the sum of the squares (RSS), as in Eq. (4.4) following Wheeler and Ganji's, (2004) Experimental Uncertainty Analysis Procedure. The uncertainty in the PIV measurements (Velocity measurements) is very small, besides it is averaged over many windows, this makes it to be neglected. As will become evident in the following section in the errors bars of Figure 4.8, the data obtained in smooth flow (TI =0.5%) is more precisely know than in turbulent flow. The uncertainty varies between 0.081% to 1.3% throughout the three flow speeds. Therefore, it can be demonstrated that in the smooth flow the overall uncertainty of the measurements is very slightly changed. The uncertainty in the data when the flow has a turbulent intensity of 7.4%, is estimated to be varying between 0.12% to 2%, as can be seen in the Figure. This uncertainty is mainly contributed from the random uncertainty which increases with increasing TI. It was noticed that the random component was an order of magnitude higher than the systematic component and also increases with inflow velocity.

4.7 The performance of the rotor

Torque measurements were obtained to study the hydrokinetic turbine's efficiency and determine the optimal tip speed ratio (point of maximum C_p). Low and high turbulence cases were studied, with the rotor located at the lateral/vertical center of the tunnel cross-section to minimize wall effects on the measurements. The rotor performance was obtained at three different inflow speeds for smooth flow (TI = 0.5%) and with fractal grid generated turbulent flow (TI = 7.4%). Figure 4.8 shows the results for the two different turbulence intensities. It can be observed that the rotor exhibits very good performance for the three velocities at the lower turbulent intensity, with an optimal TSR of around 3.5. The maximum C_p value increases slightly with flow speed, as would be expected from increasing blade-local Reynolds number. Moreover, the power coefficient for both cases has greatest values at TSRs of 3-4. The rotor was designed specifically for this model scale, using low Reynolds hydrofoils and a chord distribution larger than a scaled down full size device to minimize low Reynolds number impacts on performance. As mentioned, the blades were also printed intentionally rough to promote transition and flow attachment to avoid premature stall.

The rotor clearly experienced decreased performance in flows with high turbulence intensity, with C_p not exceeded 0.35 across the range of flow speeds studied. For both TIs however, the C_p curve follows a similar trend. The typical stall-from below the optimal TSR and drag dominated fall-off in C_p above $C_{p_{max}}$ are both evident in the results. It should also be noted that none of the results were corrected to free-stream conditions to account for blockage, and the maximum C_p near 0.5 for the highest inflow speed is therefore larger than would be expected in unbounded conditions. However, the results here are self-consistent, in that all tests were carried out at the same blockage ratio.

The issue of turbulent eddy size is evidently quite important, but is not well discussed in the literature. In terms of field measurements, [Birjandi, (2012)] conducted ADV measurements at 2R upstream of a 25-KW vertical axis hydrokinetic turbine (R is the turbine's radius equal to 1.7 m) in a river with a high turbulence intensity. Measurements were taken both with the rotor parked and operating. The autocorrelation function was computed over a range of delay times τ as $\rho_{uu} = \frac{\overline{u_1(t)u_1(t+\tau)}}{\langle u_1^2 \rangle}$, where u is the fluctuating streamwise velocity component recorded at a point. The integral time scale is a measure of how long turbulent fluctuations remain correlated. The integral

length scale represents a measure of the longest connection (or correlation distance) between the velocities at a single or fixed point but different times, and thereby a typical size metric of the turbulent eddies. The integral time scale is computed by integrating the autocorrelation function from t=0 to the first instance of ρ_{ii}=0 as $T_i = \int_{t=0}^{t(\rho_{ii}(t)=0)} \rho_{ii}(t)dt$. Birjandi examined two locations, one close to an upstream pier and another away from the pier and found that the integral length scale was dramatically shorter when the turbine was operating, ranging from 6.41 m (near pier) and 0.47 m (away from the pier) but reduced to 0.11 m with the turbine operating in both locations. It was reasoned that the operating turbine retarded the flow, which in turn created a shear layer that through the energy cascade transformed mean flow and large-scale turbulent structures into much smaller eddies. Birjandi reported that eddies upstream of the operating turbine had a size around 1.1 times the turbine's chord. Unfortunately, a simple dump load was used on the turbine's output, so impacts on the C_p were unavailable.

Mycek [Mycek 2014] reported a series of turbine tests in a large recirculating water tunnel (0.7 m diameter turbine, 18 m test section 4 m width, 2m height), operating the turbine with standard flow conditioning honeycombs in-place and removed. With honeycombs the flow TI was approximately 3%, and without 15%. In the discussion, it was reported that the mean C_p and Ct curves did not vary much with TI level, even though the standard deviation of C_p and Ct did increase substantially at 15% TI. However, the results were reported at 4 flow speeds from 0.4 m/s to 1.2 m/s, and the C_p curves in particular at a given TI level exhibited significant variation. Examining the results it is difficult to discern a concrete conclusion as to the effect on mean C_p with TI, given the overwhelming variation with Re (the blade local Re were in the range 1.4e10^5 to 4.2e10^5, right in the typical laminar-turbulent transition regime of typical hydrofoils). They also do not directly address the issue of length scale of turbulence in their paper, only TI level, although there is an FFT of the inflow velocities given in the appendix. From that plot, it appears in the 15% TI case there is significant energy around 0.25 Hz, which in the 0.83 m/s average flow velocity corresponds to a wave number of 1.89 m^-1 and a typical length scale of 0.53 m. That is on the order of the rotor diameter, and it is therefore likely the turbulent structures in the flow interacted very differently with the blade-local sections that smaller scale turbulence on the order of blade chord would have (the latter apparently quite important, as discussed below). These large turbulent flow structures were likely the result of simply removing the flow-conditioning honeycomb (downstream of the driving pump turbines), compared to the controlled turbulence created in the current work by the fractal grid, or in true field conditions at the CHTTC.

To help understand what caused the lower C_p in the current work, the vorticity profile, typical instantaneous velocities, and averaged velocity profiles upstream of the rotor are presented in Figures 4.10, 4.11, and 4.12 for the two cases (case one: TI≈ 0.5 %, 35 Hz ≈1.23 m/s; case 2: TI =7.4%, 35 Hz ≈1.37 m/s; at 2R upstream for 7.4% TI). C_p was calculated from the using the appropriate averaged velocity in the two cases. It is clear that with the grid installed, the structure of the flow has vorticities that are an order magnitude of 10 times greater than those in the case of smooth flow. Their size is around 1.5 times the maximum chord (5.3 cm) on the blades.

To further investigate the turbulent length scales produced by the fractal grid, the autocorrelation function was computed as shown in figure 4.13 for points (exactly at the rotor's centerline, off-centerline, and in-between) 2R upstream of the turbine in the high TI case. Computing the integral length scale using the earlier formula yielded a size of 7.7 cm at the centerline, 8 cm in between, and 7.67 cm off-centerline.

These vorticities, shown in figure, can therefore be considered (with respect to the blade size) large-scale. It was reported that turbulent inflows with large-scale eddies can impose heavy loads horizontal turbine blades and contributes to dynamic loads on the rotor blades with large effects on the fatigue life of the rotor blades [Sutherland and Kelley, (1995); Osalusi, et al., (2009)]. Also, the smaller scale non-uniform inflow can affect the hydrodynamic properties of the rotor blade sections, from which the energy of the rotor is determined causing less power performance. These vorticities therefore will alter the relative angle and magnitude of the inflow seen by the rotor sections. Hence the lower C_p was likely caused by decreasing average lift and/or increased drag, ultimately reducing the average torque produced. The vorticities that are carried along with the mean flow would also cause a locally rapid change in the relative velocity over the blade, which can cause dynamic stall on the turbine's blades. This dynamic stall can create fluctuating hydrodynamic loads on the blades and also contribute to the degraded C_p . Also, from the averaged velocity profile Figure, one can see that there is a difference in the flow velocity between the centerline and extreme off-centerline in the turbulent flow. This means that the rotor experiences changing flow speeds radially, reducing their performance [Batten, et al., (2006)]. When the flow is unsteady, it makes the blade suffer unsteady flow condition which leads to stall condition. Battenm, et al., (2006) reported that unsteady flow can influence both fatigue loads on the turbine blades and also affect power production.

The TI seems to not have an influence on the standard deviation of c_p. The standard deviation of c_p for the tow TIs at the different inflow speeds is presented in figure 4.9. The TI seems to not have an influence on the standard deviation of c_p. It can be seen that the standard deviation is independent of TI and even inflow speeds. This is not the same with Mycek [Mycek 2014]; Mycek calculated the standard deviation values of both $C_p and\ C_t$ at two TIs (3% and 15%). He concluded that standard deviation values at 15% is higher than those at 3%; and it should always stay higher at higher TIs.

In the instantaneous velocity field for TI=7.4%, it can be seen that the flow is more turbulent and has high velocity zones and low velocity zones, which appear to correspond to the vorticities that are created by the grid elements. This cannot be seen in the case of TI=0.5%. This might again cause the flow to be not perpendicular to the rotor blade at all times, again contributing to lower C_p. These results generally confirm what has been mention in the literature, that turbulence has effects on the performance of the hydrokinetic turbines [Sutherland and Kelley, (1995); Selig and McGranahan, (2004); Kelley, et al., (2005); Ardhuin and Jenkins, (2006); Batten, et al., (2006); Frandsen, (2007); Osalusi, et al., (2009); Kaji, (2013); Thomson, et al., (2012); Singh and Ahmed, (2012); Franca and Brocchini, (2015); Clark, et al., (2015); Talavera and Shu, (2015)] but clearly there is much more work to be done in terms of detailed characterization and reproduction of proper length scales and other descriptive characteristics beyond simple TI levels.

(a)

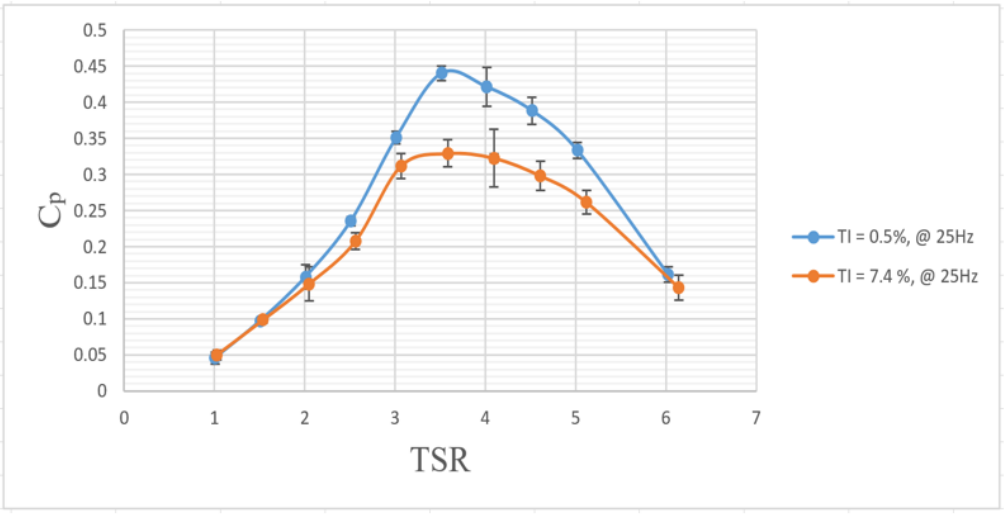

(b)

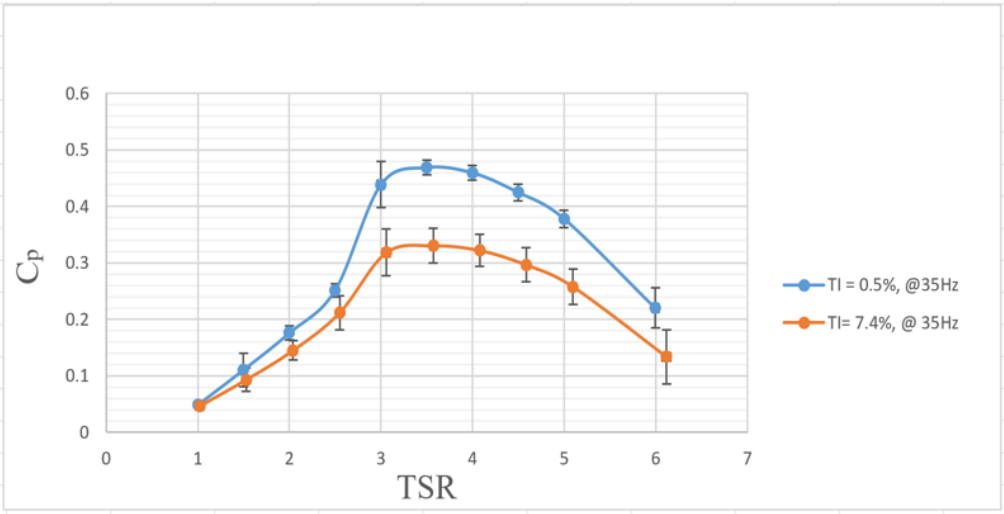

(c)

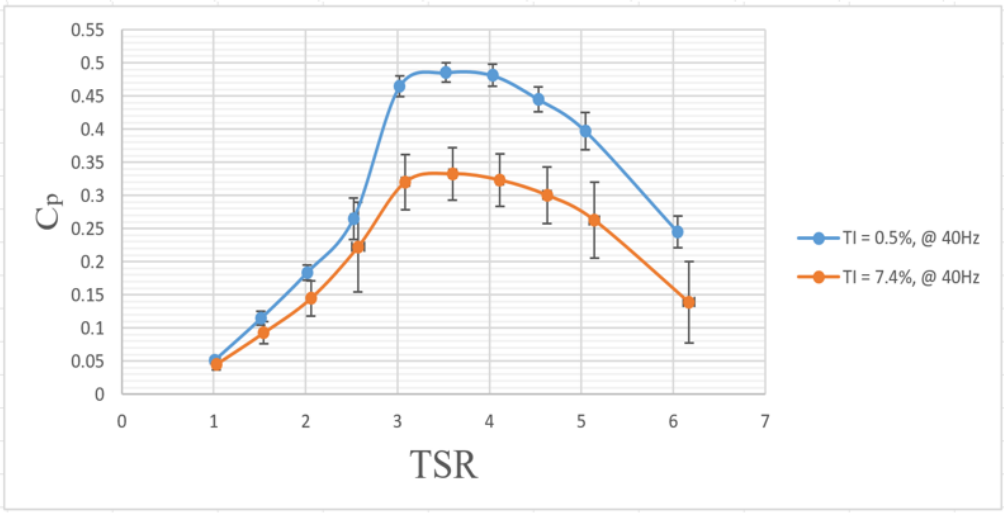

Figure 4-8:A comparison between the power coefficient of the rotor in smooth flow TI≈ 0.5 %; [(a) 25 Hz ≈ 0.88 m/s, (b) 35 Hz ≈1.23 m/s, (c) 40 Hz ≈1.4 m/s.] and in turbulence flow TI =7.4%; [(a) 25 Hz ≈ 0.99 m/s, (b) 35 Hz ≈1.37 m/s, (c) 40 Hz ≈1.57 m/s.]

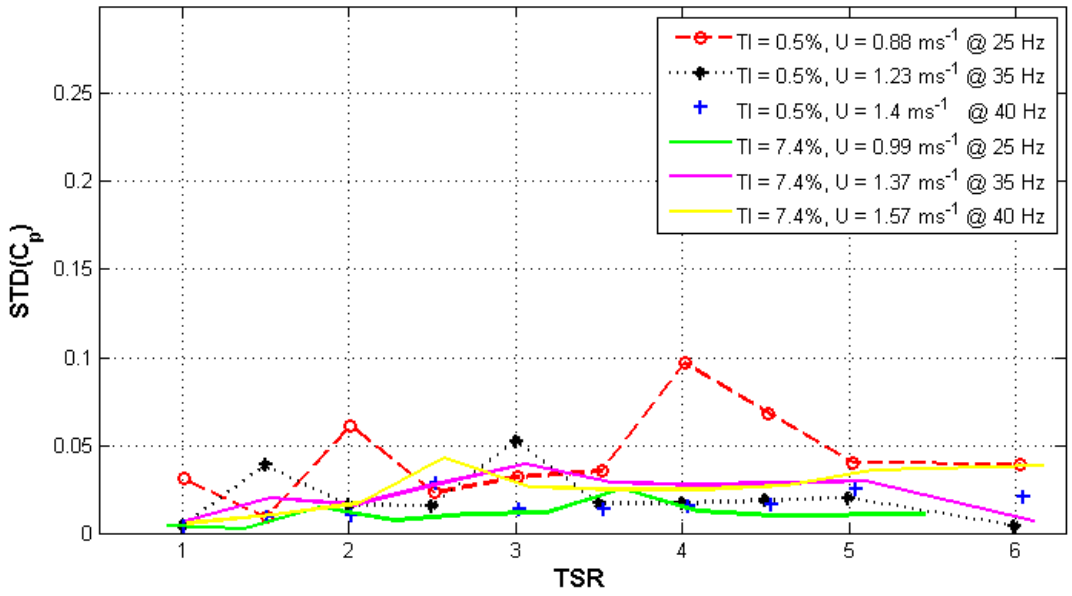

Figure 4-9: Standard deviation of the power c_p for TI=0.5% and TI=7.4% on the centerline, 2R upstream the rotor

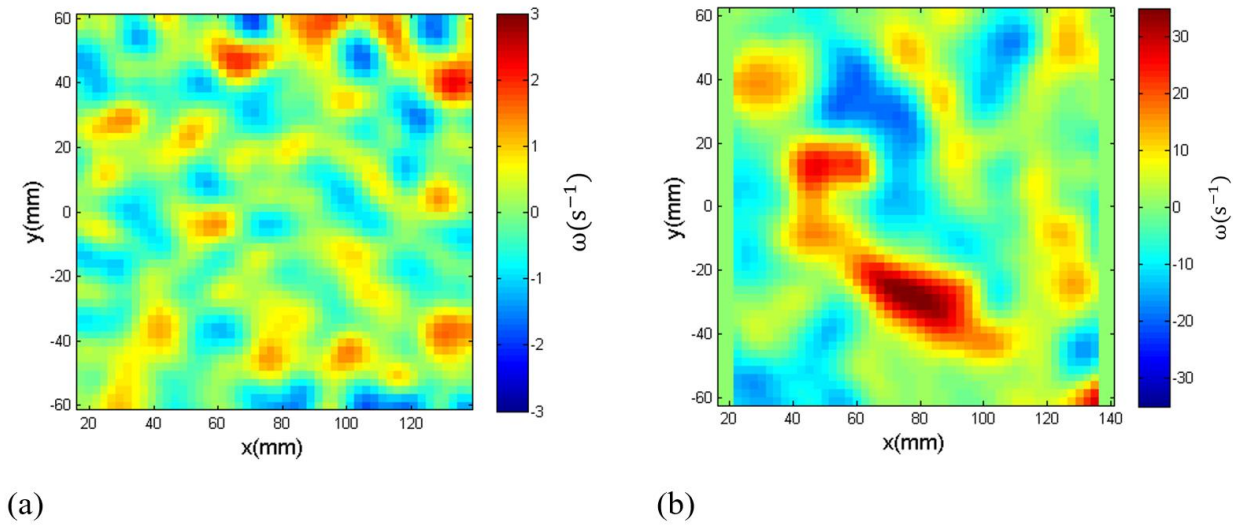

Figure 4-10: Vorticity profile upstream of the rotor, (a) without the grid, TI≈ 0.5 %; 35 Hz ≈1.23 m/s, (b) with the grid, TI =7.4%; 35 Hz ≈1.37 m/s

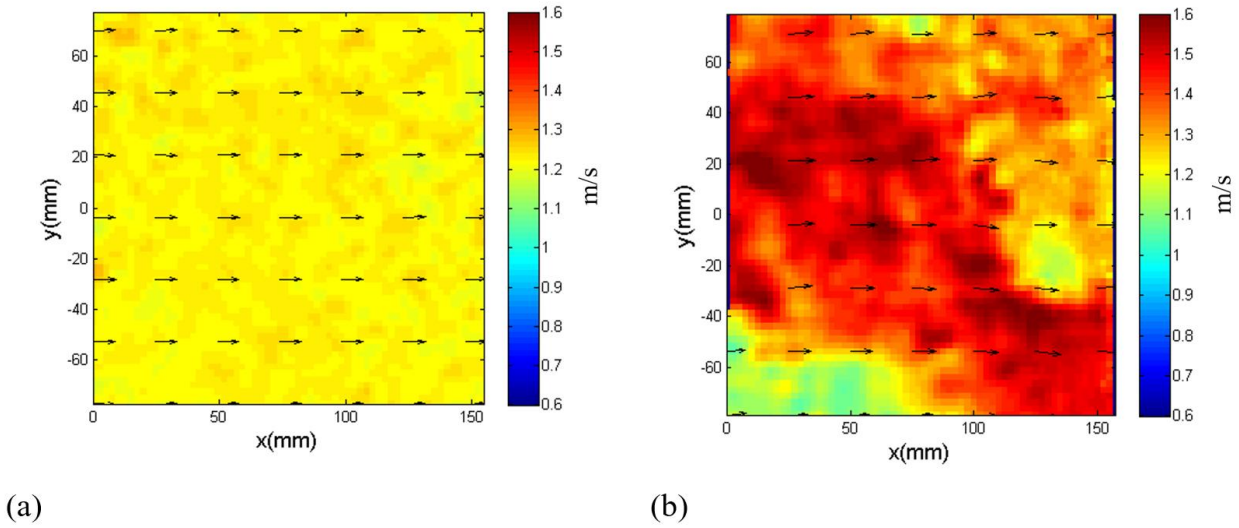

Figure 4-11: Typical instantaneous velocity upstream of the rotor, (a) without the grid, TI≈ 0.5 %; 35 Hz ≈1.23 m/s, (b) with the grid, TI =7.4%; 35 Hz ≈1.37 m/s

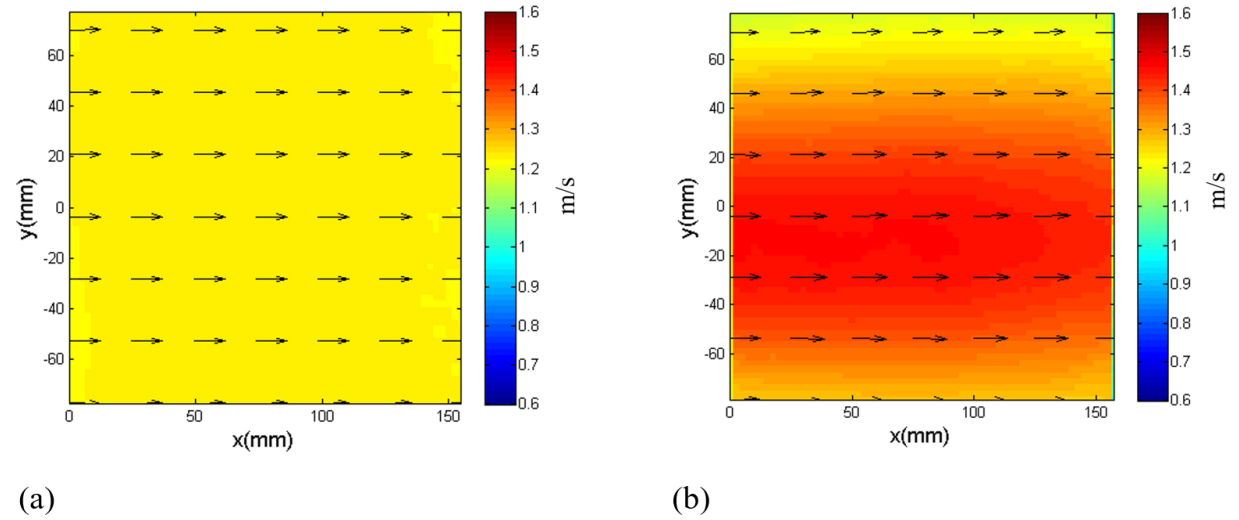

Figure 4-12: Averaged flow velocity upstream of the rotor, (a) without the grid, TI≈ 0.5 %; 35 Hz ≈1.23 m/s, (b) with the grid, TI =7.4%; 35 Hz ≈1.37 m/s

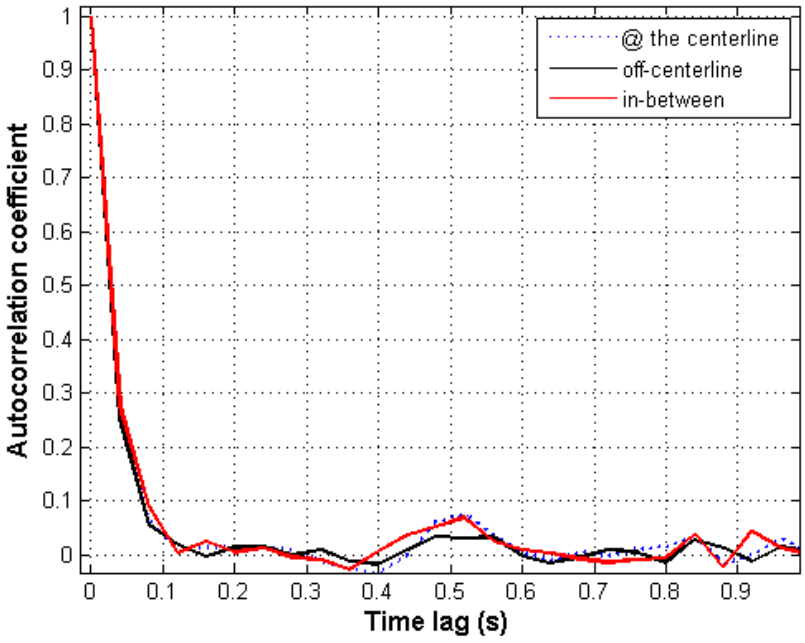

Figure 4-13: Autocorrelation coefficient for different points spanwise the channel 2R upstream of the rotor for TI = 7.4 % case (at the centerline, off-centerline @ 0.7R, in-between @ 0.35R)

4.8 Conclusion

An experimental investigation was performed in order to study the influence of turbulent intensity on a hydrokinetic turbine model efficiency. In this study, a fractal square grid was installed at the entrance of the water tunnel to generate turbulence inflow with turbulent intensity having value of 7.4 %. A model of a hydrokinetic turbine was then installed downstream the grid in the decay region. The experiments were run under three different inflow speeds for both low and high TI cases. It was found that the turbulence intensity has strong influence on the efficiency of the turbine. Use of fractal square grids seems to be an effective way to generate controllable turbulence intensity and thereby obtain hydrokinetic turbine test results in water tunnels more representative of real world conditions.

As future work, fractal grids should be employed in larger-scale water tunnels to verify performance impacts on larger model scale rotors. Additional fractal grids may be used across a range of tunnel sizes to obtain a larger dataset at various TI levels, in order to determine a relationship between TI and C_p. Comparison to CFD rotor model predictions at high TI could inform computational accuracy improvements when analyzing full-scale rotors. It would also be

useful to use a longer water tunnel a PIV wake visualization to look at changes in wake behavior that would impact the spacing of other rotors in an array. Finally, instrumentation (on a larger scale model) of the blade root bending moments would be instructive in ascertaining the impact on fatigue loading of turbulent inflows.

Chapter 5

5 Conclusions

Field and laboratories study were presented throughout this thesis and resulted in a number of achievements. The overall aim of the work was to improve laboratory testing of hydrokinetic turbines by making the testing conditions more similar to those in the real-world flow conditions, i.e. turbulent river and tidal currents. This overarching goal of the research motivated the field study in Manitoba at the CHTTC. The literature review also highlighted that the key property of real-world flows (tidal/rivers flows) differing from lab scale experiments is their ambient turbulent intensity. This property plays a decisive role in the performance of marine current turbines [Mycek, et al., (2014)]. Therefore, the goal of the remainder of the work was to replicate appropriate turbulent intensities in the water tunnel. Overall, these studies provide valuable field and laboratory information for the marine energy and hydrokinetic turbines industry.

Turbulent measurements from the free-surface to the boundary layer region of a real-world fast current channel were presented in chapter 2. These measurements were conducted by deploying an ADV from the river surface to the river bed using a novel technique to guide and control the ADV along the water column. The use of a fin on the ADV for stabilization resulted in raw data that were consistent with reasonable turbulence characteristics. Results showed that the mean velocity of the river was independent of the overall river depth. However, the flow had minimum velocity near the river bed and increased rapidly until mid-depth. From mid depth, the velocity increased gradually until it reached its highest value then decreased gradually again until the free-surface. The maximum energy of the flow occurred 3 m below the free-surface. The minimum energy was carried in the boundary layer region. The turbulent intensity profile through the water column was presented with the highest turbulence intensity at the river bed. The streamwise integral length scale was much larger than those in the upward and spanwise directions. The turbulence was fully developed with a -5/3 slope of the inertial sub-range portion of spectra.

Subsequently, the field study results were used in the fractal grid turbulence study. Different fractal square grids were designed guided by the results found in the existing literature. Two of these grids were manufactured and their turbulence was experimentally investigated using the recirculating

flume tank and PIV. The first manufactured grid failed to give the required results, yielding low turbulence levels. Thus, a second grid was designed and tested. This fractal grid generated turbulence with controlled characteristics and the results showed good agreement with other results in literature for fractal grids. The grid generated turbulence had two regions: a production region and a decay region. The grid increased the turbulent intensity of the flow in the water tunnel from around 0.5% (bare tunnel) to 7.5%. Homogenous and isotropic turbulent flow was generated by the selected grid. The TI peak value seemed to be affected primarily by the size of the biggest bars in the grid and the number of grid iterations. The grid solidity did not appear to have a strong effect on the TI peak location. The opening at the grid's center can cause noticeable shift of the TI peak location. Homogeneity of the grid generated-turbulence in the decay region is also strongly affected by the number of iterations.

The final output of the work was a rotor performance study with the rotor in the turbulent decay region. It was found that the turbulence in the decay region had an fairly large influence on the performance of a model of horizontal axis hydrokinetic turbines across a range of different operational conditions. In contrast, the model showed quite good performance in low TI flow. However, when it was deployed in the fractal generated-turbulence, it performed much less efficiently at the three different inflow speeds. This is a key result of work presented and suggests that experimental testing, if it is to be representative of real-world performance, should not be done in low turbulence tunnels, but rather include turbulence levels representative of real-world conditions.

5.1 Future work

There are clearly many more lines of inquiry open to explore the details of TI impacts on scale rotor testing and help to define acceptable testing procedures to reproduce real-world performance. Of course, without non-proprietary access to real world data gathered from full scale rotors, direct comparison of results is hampered. Provision of some standardized full scale measurements would therefore be invaluable in tuning tunnel scale testing procedures. With the current rig, it would be beneficial to study the effects of TI on the wake expansion behind the rotor and also the wake shape. This could also be extended to turbine arrays in high turbulent flow. This could be done using the one spinning rotor and cheap porous disks to simulate other rotors in the array. A much

longer water channel would be required however, as the fractal grid required much of the channel test section to develop into fully developed turbulent flow. However, conducting testing in a much larger tunnel would help understand the power performance impacts on turbines positioned downstream of other turbines in highly turbulent flow. Studying thrust coefficient and tip vortex behavior in fractal grid turbulence conditions would also provide further insight into experimental work done in a smooth flow, but would again require a longer tunnel to allow the wake sheet to be visualized. The grid generated-turbulence could also be further tuned, by investigation of the grid parameters in a full design of experiments to assess their effects on the flow. For instance, one could change the size of the smallest element in the grid only and study its effects. Also the effect of the grid thickness in the direction of the mean flow on the generated turbulence needs more investigation. Changing the grid' solidity by changing just the bars' lengths while keeping the thickness ratio (t_r) and the number of iteration (N) constant was not investigated yet.

Bibliography

[1] A. J. Wheeler and A. R. Ganji, Introduction to engineering experimentation, 2nd ed., Pearson Education, 2004.

[2] R. J. Adrian, "Particle-imaging techniques for experimental fluid mechanics," *Annual Review of Fluid Mechanics,* vol. 23, pp. 261-304, 1991.

[3] R. J. Adrian, "Twenty years of particle image velocimetry," *Experiments in Fluids,* vol. 39, no. 2, p. 159–169, 2005.

[4] T. J. Andersen, J. Fredsoe and M. Pejrup, "In situ estimation of erosion and deposition thresholds by Acoustic Doppler Velocimeter (ADV)," *Estuarine, Coastal and Shelf Science,* vol. 75, no. 3, p. 327–336, 2007.

[5] F. Ardhuin and A. D. Jenkins, "On the interaction of surface waves and upper ocean turbulence," *Journal of Physical Oceanography,* vol. 36, no. 3, pp. 551-557, 2006.

[6] A. S. Bahaj, A. F. Molland , J. R. Chaplin and W. M. Batten, "Power and thrust measurements of marine current turbines under various hydrodynamic flow conditions in a cavitation tunnel and a towing tank," *Renewable Energy,* vol. 32, no. 3, p. 407–426, 2007.

[7] W. M. Batten, A. S. Bahaj, A. F. Molland and J. R. Chaplin, "Experimentally validated numerical method for the hydrodynamic design of horizontal axis tidal turbines," *Ocean Engineering,* vol. 7, no. 34, p. 1013–1020, 2007.

[8] W. M. Batten, A. S. Bahaj, A. F. Molland and J. R. Chaplin, "Hydrodynamics of marine current turbines," *Renewable Energy,* vol. 31, no. 2, p. 249–256, 2006.

[9] W. M. Batten, A. S. Bahaj, A. F. Molland and J. R. Chaplin, "The prediction of the hydrodynamic performance of marine current turbines," *Renewable Energy,* vol. 33, no. 5, p. 1085–1096, 2008.

[10] A. H. Birjandi, "River ADV measurement and hybrid filter," University of Manitoba, Winnipeg, 2011.

[11] A. H. Birjandi, "Effect of Flow and Fluid Structures on the Performance of Vertical River Hydrokinetic Turbines," PhD thesis, University of Manitoba, Winnepig, 2013.

[12] A. H. Birjandi and E. . L. Bibeau, "Improvement of Acoustic Doppler Velocimetry in bubbly flow measurements as applied to river characterization for kinetic turbines," *International Journal of Multiphase Flow,* vol. 37, no. 8, p. 919–929, 2011.

[13] A. H. Birjandi and E. Bibeau, "Bubble Effects on the Acoustic Doppler Velocimeter (ADV) Measurements," *American Society of Mechanical Engineers,* vol. 2, pp. 27-32, 2009.

[14] A. H. Birjandi, J. Woods and E. L. Bibeau, "Investigation of macro-turbulent flow structures interaction with a vertical hydrokinetic river turbine," *Renewable Energy,* vol. 48, p. 183–192, 2012.

[15] D. J. Booker, D. A. Sear and A. J. Payne, "Modelling three-dimensional flow structures and patterns of boundary shear stress in a natural pool–riffle sequence," *Earth Surface Processes and Landforms,* vol. 26, no. 5, p. 553–576, 2001.

[16] B. Brunk, M. Weber-Shirk, A. Jensen, G. Jirka and L. W. Lion, "Modeling Natural Hydrodynamic Systems with a Differential-Turbulence Column," *Journal of Hydraulic Engineering,* vol. 122, no. 7, pp. 373-380, 1996.

[17] L. Catalina, "Development of a rig and testing procedures for the experimental investigation of horizontal axis kinetic turbines," Master's thesis, University of Victoria, Victoria, 2012.

[18] J. I. Cardesa, T. B. Nickels and J. R. Dawson, "2D PIV measurements in the near field of grid turbulence using stitched fields from multiple cameras," *Experiments in Fluids,* vol. 52, no. 6, p. 1611–1627, 2012.

[19] G. F. Carollo, V. Ferro and D. Termini, "Analyzing Turbulence Intensity in Gravel Bed Channels," *Journal of Hydraulic Engineering,* vol. 131, no. 12, pp. 1050-1061, 2005.

[20] H. Chanson, M. Trevethan and S.-i. Aoki, "Acoustic Doppler velocimetry (ADV) in small estuary: Field experience and signal post-processing," *Flow Measurement and Instrumentation,* vol. 19, no. 5, p. 307–313, 2008.

[21] Y. Li, J. . A. Colby, N. Kelley, R. Thresher, B. Jonkman and S. Hughes, "Inflow Measurement in a Tidal Strait for Deploying Tidal Current Turbines: Lessons, Opportunities and Challenges," in *29th International Conference on Ocean, Offshore and Arctic Engineering*, Shanghai, 2010.

[22] D. Ting , Basics of Engineering Turbulence, University of Windsor, 2016.

[23] K. Dissanayake, "Experimental and numerical modeling of flow and sediment characteristics in open channel junctions," Ph.D. thesis, University of Wollongong, Wollongong, 2009.

[24] R. Duraiswami, S. Prabhukumar and G. L. Chahine, "Air-bubble counting using an inverse acoustic scattering methodAir-bubble counting using an inverse acoustic scattering method," *Acoustical Society of America,* vol. 104, no. 5, p. 2699–2717, 1998.

[25] M. J. Franca and M. Brocchini, "Turbulence in Rivers," Springer International Publishing, Switzerland, 2015.

[26] I. Franchini and C. Crawford, "An experimental study of small scale horizontal axis turbine rotor performance and tip vortex behavior," University of Victoria, Victoria, 2016.

[27] MAVI, C. Current and U. of Victoria, "Impact of channel blockage, free surface," Tech. Rep, Victoria, 2014.

[28] T. S. Frandsen, "Turbulence and turbulence-generated structural loading in wind turbine clusters," Ph.D. dissertation Technical University of Denmark, Denmark, 2007.

[29] D. C. Fugate and C. T. Friedrichs, "Determining concentration and fall velocity of estuarine particle populations using ADV, OBS and LISST," *Continental Shelf Research,* vol. 22, no. 11-13, p. 1867–1886, 2002.

[30] C. M. García, . M. I. Cantero, Y. Niño and M. H. García, "Turbulence Measurements with Acoustic Doppler Velocimeters," *Journal of Hydraulic Engineering,* vol. 131, no. 12, pp. 1062-1073, 2005.

[31] R. J. Garde, Turbulent flow, 3nd ed., New Delhi: New Age International (P), 2013.

[32] L. Ge, S. O. Lee, F. Sotiropoulos and T. Sturm, "3D unsteady RANS modeling of complex hydraulic engineering flows. II: Model validation and flow physics," *Journal of Hydraulic Engineering,* vol. 131, no. 9, pp. 809-820, 2005.

[33] "A physical model for seismic noise generation by turbulent flow in rivers," *JournalofGeophysicalResearch: EarthSurface,* vol. 119, no. 10, p. 2209–2238, 2014.

[34] R. GomesFernandes, B. Ganapathisubramani and J. C. Vassilicos, "Particle image velocimetry study of fractal-generated turbulence," *Journal of Fluid Mechanics,* vol. 711, pp. 306-336, 2012.

[35] I. Grant, "Particle image velocimetry: A review," *Journal of Mechanical Engineering Science* , vol. 1, no. 211, pp. 55--76, 1997.

[36] M. Hand, D. Simms, L. Fingersh, D. Jager, J. Cotrell, S. Schreck and S. Larwood, "Unsteady aerodynamics experiment phase VI: wind tunnel test configurations and available data campaigns unsteady aerodynamics experiment," Technical Report, National Renewable Energy Laboratory, Golden, Colorado, 2001.

[37] M. E. Harrison, W. M. J. Batten, L. E. Myers and A. S. Bahaj, "Comparsion between CFD simulation and experimental for predicting the far wake of horizontal axis tidal turbines," in *8th European Wave and Tidal Energy Conference*, Uppsala, Sweden, 2009.

[38] . M. Harrison, W. Batten , L. Myers and A. Bahaj, "Comparison between CFD simulations and experiments for predicting the far wake of horizontal axis tidal turbines," *IET Renewable Power Generation,* vol. 4, no. 6, pp. 613-627, 2010.

[39] R. H. Jason, "Fractal, Classical, and Active Grid Turbulence: From Production to Decay," Phd Thesis, University of Toronto, Toronto, 2015.

[40] H. Suzuki, K. Nagata, Y. Sakai and R. Ukai, "High-Schmidt-number scaler transfer in regular and fractal grid turbulence," *The Royal Swedish Academy of Sciences, Physica Scripta,* no. T142 014065, 2010.

[41] D. Hurst and J. C. Vassilicos, "Scalings and decay of fractal-generated turbulence," *PHYSICS OF FLUIDS,* vol. 19, no. 3, p. 035103, 2007.

[42] V. G. Iungo, Y.-T. Wu and F. Porté-Agel, "Field Measurements of Wind Turbine Wakes with Lidars," *Journal of Atmospheric and Oceanic Technology,* vol. 30, no. 2, pp. 274-287, 2013.

[43] M. H. A. Kaji, "Turbulent Structure in Open Channel Flow," MASc thesis, University of Windsor, Windsor, 2013.

[44] Kaya, Yoichi and . K. Yokobori, "Environment, energy and economy: Strategies for sustainability," (No. BROOK--0356/XAB). Aspen Inst., Washington, DC (United States), Washington, DC United States, 1998.

[45] N. Kelley and R. Osgood, "Using the time-frequency and wavelet analysis to assess turbulence/rotor interactions," in *In Proc. 19th ASME Wind Energy Symposium*, 2000.

[46] M. Khan, G. Bhuyan, . M. Iqbal and . J. Quaicoe, "Hydrokinetic energy conversion systems and assessment of horizontal and vertical axis turbines for river and tidal applications: A technology status review," *Applied Energy,* vol. 86, no. 10, p. 1823–1835, 2009.

[47] S.-C. Kim, C. T. Friedrichs, J. P.-Y. Maa and . L. D. Wright, "Estimating bottom stress in tidal boundary layer from acoustic doppler velocimeter data," *Journal of Hydraulic Engineering,* vol. 126, no. 6, pp. 399-406, 2000.

[48] A. N. Kolmogorov, "The Local Structure of Turbulence in Incompressible Viscous Fluid for Very Large Reynolds Numbers," *In Dokl. Akad. Nauk SSSR,* vol. 30, no. 4, pp. 301-305, 1941.

[49] N. C. Kraus, A. Lohrmann and R. Cabrera, "New Acoustic Meter for Measuring 3D Laboratory Flows," *Journal of Hydraulic Engineering,* vol. 120, no. 3, pp. 406-412, 1994.

[50] R. W. J. Lacey and A. G. Roy, "Fine-Scale Characterization of the Turbulent Shear Layer of an Instream Pebble Cluster," *Journal of Hydraulic Engineering,* vol. 134, no. 7, pp. 925-936, 2008.

[51] S. Laizet and J. C. Vassilicos, "DNS of Fractal-Generated Turbulence," *Flow, turbulence and combustion,* vol. 87, no. 4, pp. 673-705, 2011.

[52] S. N. Lane, P. M. Biron, K. F. Bradbrook, J. B. Butler, J. H. Chandler, M. D. Crowell, S. J. McLelland, K. S. Richards and A. G. Roy, "Three Dimensional Measurement of River Chanel Flow Processes Using Acoustic Doppler Velocimetry," *Earth Surface Processes and Landforms,* vol. 23, no. 13, pp. 1247-1267, 1998.

[53] LaVision, "LaVision Davis 7.2, version 7.2.2.474," Sep. 1, 2010..

[54] G. J. Leishman, "Challenge in modeling the unsteady aerodynamics of wind turbines," *ASME 2002 Wind Energy Symposium. American Society of Mechanical Engineers,* pp. 141-167, 2002.

[55] A. Lohrmann, ,. Cabrera and N. C. Kraus, "Acoustic-doppler velocimeter(ADV) for laboratory use," *In PROC SYMP FUNDAM ADV HYDRAUL MEAS EXP, ASCE, NEW YORK, NY,(USA),* pp. 351-365, 1994.

[56] B. R. MacKenzie and L. W. C. Leggett, "Wind-based models for estimating the dissipation rates of turbulent energy in aquatic environments: empirical comparisons," *Marine Ecology-Progress Series,* vol. 94, pp. 207-207, 1993.

[57] A. J. MacLeod, S. Barnes, K. G. Rados and . I. G. Bryden, "Wake effects in tidal current turbine farms," in *In International conference on marine renewable energy-conference proceedings*, 2002.

[58] R. Malki, A. Williams, T. Croft, M. Togneri and I. Masters, "A coupled blade element momentum – computational fluid dynamics model for evaluating tidal stream turbine performance," *Applied Mathematical Modelling*, vol. 37, no. 5, p. 3006–3020, 2013.

[59] R. H. Marcuso, Turbulence theory, types and simulation, Nova Science Pub Inc, 2012.

[60] N. Mazellier and J. C. Vassilicos, "Turbulence without Richardson–Kolmogorov cascade," *Physics of Fluids*, vol. 22, no. 7, p. 075101, 2010.

[61] S. J. McLelland and A. P. Nicholas, "A new method for evaluating errors in high-frequency ADV measurements," *Hydrological Processes*, vol. 14, no. 2, pp. 351-66, 2000.

[62] S. McTavish, D. Feszty and F. Nitzsche, "An experimental and computational assessment of blockage effects on wind turbine wake development," *Wind Energy*, vol. 17, no. 10, pp. 1515-1529, 2014.

[63] I. A. Milne, R. N. Sharma, R. G. J. Flay and S. Bickerton, "Characteristics of the turbulence in the flow at a tidal stream power site," *Philosophical Transactions of the Royal Society of London A: Mathematical, Physical and Engineering Sciences*, vol. 371, no. 1985, p. 20120196, 2013.

[64] N. Mori, . T. Suzuki and S. Kakuno, "Noise of Acoustic Doppler Velocimeter Data in Bubbly Flows," *Journal of engineering mechanics*, vol. 133, no. 1, pp. 122-125, 2007.

[65] S. S. Mukherji, "Design and critical performance evaluation of horizontal axis hydrokinetic turbine," MASc thesis, Missouri University of Science and Technology, 2010.

[66] P. Mycek, B. Gaurier, G. Germain, G. Pinon and E. Rivoalen, "Experimental study of the turbulence intensity effects on marine current turbines behaviour," *Renewable Energy*, vol. 66, no. 2014, p. 729–746, 2014.

[67] P. Mycek, B. Gaurier, G. Germain, G. Pinon and E. Rivoalen, "Experimental study of the turbulence intensity effects on marine current turbines behaviour. Part II: Two interacting turbines," *Renewable Energy,* vol. 68, no. 2014, p. 876–892, 2014.

[68] L. Myers and A. Bahaj, "Experimental analysis of the flow field around horizontal axis tidal turbines by use of scale mesh disk rotor simulators," *Ocean Engineering,* vol. 37, no. 2-3, p. 218–227, 2009.

[69] H. Nakagawa, N. Iehisa and U. Hiroshi, "Turbulence of open channel flow over smooth and rough beds," *Proc Jpn Soc Civ Eng,* vol. 241, no. 1975, pp. 155-168, 1975.

[70] I. Nezu and W. Rodi, "Open-channel flow measurements with a laser Doppler anemometer," *Journal of Hydraulic Engineering,* vol. 112, no. 5, pp. 335-355, 1986.

[71] I. Nezu, N. Hiroji and Gerhard H. Jirka, "Turbulence in open-channel flows," *Journal of Hydraulic Engineering,* vol. 120, no. 10, pp. 1235-1237, 1994.

[72] A. P. Nicholas and S. S. G. H, "Numerical simulation of three-dimensional flow hydraulics in a braided channel," *Hydrological Processes,* vol. 13, no. 6, pp. 913-929, 1999.

[73] V. I. Nikora and G. G. Derek, "ADV measurements of turbulence: Can we improve their interpretation?," *Journal of Hydraulic Engineering,* vol. 124, no. 6, pp. 630-634, 1998.

[74] V. Nikora, "3 Hydrodynamics of gravel-bed rivers: scale issues," *Developments in Earth Surface Processes,* vol. 11, pp. 61-81, 2007.

[75] Nortek, A., "Vector current meter, User Manual," Nortek AS,, Norway, 2005.

[76] N. R. Olsen and S. Siri, "Three-dimensional numerical modelling of water flow in a river with large bed roughness," *Journal of Hydraulic Research,* vol. 33, no. 4, pp. 571-581, 1995.

[77] E. Osalusi, S. Jonathan and H. Robert, "Structure of turbulent flow in EMEC's tidal energy test site," *International Communications in Heat and Mass Transfer,* vol. 36, no. 5, pp. 422-431, 2009.

[78] O'Malley, Peter, "Trajectories of Inertial Particles and Fluid Elements," Haverford College, Haverford, 2008.

[79] United Nations, "Population division of the department of economic and social affairs of the United Nations Secretariat, World population prospects,," Report, United Nations, United Nations, New York, 2015.

[80] E. Precht, J. Felix and H. Markus, "Near-bottom performance of the Acoustic Doppler Velocimeter (ADV)- a comparative study," *Aquatic Ecology*, vol. 40, no. 4, pp. 481-492, 2006.

[81] D. Queiros-Conde and J. C. Vassilicos, "Turbulent wakes of 3D fractal grids," *Intermittency in turbulent flows*, pp. 136-167, 2001.

[82] M. Raffel, C. E. Willert, S. Wereley and J. Kompenhans, Particle image velocimetry: a practical guide, Springer, 2013.

[83] Richardson Lewis Fry, Weather prediction by numerical process, Cambridge University Press, 2007.

[84] M. A. Sarker, "Flow measurement around scoured bridge piers using Acoustic-Doppler Velocimeter (ADV)," *Flow measurement and instrumentation*, vol. 9, no. 4, pp. 217-227, 1998.

[85] M. S. Selig and B. D. McGranahan , "Wind tunnel aerodynamic tests of six airfoils for use on small wind turbines," *Journal of solar energy engineering*, vol. 126, no. 4, pp. 986-1001, 2004.

[86] Seoud, R. E and J. C. Vassilicos, "Dissipation and decay of fractal generated turbulence," *Physics of Fluids* , vol. 19, no. 10, p. 105108, 2007.

[87] R. K. Singh and M. R. Ahmed, "Blade design and performance testing of a small wind turbine rotor for low wind speed applications," *Renewable Energy*, vol. 50, pp. 812-819, 2013.

[88] S. K. Sinha, F. Sotiropoulos and A. J. Odgaard, "Three-dimensional numerical model for flow through natural rivers," *Journal of Hydraulic Engineering*, vol. 124, no. 1, pp. 13-24, 1998.

[89] A. Staicu, B. Mazzi, J. C. Vassilicos and W. van de Water, "Turbulent wakes of fractal objects," *Physical Review*, vol. 67, no. 6, p. 066306, 2003.

[90] Stefan, W, "Experimental study of turbulence generated by fractal grids," University of Oldenburg, 2011.

[91] S. Weitemeyer, N. Reinke, J. Peinke and M. Hölling, "Multi-scale generation of turbulence with fractal grids and an active grid," *Fluid Dynamics Research*, vol. 45, no. 6, p. 061407, 2013.

[92] M. C. Stone and R. H. Hotchkiss, "Turbulence descriptions in two cobble-bed river reaches," *Journal of Hydraulic Engineering*, vol. 133, no. 2, pp. 1367-1378, 2007.

[93] R. Stresing, J. Peinke, R. E. Seoud and J. C. Vassilicos, "Defining a new class of turbulent flows," *Physical review letters*, vol. 104, no. 19, p. 194501, 2010.

[94] K. B. Strom and A. N. Papanicolaou, "ADV measurements around a cluster microform in a shallow mountain stream," *Journal of Hydraulic Engineering*, vol. 133, no. 12, pp. 1379-1389, 2007.

[95] A. N. Sukhodolov and B. L. Rhoads, "Field investigation of three-dimensional flow structure at stream confluences: 2. Turbulence," *Water Resources Research*, vol. 37, no. 9, pp. 2411-2424, 2001.

[96] A. Sukhodolov, M. Thiele and H. Bungartz, "Turbulence structure in a river reach with sand bed," *Water Resources Research*, vol. 34, no. 5, pp. 1317-1334, 1998.

[97] Sulaiman, M. S, S. K. Sinnakaudan and M. R. Shukor, "Near bed turbulence measurement with acoustic doppler velocimeter (ADV)," *KSCE Journal of Civil Engineering*, vol. 17, no. 6, pp. 1515-1528, 2013.

[98] H. J. Sutherland and N. D. Kelley, "Fatigue damage estimate comparisons for northern European and US wind farm loading environments," in *Proceedings of WindPower*, 1995.

[99] M. Talavera and F. Shu, "Experimental Study of Turbulence Influence on Wind Turbine Performance," North American Wind Energy Academy 2015 Symposium, Virginia Tech, 2015.

[100] G. I. Taylor, "Statistical theory of turbulence," *Proceedings of the Royal Society of London A: Mathematical, Physical and Engineering Sciences,* vol. 151, no. 873, pp. 421-444, 1935.

[101] J. Thomson, B. Polagye, V. Durgesh and M. C. Richmond, "Measurements of turbulence at two tidal energy sites in Puget Sound, WA," *IEEE Journal of Oceanic Engineering,* vol. 37, no. 3, pp. 363-374, 2012.

[102] M. Trevethan, H. Chanson and M. Takeuchi, "Continuous high-frequency turbulence and suspended sediment concentration measurements in an upper estuary," *Estuarine, Coastal and Shelf Science,* vol. 73, no. 1, pp. 341-350, 2007.

[103] H. M. Tritico and R. H. Hotchkiss, "Unobstructed and obstructed turbulent flow in gravel bed rivers," *Journal of Hydraulic Engineering,* vol. 131, no. 8, pp. 635-645, 2005.

[104] J. Trowbridge and S. Elgar, "Turbulence Measurements in the Surf Zone*," *Journal of Physical Oceanography,* vol. 31, no. 8, pp. 2403-2417, 2001.

[105] P. C. Valente and J. C. Vassilicos, "The decay of turbulence generated by a class of multiscale grids," *Journal of Fluid Mechanics,* vol. 687, pp. 300-340, 2011.

[106] J. H. VanZwieten, M. N. Egeland, K. D. von Ellenrieder, J. W. Lovenbury and L. Kilcher, "Experimental evaluation of motion compensated ADV measurements for in-stream hydrokinetic applications," *In Current, Waves and Turbulence Measurement (CWTM), 2015 IEEE/OES Eleventh,* pp. 1-8, 2015.

[107] G. Voulgaris and J. H. Trowbridge, "Evaluation of the acoustic Doppler velocimeter (ADV) for turbulence measurements*," *Journal of Atmospheric and Oceanic Technology* , vol. 15, no. 1, pp. 272-289, 1998.

[108] Warner, Scott O, "Autocorrelation-based estimate of particle image density in particle image velocimetry," 2012.

[109] J. I. Whelan, J. M. R. Graham and J. Peiro, "A free-surface and blockage correction for tidal turbines," *Journal of Fluid Mechanics*, vol. 624, pp. 281-291, 2009.

[110] A. C. Wilcox and E. E. Wohl, "Field measurements of three-dimensional hydraulics in a step-pool channel," *Geomorphology*, vol. 83, no. 3, pp. 215-231, 2007.

[111] Y. Shoitiro, "The structure of river turbulence," *Bulletin of the Disaster Prevention Research Institute,* vol. 17 , no. 2, pp. 1-29, 1967.

[112] T. Clark, K. Black, J. Ibrahim, J. Hernon and N. Minns, Turbulence: Best practices for data processing, classification and characterisation of turbulent flows, Turbulence in Marine Environments, 2015.

[113] S. Discetti, I. Ziskin, R. Adrian and K. Prestridge, "PIV study of fractal grid turbulence," *In 9th International Symposium on Particle Image Velocimetry–PIV*, vol. 11, 2011.

[114] "The Kaya Identity," PennState Department of Meteorology. Meteo 469, From Meteorology to Mitigation: Understanding Global Warming, November 2016. [Online]. Available: https://www.e-education.psu.edu/meteo469/node/213. [Accessed 11 November 2016].

[115] "Canadian Electricity Association," Power for the future, November 2016. [Online]. Available: http://powerforthefuture.ca/future-project/robert-h-saunders-generating-station/. [Accessed 10 November 2016].

[116] "Marine Renewables Canada," [Online]. Available: http://www.marinerenewables.ca/. [Accessed 8 October 2016].

[117] N. R. Canada, "Marine Energy, what is marine renewable energy," [Online]. Available: http://canmetenergy.nrcan.gc.ca/renewables/marine-energy/2475. [Accessed January 2016].

[118] N. S. Power, "Tidal Power," [Online]. Available: http://www.nspower.ca/en/home/about-us/how-we-make-electricity/renewable-electricity/annapolis-tidal-station.aspx. [Accessed November 2016].

[119] U. Nations, "Population division of the department of economic and social affairs of the United Nations Secretariat, World population prospects, 2015 Revision," [Online]. Available: https://esa.un.org/unpd/wpp/publications/files/key_findings_wpp_2015.pdf. [Accessed November 2016].

[120] D. Dabiri, "Cross-Correlation Digital Particle Image Velocimetry – A Review," in *Turbulencia*, Curitiba, ABCM, 2006, pp. 155-199.

[121] . M. R. Soltani, A. H. Birjandi and M. Seddighi, "Effect of surface contamination on the performance of a section of a wind turbine blade," *Journal of Scientia Iranica*, vol. 3, no. 18, pp. 349-357, 2011.

[122] K. Ghorbanian, M. R. Soltani and M. M. Dehghan, "Experimental investigation on turbulence intensity reduction in subsonic wind tunnels," *Aerospace Science and Technology*, vol. 15, no. 2, pp. 137-147, 2011.

[123] K. B. Strom and A. N. Papanicolaou, "ADV measurements around a cluster microform in a shallow mountain stream," *Journal of Hydraulic Engineering*, vol. 133, no. 12, pp. 1379-1389, 2007.

[124] . B. E. Balcer, "Boundary layer flow control using plasma induced velocity," Master's Thesis, Air Force Institute of Technology, Department of Aeronautics and Astronautics, 2005.

[125] . R. George, . R. E. Flick and . R. T. Guza, "Observations of turbulence in the surf zone," *Journal of Geophysical Research*, vol. 99, pp. 801-810, 1994.

[126] V. I. Nikora and G. M. Smart, "Turbulence characteristics of New Zealand gravel-bed rivers," *Journal of Hydraulic Engineering,* vol. 123, no. 9, pp. 764-773, 1997.

[127] A. J. Williams 3rd, J. S. Tochko, R. L. Koehler, W. D. Grant, T. F. Gross and C. V. Dunn, "Measurement of turbulence in the oceanic bottom boundary layer with an acoustic current meter array," *Journal of Atmospheric and Oceanic Technology,* vol. 4, no. 2, pp. 312-327, 1987.

Appendix A

6 Additional Information

6.1 Particle Image Velocimetry (PIV)

Particle Image Velocimetry (PIV) technique was used to study the fractal grid-generated turbulence properties. It was used also to document the flow in the experiments of studying the performance of the rotor. Particle Image Velocimetry (PIV) is an optical method for measuring the speed of liquids and gases. PIV is used to visualize the flow then a high-speed CCD camera takes image of the visualized flow to calculate the velocity field. It was used to calculate the velocity field for many different applications such as in thermal convection, boundary layer studies, vortex shading of a body inside a flow in wind and water tunnels experiments [Raffel, et al., (2002)]. PIV is used in the present work to measure the flow speed in the water tunnel in a two-dimensional of the flow field. As part of PIV, the flow is seeded with small particles. The flow velocity is calculated by capturing the location of the seeding particles in the flow by recording images which are separated by time interval. The velocity of all particles is assumed as a constant velocity. Then the displacement of each particle in the two directions is calculated. By knowing the time interval between the images and the movement of the particles between images, the speed and direction of the fluid flow can be calculated. The displacement of each particle is calculated by dividing each image to several interrogation windows [Adrian, (1991)]. The ability of PIV to accurately measure the flow velocity is a function of many parameters including the particle image density, or number of particles contained within an image [Warner, (2012)]. In the PIV technique, the field velocity is calculated using four general methods: autocorrelation, cross correlation, optical correlation, and Young's Fringes [Adrian, (2005)]. In the autocorrelation method, an autocorrelation involves correlating a single image with itself. The image is convert into a digital form and send to a computer for processing and once the correlation peak is determined using autocorrelation, the instantaneous velocity of the flow is calculated. High resolution measurements are enabled in this method because the particle images are taken on a film [Adrian, (2005)]. The autocorrelation method presents two problems: ambiguity in the flow direction and limiting the

measurable velocity range in very small displacements. These two issues are posed because of the fact that the auto-correlation function of a doubly-exposed image has a dominant central peak, and two symmetric side peaks [Dabiri, (2006)]. To overcome these two problems, the preferred method is to singly expose images, and perform cross-correlation method. The auto-correlation method required that the images be doubly exposed, while the cross-correlation required that the images be singly exposed. The displacement information is then obtained once the correlation peak is determined using either of these methods. The cross-correlation method involves correlating two separate images together. Spatial cross-correlation between these two images is used to determine the flow speed. Figure 6.1 shows the cross-correlation data processing [Dabiri, (2006)]. As shown in the Figure 6.1a, the first step is an interrogation window subsamples the main sequential image pairs f (i, j) and g (i, j) at the same location within the image. Then FFT cross-correlation algorithm or direct cross-correlation is performed on these two interrogation regions. This step is resulted in a cross-correlation pixel domain. Within this domain the peak's location corresponding to the average shift of particles (dx, dy) within the interrogation windows is identified. Finally, this shift (dx, dy) is converted into a velocity vector Figure 6.1d [Dabiri, (2006)].

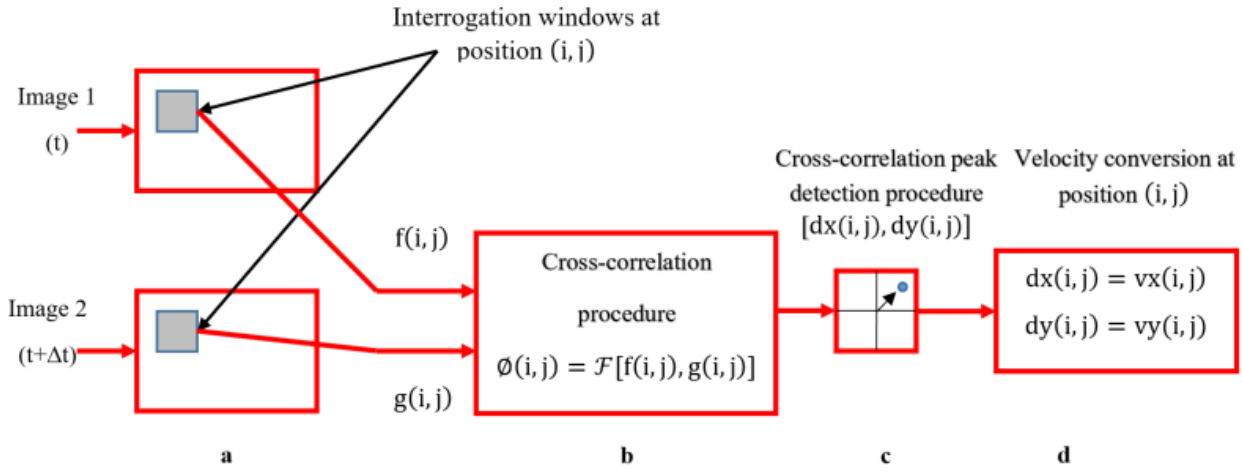

Figure 6-1: The cross-correlation data processing

In the optical correlation method, the two digital FFT operations are replaced with optical Fourier transformations [Adrian, (2005)]. Young's fringe method started with capturing a single flow picture with double- or multi-exposed particles. The image pairs act as interfering point sources, with the transmitted light forming Young's fringes. The transparency and the plane on which the fringes were being observed were arranged to be in the principle focal planes of a converging lens,

so that the fringe pattern was an accurate Fourier transform of the phase and amplitude of the transmitted light from the interrogation window. A lens is used in this method to perform a two-dimensional Fourier transform of the transmitted light from the interrogation window. Then the amplitude and orientation of the fringe spacing was used to infer the image displacement [Grant, (1997)].